ELECTROCHEMICAL METHODS AND MEMBRANE BIOREACTOR APPROACH FOR WASTEWATER TREATMENT AND WATER QUALITY ASSESSMENT

By

XIAO QU

A thesis submitted in conformity with the requirements

for the Degree of Mater of Science in Engineering

Faculty of Engineering

Lakehead University

ABSTRACT

Severe water scarcity, high health standards, and strict disposal limits have necessitated the development of novel and robust strategies for wastewater remediation and water quality analysis at lower cost with reduced energy expenditure. Electrochemistry offers promising and environmentally compatible approaches for the treatment of wastewater and for water quality assessment. Meanwhile, membrane bioreactor (MBR) technology is widely recognized as an effective method for enhanced wastewater treatment or re-use. In this study, an enhanced electrochemical oxidation process was first developed for the decontamination of phenolic compounds. Subsequently, a thermophilic submerged aerobic membrane bioreactor (TSAMBR) integrated with electrochemical oxidation (EO) was constructed for the treatment of thermomechanical pulping pressate. Finally, a photoelectrochemical method was proposed for the rapid determination of chemical oxygen demand (COD).

A novel process based on an adsorption and release step followed by electrochemical oxidation was developed for the decontamination of three phenolic compounds: Phenol, p-nitrophenol (p-NPh) and p-cresol. The adsorption step was carried out by adsorbing the three pollutants onto a hyper-cross-linked resin (MN-200). The adsorption equilibrium and kinetics, as well as temperature effects were systematically studied. The MN-200 resin exhibited a high removal efficiency of the three pollutants and the adsorbed phenolic compounds can be efficiently released in a NaOH solution. The pre-concentrated phenolic compounds were further treated via electrochemical oxidation at a $Ti/SnO_2–Sb_2O_5–IrO_2$ electrode. The first-order model fitted the kinetics data of the electrochemical oxidation very well, showing that the degradation rate constant decreased in the order of p-NPh > phenol > p-cresol. The integration of the effective

I

pre-concentration process with the electrochemical oxidation offers a promising approach for the effective decontamination of phenolic pollutants in wastewater.

A TSAMBR system was operated at $51 \pm 1°C$ to investigate its feasibility for the treatment of thermomechanical pulping pressate and to elucidate the effect of the hydraulic retention time (HRT) on membrane fouling. The results showed that the removal efficiency of COD decreased slightly as the HRT decreased. However, the short HRT induced high concentrations of mixed liquor suspended solids (MLSS) and bound extracellular polymeric substances (EPS), as well as small particles in the bulk sludge. The structure of the cake layer formed at an HRT of $1.1 \pm 0.1d$ was different from that developed at an HRT of $0.9 \pm 0.1d$. The cake layer structure bears more responsibility for membrane fouling in the TSAMBR. An optimal HRT of $1.1 \pm 0.1d$ for the TSAMBR was determined. An electrochemical oxidation (EO) process was employed as a post treatment. The electrochemical oxidation of the TSAMBR effluent was performed on the $Ti/SnO_2-Sb_2O_5-IrO_2$ electrode. Complete decolourization and an overall 94% – 97% removal in COD were obtained after 5.5 hours of oxidation. This demonstrates the integrated TSAMBR – EO process is a promising technology for system closure.

A novel photoelectro-bifunctional electrode ($TiO_2/Ti/TiO_2-Pt$) for the rapid determination of COD was successfully fabricated. The TiO_2 nanotubes, serving both as the photocatalyst and the support for the electrocatalyst, were directly grown on both sides of a Ti plate via anodic oxidation. Pt nanoparticles were loaded on one side of TiO_2 nanotubes by the photo-reduction method. For the determination of COD, the bifunctional electrode exhibits a low detection limit, a high sensitivity and a high Cl^- tolerance. For actual wastewater samples, the COD results obtained by the electrode were in excellent agreement with those determined by the standard $K_2Cr_2O_7$ method.

ACKNOWLEDGEMENTS

LIST OF ABBREVIATIONS AND SYMBOLS

AOPs	Advanced Oxidation Processes
BOD	Biochemical Oxygen Demand
CA	Chronoamperometry
Ce	Equilibrium Concentration
COD	Chemical Oxygen Demand
COM	Conventional Optical Microscope
CV	Cyclic Voltammetry
DO	Dissolved Oxygen
Ea	Activation Energy
EC	Electrocatalysis
EDS	Energy Dispersive X-ray Spectrometry
EO	Electrochemical Oxidation
EPS	Extracellular Polymeric Substances
F/M	Food to Microorganisms Ratio
HRT	Hydraulic Retention Time
i	Current Density
K_F	Adsorption Capacity in Freundlich Isotherm
K_L	Langmuir Isotherm Constant
LSV	Linear Sweep Voltammetry
MBRs	Membrane Bioreactors
MLSS	Mixed Liquor Suspended Solids
OLR	Organic Loading Rate
PEBC	Photoelectro-bifunctional Catalysis
PEC	Photoelectrocatalysis
PN/CH	Protein to Carbohydrate Ratio

PSD	Particle Size Distribution
PtNPs	Pt Nanoparticles
q_e	Equilibrium Adsorption Capacity
q_m	Maximum Adsorption Capacity
Q_H	Hydrogen Oxidation Charge
R	Hydraulic Resistance
SEM	Scanning Electron Microscope
SRT	Sludge Retention Time
TAMBRs	Thermophilic Aerobic Membrane Bioreactors
TiO_2NTs	TiO_2 Nanotubes
TMP	Transmembrane Pressure
TSAMBRs	Thermophilic Submerged Aerobic Membrane Bioreactors
TSS	Total Suspended Solids
XRD	X-ray Diffraction

TABLE OF CONTENTS

Chapter 1. Introduction

1.1   Waste Pollution and the Conventional Remediation Technologies

One of the most pervasive problems afflicting people worldwide is inadequate access to clean water caused by severe water pollution. It is estimated that the amount of wastewater produced annually is 1.5×10^{12} m^3 which is six times more water than that exists in all the rivers of the world; two million tons of sewage, industrial and agricultural waste are discharged into the world's water every single day; 70% of industrial waste in developing countries are discharged into water bodies without any treatment; and 3900 children die per day because of the diseases transmitted through unsafe drinking water [1-3]. There is no doubt that the proper treatment and remediation of a huge amount of wastewater is both necessary and urgent.

The conventional wastewater treatment techniques can be divided into two major groups [4-7]: (i) separation technologies based on physicochemical methods (e.g. adsorption, coagulation and flocculation, sedimentation, flotation, filtration, extraction, air stripping and membrane processes, etc.) and (ii) transformation technologies dominated by both microbiological and chemical methods (e.g., incineration and permeable reactive barriers, etc.).

However, all these methods suffer from some major drawbacks when treating industrial wastewater. For instance, adsorption and filtration are not always sufficient to achieve the discharge limits; coagulation and flotation generate a large amount of sludge; the presence of toxic or biorefractory pollutants may hinder the conventional biological approach; chemical oxidations have low capacity rates and need transportation and storage of dangerous reactants; and advanced oxidation processes require high investment costs [8]. Under these circumstances,

more effective, lower-cost and robust methods for the decontamination and re-use of wastewater are needed, without further stressing the environment or endangering human health by the treatment itself.

1.2 New Methods for Industrial Wastewater Treatment and Water Quality Analysis

In recent years, electrochemical technologies have reached a promising state of development due to intensive investigations that improved the electrocatalytic activity and stability of electrode materials [9-11], and can be effectively used for purification of industrial wastewater polluted with organic compounds. Particularly, the use of electrochemical oxidation for the treatment of toxic or biorefractory organics has received great attention as electrons provide a powerful, versatile, efficient, cost effective, and clean reagent [8-13]. Another technology now actively being pursued is membrane bioreactors (MBRs) [14-17]. This technology combines suspended biomass, similar to the conventional activated sludge process, with immersed microfiltration or ultrafiltration membranes that replace gravity sedimentation and clarify the wastewater effluent. MBRs can produce high-quality effluent that is suitable for unrestricted irrigation and other industrial applications. However, individual application of MBRs processes is limited due to the presence of biorecalcitrant compounds (resistant to biodegradation) in the industrial wastes. On the other hand, the application of single electrochemical oxidation is very efficient, but significantly more expensive than the biological process alone. An advantage of the combined wastewater treatment is the synergistic effect as biological and electrochemical methods complement each other. The electrochemical oxidation, acting as a post treatment process after MBRs, can be responsible for the decolourization and further reduction of chemical oxygen

demand (COD) in MBRs effluent. The coupling reduces the total residence time in both and biological and electrochemical reactors while obtaining the desired total efficiency. Thus the process becomes cost-effective and achieves a very high-quality effluent that can reach the goal of system closure in industries.

In addition to the electrochemical oxidation for remediation of wastewater, electroanalytical techniques for monitoring and detection of pollutants in the environment are also undergoing a rapid development [18]. A number of electrochemical sensors have been developed and applied for the rapid and accurate determination of heavy metals, pesticides, phenolic compounds and the chemical oxygen demand (COD) of wastewater [19-22].

1.3   Rationale and Scope of This Thesis

The introduction of more stringent environmental regulations, coupled with financial and social pressures for sustainable development, has pressed toward "zero-effluent" process. The conventional wastewater treatment technologies can no longer meet the requirements and, thus, developing new or more efficient remediation and detection technologies are of great urgency and importance. In this context, the main objectives of this study are:

1) Explore an improved electrochemical oxidation technology based on an effective pre-concentration process for the decontamination of phenolic compounds in a synthetic industrial wastewater.

2) Test the feasibility of using a thermophilic submerged aerobic membrane bioreactor (TSAMBR) followed by electrochemical oxidation for the remediation and re-use of thermomechanical pulping pressate and understand the membrane fouling behaviours and mechanisms in the TSAMBR.

3) Propose a photoelectrochemical method for rapid determination of chemical oxygen demand (COD) based on a novel bifunctional electrode.

This thesis is composed of seven chapters. In the next chapter, a comprehensive literature review will be provided. In Chapter 3, the experimental materials and methods used throughout the project will be discussed. Chapter 4 to Chapter 6 will present the complete study of electrochemical oxidation, the TSAMBR system and rapid COD determination, respectively. The final chapter, Chapter 7, will provide a summary of the results and conclusions.

References

[1] UN-WWAP "The World Water Development Report 1: Water for People, Water for Life," UNESCO, 2003.

[2] M. A. Montgomery, M. Elimelech, *Environ. Sci. Technol.* **2007**, *41*, 17.

[3] M. A. Shannon, P. W. Bohn, M. Elimelech, J. G. Georgiadis, B. J. Marinas, A. M. Mayes, *Nature* **2008**, *452*, 301.

[4] G. Tchobanoglous, F. L. Burton, H. D. Stensel *Wastewater engineering :treatment and reuse /Metcalf & Eddy, Inc*; 4th ed. ed.; McGraw-Hill: Boston, 2003.

[5] R. D. Letterman *Water quality and treatment : a handbook of community water supplies* 5th ed. ed.; McGraw-Hill: New York, 1999.

[6] M. Henze, P. Harrenmoes, J. la Cour Jansen, E. Arvin *Wastewater Treatment: Biological and Chemical Processes*; 3rd ed. ed.; Springer-Verlag: Berlin, Germany, 2002.

[7] E. Brillas, I. Sirés, M. A. Oturan, *Chem. Rev.* **2009**, *109*, 6570.

[8] M. Panizza, G. Cerisola, *Chem. Rev.* **2009**, *109*, 6541.

[9] C. A. Martinez-Huitle, S. Ferro, *Chem. Soc. Rev.* **2006**, *35*, 1324.

[10]   G. H. Chen, *Sep. Purif. Technol.* **2004**, *38*, 11.

[11]   C. Comninellis, G. Chen *Electrochemistry for the environment*; Springer: New York, 2010.

[12]   M. Panizza, G. Cerisola, *Environ. Sci. Technol.* **2004**, *38*, 5470.

[13]   G. Zhao, X. Cui, M. Liu, P. Li, Y. Zhang, T. Cao, H. Li, Y. Lei, L. Liu, D. Li, *Environ. Sci. Technol.* **2009**, *43*, 1480.

[14]   W. B. Yang, N. Cicek, J. Ilg, *J. Membr. Sci.* **2006**, *270*, 201.

[15]   B.-Q. Liao, J. T. Kraemer, D. M. Bagley, *Crit. Rev. Env. Sci. Technol.* **2006**, *36*, 489.

[16]   S. Judd, *Trends Biotechnol.* **2008**, *26*, 109.

[17]   A. Santos, W. Ma, S. J. Judd, *Desalination* **2011**, *273*, 148.

[18]   M. Badihi-Mossberg, V. Buchner, J. Rishpon, *Electroanalysis* **2007**, *19*, 2015.

[19]   G. M. S. Alves, J. M. C. S. Magalhães, H. M. V. M. Soares, *Electroanalysis* **2011**, 23, 1410.

[20]   M. Trojanowicz, *Electroanalysis* **2002**, *14*, 1311.

[21]   Y. Liu, J. Lei, H. Ju, *Electroanalysis* **2010**, *22*, 2407.

[22]   S. Y. Ai, M. N. Gao, Y. Yang, J. Q. Li, L. T. Jin, *Electroanalysis* **2004**, *16*, 404.

Chapter 2. Literature Review

This study focuses on the development of electrochemical methods and membrane bioreactor approach for industrial wastewater treatment and water quality assessment. A thorough analysis of the literature emphasizing the electrochemical oxidation process, membrane bioreactor technology and electrochemical methods for COD determination is presented in this chapter.

2.1 Electrochemical Oxidation of Biorefractory Pollutants in Wastewater

2.1.1   Biorefractory pollutants and their treatment

Wastewater with organic biorefractory pollutants leads to the partial inhibition of biodegradation, as microorganisms are sensitive to these pollutants. Biorefractory compounds found in industrial wastewater include halogenated organics, aromatic and aliphatic hydrocarbons and pesticides [1]. Biorefractory pollutants cannot be completely removed by biological treatments, so water contaminated with these compounds must be treated by chemical methods such as the environmentally friendly advanced oxidation processes (AOPs) [2-3]. AOPs are chemical, photochemical, or electrochemical methods sharing the common feature of the *in-situ* production of hydroxyl radical ($\cdot$OH) as their main oxidizing agent. The most popular AOPs include Fenton processes, photo-assisted Fenton processes, UV/Fe^{3+}-oxalate/H_2O_2, electrocatalysis, photocatalysis, ozone water system, H_2O_2 photolysis, O_3/UV, and others [4]. Among the AOPs, electrochemical oxidation, featuring strong oxidation performance, low-volume application, amenability to automation and environmental compatibility is considered as a promising and effective method for the degradation of biorefractory organic pollutants in wastewater [5-6].

2.1.2 Electrochemical oxidation technology

Fig. 2.1 shows a conceptual diagram of an electrochemical reactor for wastewater electrochemical oxidation [7], which includes a power supply, a cathode, an anode and the electrolyte. Under the application of potential or current, the organic compounds in wastewater can be oxidized on the surface of the anode or in the electrolyte through an electrochemically generated mediator.
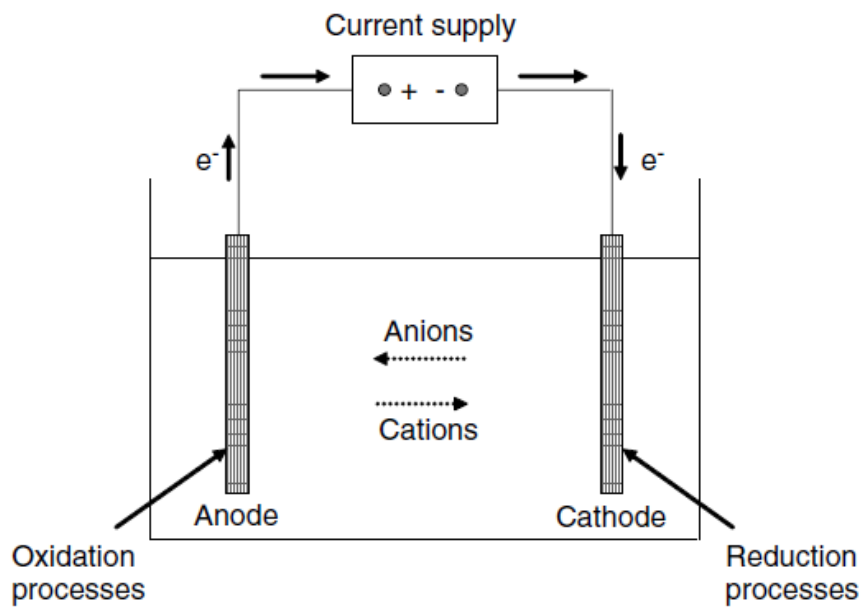
Fig. 2.1 Conceptual diagram of an electrochemical reactor [7].

Electrochemical processes offer in specific cases some advantages such as the environmental compatibility (e.g. no need for auxiliary chemicals), versatility (e.g. applicability to a wide range of pollutants), energy efficiency (e.g. no need for high pressures and temperatures), amenability to automation and cost effectiveness [6]. For these reasons electrochemical oxidation is considered a promising and attractive technique for the effective advanced treatment of wastewaters containing non-biodegradable organic compounds, such as textile effluents [8-10] landfill leachates [11-13] and tannery waste liquors [14].

2.1.3 Mechanisms of electrochemical oxidation

Electrochemical oxidation treatment for wastewater can be subdivided into two important categories: direct oxidation at the anode, and indirect oxidation using appropriate anodically - formed oxidants. The anodic direct oxidation does not involve the addition of oxidation catalysts to the wastewater and has no tendency to produce secondary pollution. This project mainly focuses on direct electrochemical oxidation, particularly, oxidation via intermediates of oxygen evolution for the destruction of biorefractory pollutants.

A mechanism for the electrochemical oxidation of organics based on the intermediates of oxygen evolution reaction in aqueous media was first proposed by Johnson *et al.* [15-19] and furthered by Comninellis *et al.* [20-23] who found that the selectivity and efficiency of the electrochemical oxidation was strongly influenced by the electrode materials. In particular, several anodes favoured partial and selective oxidation of pollutants, defined as "active" anodes, while others favoured complete mineralization of pollutants to CO_2, defined as "non-active" anodes. In order to interpret these observations, they proposed a comprehensive model for oxidation of organics at metal oxide electrodes with simultaneous oxygen evolution (Fig. 2.2).

The first step in the oxygen transfer reaction is the discharge of water to form adsorbed hydroxyl radicals:

$$MO_x + H_2O \rightarrow MO_x(\cdot OH) + H^+ + e^- \qquad\qquad (1)$$
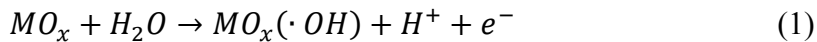
Where MO_x represents the surface sites of the metal oxides electrode for adsorption of $\cdot OH$ species.
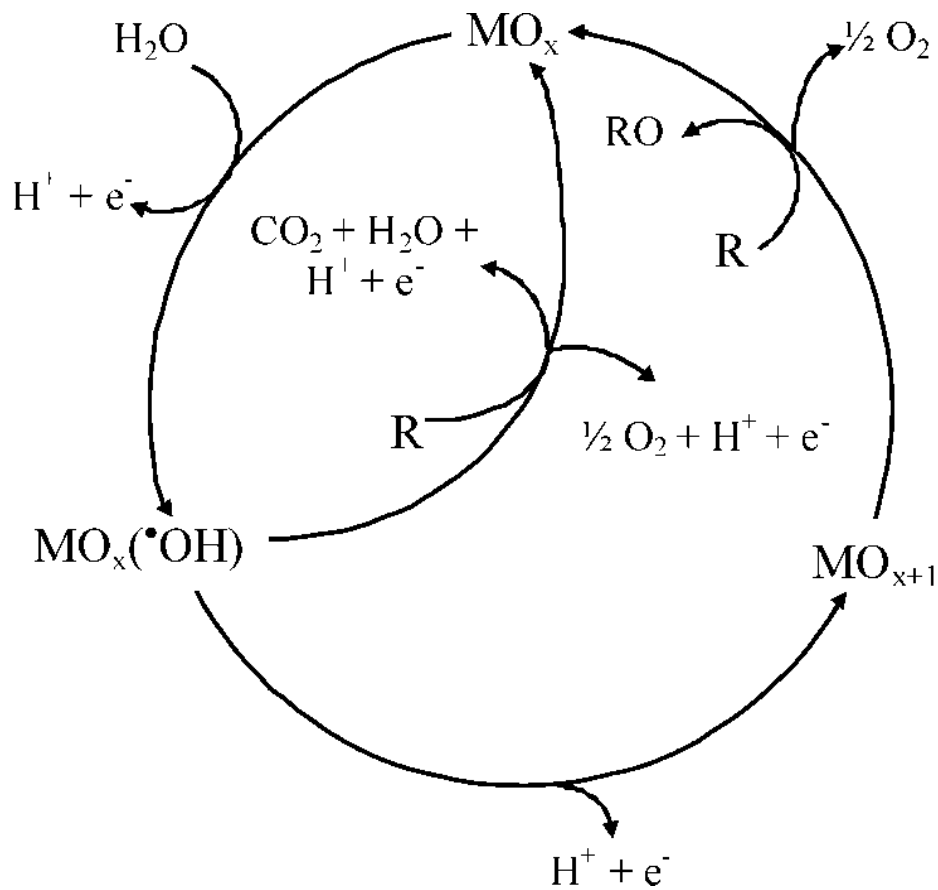
Fig. 2.2 Scheme of the electrochemical oxidation of organic compounds on active and non-active anodes [5].

With *active* electrodes, there is a strong interaction between the electrode and the hydroxyl radical. Adsorbed hydroxyl radicals may interact with the anode, forming a higher oxide. This may be the case when higher oxidation states are available for the electrode material above the thermo-dynamic potential for oxygen evolution.

$$MO_x(\cdot OH) \rightarrow MO_{x+1} + H^+ + e^- \qquad\qquad (2)$$

9
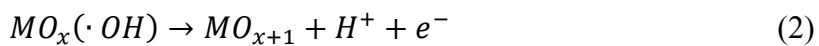
The surface redox couple MO_{x+1}/MO_x can act as a mediator in the conversion or selective oxidation of organics on *active* electrodes:

$$MO_{x+1} + R \rightarrow MO_x + RO \qquad\qquad (3)$$

Typical examples of active electrodes are carbon, graphite, IrO_2, RuO2 and platinum [5].

With *non-active* electrodes, weak interactions exist between the hydroxyl radical and the electrode surface. Thus, the oxidation of organics is mediated by hydroxyl radicals and may result in fully oxidized reaction products such as CO_2:

$$MO_x(\cdot OH) + R \rightarrow MO_x + CO_2 + H_2O + H^+ + e^- \qquad (4)$$
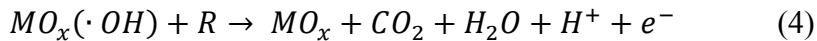
Therefore, the non-active electrodes are ideal candidates for wastewater treatment. Typical examples of non-active elective electrodes are SnO_2, PbO_2 and boron doped diamond (BDD) [5].

However, both of the active and non-active anodes undergo a competitive side reaction, i.e. oxygen evolution, resulting in decreased anodic process efficiency. Additionally, in practice, most anodes will exhibit a mixed behaviour, since both parallel reaction paths participate in organic oxidation and oxygen evolution reactions.

2.1.4   The SnO_2 based anodes

Of the non-active electrodes, SnO_2 anodes are thought to be the most promising electrode for wastewater treatment as PbO_2 anodes have the potential risk of releasing toxic ions, especially in basic solutions, and BDD electrodes suffer from their extremely high cost and the difficulties in finding an appropriate substrate for thin diamond layer deposition [5,24]. However, pure SnO_2 is an n-type semiconductor with a band gap of about 3.5 eV and exhibits very low conductivity at

room temperature; thus cannot be used as an electrode material directly [25]. By doping with antimony (Sb), the electrical conductivity can be significantly increased. Kotz et al. [26] first reported the use of antimony-doped tin dioxide deposited on a titanium base metal (Ti/SnO$_2$-Sb$_2$O$_5$) for electrochemical wastewater treatment. Complete TOC removal of a wide range of organic compounds was obtained independently of pH, with average efficiency five times higher than with Pt anodes. Similar results were also obtained by Comninellis and Pulgarin [20,27] and by Li et al. [24] who used the Ti/SnO$_2$-Sb$_2$O$_5$ electrode for phenol oxidation. This is because SnO$_2$ enabled a rapid removal of phenol oxidation intermediates, mainly aliphatic acids, which were practically inactive on Pt anodes. Later, Grimm et al. [28] compared the oxidation of phenol on Ti/SnO$_2$–Sb$_2$O$_5$ and PbO$_2$ and found that the former was more active. However, the main issue with the Ti/SnO$_2$–Sb$_2$O$_5$ electrode is its short lifetime. As mentioned before, the known failure mechanisms of metal oxides electrodes include selective loss of the catalyst to the electrolyte solution, the formation of a resistive layer between the substrate and coating, and a non-conducting layer formed on the outer surface of the coating. Previous study by Chen et al [29] has shown that the addition of a nano-scale gold thin film on the titanium substrate can effectively prevent the growth of a TiO$_2$ insulating layer between the substrate and the SnO$_2$–Sb$_2$O$_5$ coating, greatly prolonging the service life of the electrode. Correa-Lozano et al. [30] have also shown that an interlayer of IrO$_2$ in the Ti/IrO$_2$/SnO$_2$–Sb$_2$O$_5$ electrode strongly increases the service life of the anode. In a more recent investigation done by Adams et al. [24], four different SnO$_2$-based electrodes: Ti/SnO$_2$–Sb$_2$O$_5$, Ti/SnO$_2$–Sb$_2$O$_5$–PtO$_x$, Ti/SnO$_2$–Sb$_2$O$_5$–RuO$_2$ and Ti/SnO$_2$–Sb$_2$O$_5$–IrO$_2$ were compared, based on their performance in the lifetime test and the degradation efficiency of three Nitro-phenols, Ti/SnO$_2$–Sb$_2$O$_5$–IrO$_2$ outstood the other three electrodes and was selected as the most suitable electrode for wastewater treatment.

2.1.5 Operating conditions and drawbacks of electrochemical oxidation

In addition to the electrode materials, the operating conditions such as current density, temperature, mass transfer, initial concentration of the pollutants, and supporting electrolyte also affect the process efficiency of electrochemical oxidation. Matyasovszky *et al.* [31] employed Plackett-Burman's experimental design to simultaneously investigate the effect of operating conditions on the electrochemical oxidation of SA, revealing that temperature and the applied current density are the two major factors.

The main drawback of the electrochemical oxidation is the high operating cost due to the high energy consumption. Also note that the low concentration of contaminants in some wastewater and the poor conductivity of some waste streams may cause a significant decrease in current efficiency as most of the energy could be wasted in oxygen evolution reactions [32].

2.1.6 Combination of electrochemical oxidation with biological process

Given the limitations of electrochemical oxidation, great efforts are being put into the integration of electrochemical oxidation with biological processes. This system takes advantage of coupling a biodegradation (reduction of operating cost) and a chemical process (shorter retention time). When a wastewater is first subjected to electrochemical oxidation, biodegradability of the organic pollutants is enhanced, improving the performance of the subsequent biological process [33]. More commonly, employment of electrochemical oxidation as a post treatment further destroys the biorefractory organic matter remaining in the effluent after biological treatment. For example, Panizza *et al*. [34] demonstrated that integration of a biofilm airlift suspension (BAS) reactor with electrochemical oxidation by BDD anodes as a post treatment was an effective method for treating a mixture of naphtalenesulfonates. A reduction in energy consumption from

80 to 61 kWh m^{-3} was obtained after coupling the two processes. Other treatment schemes that have been evaluated include: an anaerobic digester followed by electro-oxidation [35], MBRs followed by electrochemical oxidation [36], and an aged-refuse bioreactor (ARB) followed by electrochemical oxidation [37]. The promising results obtained during the treatment of industrial wastes by combined methods involving electrochemical oxidation set the basis for future work. Development of a sustainable process based on the integration of efficient technologies is one of the key obstacles that have to be overcome before the full-scale implementation of electrochemical oxidation [38].

2.2 Membrane Bioreactor Technology for Wastewater Treatment

2.2.1 MBR technology

Membrane bioreactor (MBR) technology, which combines the activated sludge process with a direct solid–liquid separation by membrane filtration, has become an attractive option for the treatment and reuse of wastewaters. By incorporation of micro or ultrafiltration membrane technology, the MBR systems allow the complete physical retention of sludge flocs and virtually all suspended solids within the bioreactor. As a result, the MBR system has many distinct advantages over conventional biological treatment processes. First of all, the MBR can produce high-quality effluent. For example, MBR treatment of municipal wastewater yields high-quality water with reported removal percentages of 95%, 98%, and 99% (or greater) for COD, biochemical oxygen demand (BOD), and suspended solids (SS), respectively [39]. In addition, MBRs have greater (independent) control over the sludge retention time (SRT) and hydraulic retention time (HRT) because membrane filtration rather than gravitational settling is used to separate the biomass from the effluent. This allows for operation at a longer SRT and at higher

loading rates, which results in less sludge production and shorter HRT. Furthermore, MBRs have small footprints and reduced sludge production. MBRs take only half the land area of a conventional activated sludge and sludge production is approximately halved [40-41].

There are two types of configuration for the MBRs system: external vs. submerged. The external MBR is shown in Fig. 2.3a. Mixed liquor is circulated outside of the reactor to the membrane module, where pressure drives the separation of water from the sludge. The concentrated sludge is then recycled back into the reactor. Fig. 2.3b presents a submerged MBR, where the membrane module immerses in the activated sludge. A suction force is applied to draw the water through the membrane, while the sludge is retained on the membrane surface. A manifold at the base of the reactor diffuses compressed air within the reactor, providing oxygen to maintain aerobic conditions. The air bubbles also function to scour the membrane surface and clean the exterior of the membrane as they rise in the reactor. The submerged configuration is more commonly used than the external configuration because it is less energy-intensive and provides a cleaning mechanism to reduce membrane fouling [42]. Thus, more studies focus on the submerged configuration than on the external configuration.
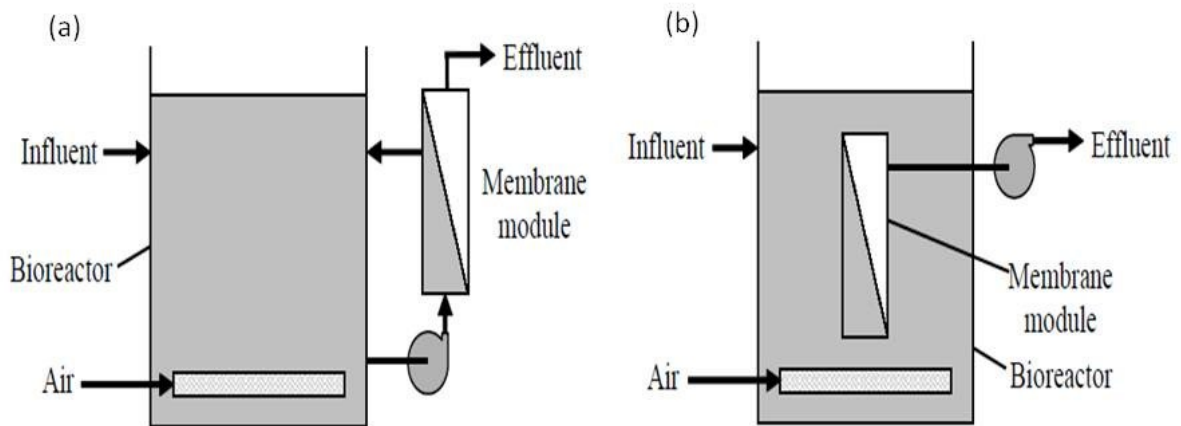
Fig. 2.3 MBRs system configuration: (a) external MBR and (b) submerged MBR [43].

14

The MBR technology has been successfully applied for the treatment of municipal [42,44-45] and industrial [46-48] wastewaters. For example, Itokawa *et al.* [44] analyzed the design and operating data from 17 full-scale municipal MBRs plants in Europe. They found that small footprint and high effluent quality were the decisive factors of MBR installation. Marrot *et al.* [47] provided a detailed literature review of industrial wastewater treatment by MBRs and concluded that the MBR systems have better removal efficiency and a potential for water reuse in manufacturing. However, MBRs have not reached a mature stage, and further development is essential in terms of both membrane modules and process engineering in order for the technology to become more competitive against conventional technologies.

2.2.2 Thermophilic aerobic activated sludge processes and thermophilic aerobic MBRs (TAMBRs)

Thermophilic aerobic activated sludge system represents a unique process for the treatment of high strength and high temperature wastewater. In recent years, thermophilic treatment systems have gained considerable interest due to (i) high biodegradation rate: substrate utilization rates are 3 - 10 times greater than those observed with analogous mesophilic processes; (ii) reduced sludge generation: sludge production rates are generally similar to anaerobic treatment processes; (iii) tolerance of high loading rate, and (iv) excellent process stability [49]. However, thermophilic aerobic processes have been reported to suffer from poor effluent quality, typically measured as higher COD values and turbidity. In particular, a high amount of dispersed particles, such as free bacteria and colloids, increases COD values in thermophilic effluents. Another problem existing in thermophilic treatment is poor floc formation and poor sludge settleability. Possible reasons for the poor thermophilic floc formation along with the formation of dispersed

particles are the higher shear sensitivity of flocs under increased temperatures, leading to erosion of flocs, a decrease in the hydrophobicity of cells, and the absence of floc-forming bacteria [50].

In order to address the issues in the conventional thermophilic aerobic activated sludge process, thermophilic aerobic MBRs (TAMBRs) being able to filter wide ranges of biomass sizes, was developed. The TAMBRs possess both advantages of a thermophilic aerobic activated sludge system and MBR systems and thus increase the possibilities of re-use of treated effluents. In addition, the TAMBRs operate at high temperature, so that the capital and operating costs associated with wastewater pre-cooling for biological treatment and subsequent post-heating for in-mill use could be avoided [51]. Some applications of TAMBRs are summarized in Table 2.1. It is evident that the TAMBRs can achieve high contaminants removal efficiency and thus hold great promise for the incorporation into the industrial process to help industries to reuse the treated water. However, in order to reach the goal of "zero effluent" and system closure, post treatment after the MBRs using chemical methods such as electrochemical oxidation may be needed to decolourize and further lower the COD level in the effluent of TAMBRs.

Table 2.1 TAMBR applications in wastewater treatment

Wastewater	Operating temperature	Membrane configuration	Investigations	Findings	Ref.
Mechanical newsprint mill whitewater	55°C	Ultrafiltration	Compared TAMBR with Ultrafiltration system	Higher removal efficiency of COD and total solids compared to ultrafiltration alone.	[52]
Synthetic wastewater containing α-lactose and gelatin	55°C	Microfiltration	Compared TAMBR with a conventional thermophilic aerobic system and investigated the shift of the bacterial community	Higher COD removal efficiency than conventional thermophilic process. Bacterial community shifts and the specific activity of β-galactosidase and aminopeptidase increased by 10-25%,	[53]
Paper mill effluent	55°C	Ultrafiltration	Evaluate the performance of conventional thermophilic process, TAMBR and mesophilic process.	TAMBR can reach mesophilic COD removal rates. The suspended solids free effluent gives water more possibilities of being reused.	[54]
Kraft pulp mill foul condensates	35°C 45°C 55°C	Ultrafiltration	Tested the system performance at three different temperatures	At 35°C, very high COD, total reduced sulphur and methanol removals achieved. As the temperature increased, a decrease in removal efficiency and respiratory activity was observed. Thermophilic MBR was shown to be technically feasible.	[55]
Landfill leachate	45°C	-	Compared the system performance at different BOD/COD of 0.39, 0.57, 0.65.	The COD removal rate increased while ammonia removal efficiency decreased from gradual increase in BOD. A high BOD removal efficiency (97–99%) The concentrations EPS in TAMBR were higher than the corresponding concentrations in a mesophilic MBR	[56]

2.2.3 Membrane fouling

Membrane fouling is a major obstacle that hinders the faster commercialization of MBRs. As shown in Fig. 2.4, membrane fouling in MBRs can be attributed to both membrane pore clogging and sludge cake deposition on membranes which is usually the predominant fouling component [57]. Membrane fouling results in a reduction of permeate flux or an increase of transmembrane pressure (TMP) depending on the operation mode.
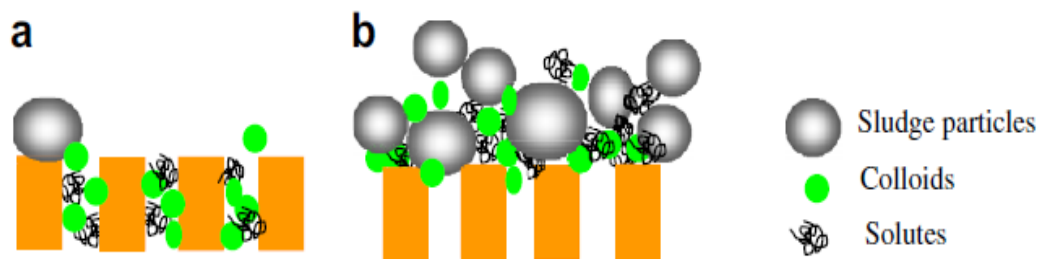
Fig. 2.4 Membrane fouling process in MBRs: (a) pore blocking and (b) cake layer [58].

With respect to MBRs, membrane fouling occurs due to the following mechanisms: (1) adsorption of solutes or colloids within/on membranes; (2) deposition of sludge flocs onto the membrane surface; (3) formation of a cake layer on the membrane surface; (4) detachment of foulants attributed mainly to shear forces; and (5) the spatial and temporal changes of the foulant composition during the long-term operation (e.g., the change of bacteria community and biopolymer components in the cake layer).

The fouling of MBRs can be classified into three major categories: biofouling, organic fouling, and inorganic fouling. Biofouling refers to the deposition, growth and metabolism of bacteria cells or flocs on the membranes. It may start with the deposition of an individual cell or cell cluster on the membrane surface, after which the cells multiply and form a cake layer, which has

a significant influence on the membrane filtration processes. Lee *et al.* [57] and Bae *et al.* [59] and Hwang *et al.* [60] reported that the cake layer resistance in the MBRs was 80%, 92 - 95% and 93.9%, respectively, indicating that the formation of cake layer is the main cause leading to membrane fouling. Organic fouling in MBRs refers to the deposition of biopolymers (i.e. proteins and polysaccharides) on the membranes. Due to the small size, the biopolymers can be deposited onto the membranes more readily promoted by the permeate flow. Metzger *et al.* [61] conducted a more detailed study to characterize organic fouling in MBRs and revealed the spatial distribution of biopolymers on the membrane surface. Inorganic fouling can form through chemical precipitation and biological precipitation. Most researchers attribute membrane fouling to the deposition of sludge flocs and biopolymers and, thus, inorganic fouling is considered as an insignificant factor in membrane fouling.

Bound and soluble extracellular polymeric substances (EPS) are currently considered as the predominant cause of membrane fouling in MBRs [58]. Bound EPS consist of proteins, polysaccharides, nucleic acids, lipids, humic acids, etc. which are located at or outside the cell surface. Soluble EPS can be defined as the pool of organic compounds that are released into solution from substrate metabolism (usually with biomass growth) and biomass decay [62]. Bound EPS have been reported not only as major sludge floc components keeping the floc in a three-dimensional matrix, but also as key membrane foulants in MBR systems [63-65]. For example, Ahmed *et al.* [64] observed that as bound EPS concentration rose, the specific cake resistance increased, and this consequently resulted in the rise of TMP. In addition to bound EPS, soluble EPS have also been recognized as significant contributors to membrane fouling [66-67]. Due to the membrane rejection, the soluble EPS is more easily accumulated in MBRs, which results in the poor filterability of the sludge suspension. Geng and Hall [68] observed that the

particle size distribution and the amount of soluble EPS in the mixed liquor were the most important properties that significantly influenced the fouling propensity of sludge. These investigations suggest that the bound EPS concentrations are closely connected to sludge characteristics such as flocculation ability, hydrophobicity, surface charge, and sludge viscosity and the soluble EPS impact on membrane fouling more directly. The concentration and composition of the soluble EPS would determine the fouling propensity of the MBR systems.

Although membrane fouling has been identified as the most challenging issue with MBRs, there is very limited information related to the membrane fouling of the thermophilic aerobic MBRs (TAMBRs). Kurian *et al.* [69] performed a long-term study on TAMBRs for the treatment of oily pet food wastewater at a low flux of 0.8 L m^{-2} h^{-1} and found that the cleaning the encapsulated membrane was more and more difficult which resulted in a gradual and irrecoverable decrease in flux over time. Visvanathan *et al.* [56] reported that the concentrations of soluble and bound EPS in TAMBRs were 2.5 times higher when compared to the EPS concentration in analogue mesophilic MBRs. The higher EPS concentration led to a higher rate of fouling in the TAMBR. However, the ratio of protein to carbohydrate (PN/CH) was higher in a mesophilic MBR, indicating that the thermophilic bacterial populations preferred utilizing protein-like material as a carbon source. The literature also suggests that thermophilic sludge contains significantly higher number of small particles compared to mesophilic sludge. For example, in a study conducted by Vogelaar *et al.* [70], the volume percentage of sludge particles with a diameter of less than 5 mm was 16% for thermophilic sludge and only 4% for mesophilic sludge. The TAMBRs hold great potential for effective and energy-saving treatment of wastewater within industrial processes, so it is of great interest to understand the membrane fouling mechanisms in the TAMBRs systems.

2.3 Electrochemical Methods for Chemical Oxygen Demand Determination

2.3.1 Chemical oxygen demand (COD) and its conventional determination

The oxygen demand of water and wastewater represents one of the most important measurable parameters for water quality. At present, two standard analytical methodologies are in widespread use for the determination of the oxygen demand of waters and wastewaters. These are biochemical oxygen demand (BOD) and chemical oxygen demand (COD). Of the two, COD is a preferred method to BOD for assessing the oxygen demand of organic pollutants in heavily polluted water bodies. This is because it needs less analysis time than the standard BOD method (i.e. 5 days) and it is immune from organic and inorganic poisons. The standard method for COD analysis consists of oxidizing organic matter of the sample, adding a known amount of oxidant, refluxing at high temperature on open containers and titrating the excess oxidant [71]. On the basis of the oxidizers used, the standard COD methods can be classified into either the dichromate method or the permanganate method. Due to its higher degradation degree to a wide range of the organic pollutions, the dichromate method has been extensively used and is more popular than the permanganate method. However, this standard method is limited by long reflux times (approximately 2 – 2.5 h), volatilisation of organics, and tedious manual procedures with the potential for error. In view of these drawbacks, an ideal method suitable for determination of COD should be quick, simple, cheap and as accurate as the standard method.

A great deal of effort has been devoted to the development of other suitable methods. Microwave heating and ultrasonic radiation were used to considerably shorten the time of digestion step [72-75]. However, these fast digestion steps still need the use of some expensive (Ag_2SO_4) and toxic ($HgSO_4$) chemicals. In this context, developing rapid and environmentally friendly methods for

COD determination has attracted much attention. Most of these new developments are based either on electrocatalytic or photoelectrocatalytic methods.

2.3.2 Electrocatalytic and photoelectrocatalytic methods for COD determination

The principle of electrocatalytic methods for rapid COD determination was proposed as follows: First, H_2O is discharged at the anode to produce physisorbed hydroxyl radicals on the surface of the electrode:

$$E[\ ] + H_2O \xrightarrow{k_1} E(\dot{\ }OH) + H^+ + e^- \tag{1}$$

In Eq. (1), E[ ] represents unoccupied surface sites where the discharge reaction is assumed to be constant and the back reaction for H_2O discharge is ignored; k_1 is the electrochemical rate constant for H_2O discharge; $E(\dot{\ }OH)$ corresponds to adsorbed hydroxyl radicals. The hydroxyl radical is a non-selective, very powerful oxidizing agent and is able to react with organic compounds according to Eq. (2):

$$R + E(\dot{\ }OH) \xrightarrow{k_2} E[\ ] + RO + H^+ + e^- \tag{2}$$

Where R is the reactant and k_2 is the electrochemical rate constant for the oxidation of organics. The concomitant evolution of oxygen is given by equation (3):

$$E(\dot{\ }OH) + H_2O \xrightarrow{k_3} E[\ ] + O_{2\ (aq)} + 3H^+ + 3e^- \tag{3}$$
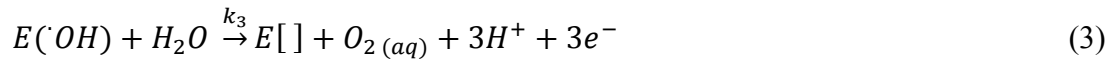
According to Popovic and Johnson [76], equation (4) could be derived from equations (1) – (3) to quantitatively describe the oxygen transfer reaction:

$$i_{tot} = 2FA\Gamma_0 k_2 C_R \tag{4}$$

Where Γ_0 is the density (mol cm^{-2}) of surface sites available for the adsorption of ·OH radicals, A (cm^2) is the area of the electrodes, F (96487 C mol^{-1}) the Faraday constant and C_R the surface concentration of the reactant.

According to equation (4), any variation of the organic compounds in the water would cause a change in the current responding to this solution. In all cases, the current increased proportionately with increased concentration of organic compounds in the sample solution. This indicated that the COD value was proportional to the current responses of the working electrode. For example, in the studies of Li *et al.* [77] and Silva *et al.* [78], a good linear relationship between the current and COD value was found, respectively, as shown in Fig. 2.5.

Similarly, for the photoelectrocatalytic determination of COD, both the linear relationships of photocurrent vs. COD and net charge vs. COD could be well established according to the principles proposed by Li *et al.* [79] and Zheng *et al.* [80]. The calibration plot of photocurrent vs. COD and net charge vs. COD values are presented in Fig. 2.6.
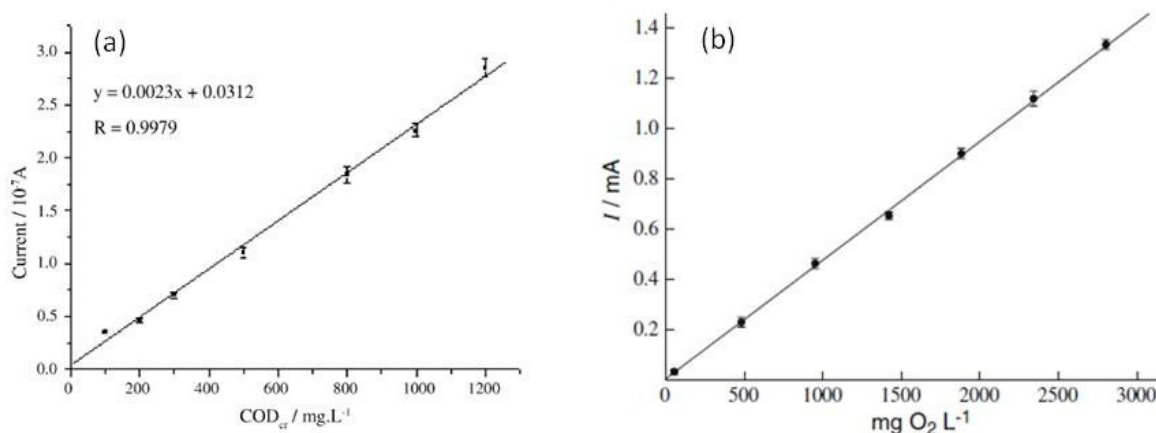
Fig. 2.5 Calibration curve of current signal as a function of COD value in electrocatalytic method: (a) F-PbO$_2$ electrode [77] and (b) Cu/CuO electrode [78].
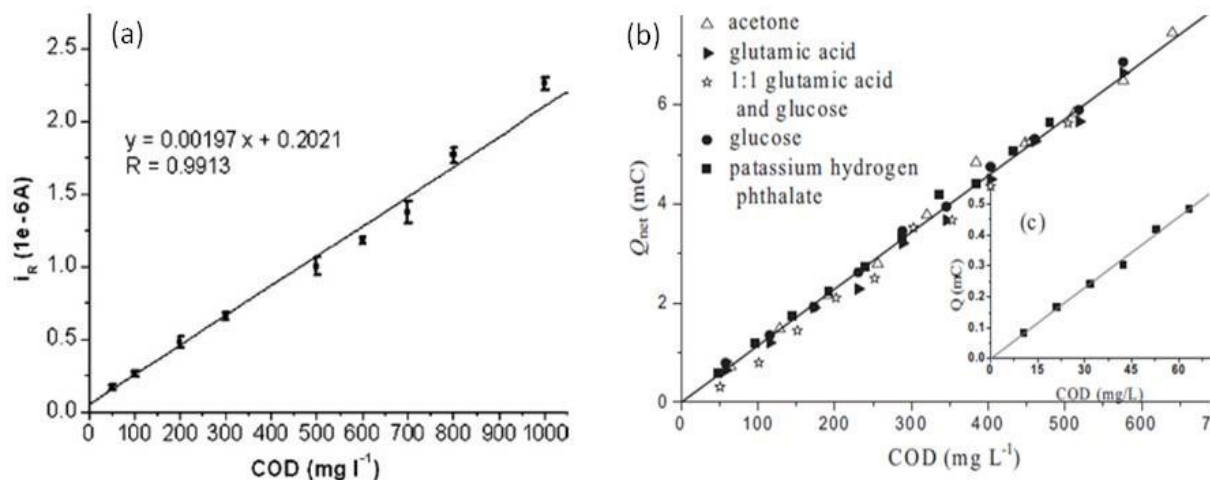
Fig. 2.6 Calibration curve of (a) photocurrent [79] and (b) net charge [80] as a function of COD value in photoelectrocatalytic method.

The rapid determination of COD can be performed either in a conventional three-electrode cell or in a thin layer three-electrode cell where a very small amount of sample is added. The thin layer cell used in the study of Li *et al.* [79] is shown in Fig. 2.7. This cell configuration is preferred when the determination is based on the net charge as a function of COD [80-81], because the minute amount of sample is more readily completely oxidized than the large amount usually used in conventional electrochemical cells.

Some typical works using electrocatalytic and photoelectrocatalytic methods for the rapid COD determination are summarized in Table 2.2. The performance varies greatly based on the electrode materials that were used. For instance, the portable UV-LED device developed by Zhang *et al.* [82] is more suitable for slightly polluted wastewater determination as it has a small practical detection range and a low detection limit. In contrast, the electrochemical method using BDD electrode exhibited a wide detection range of 20 – 9000 mg/L, which can be used for the COD determination of a variety of wastewaters.
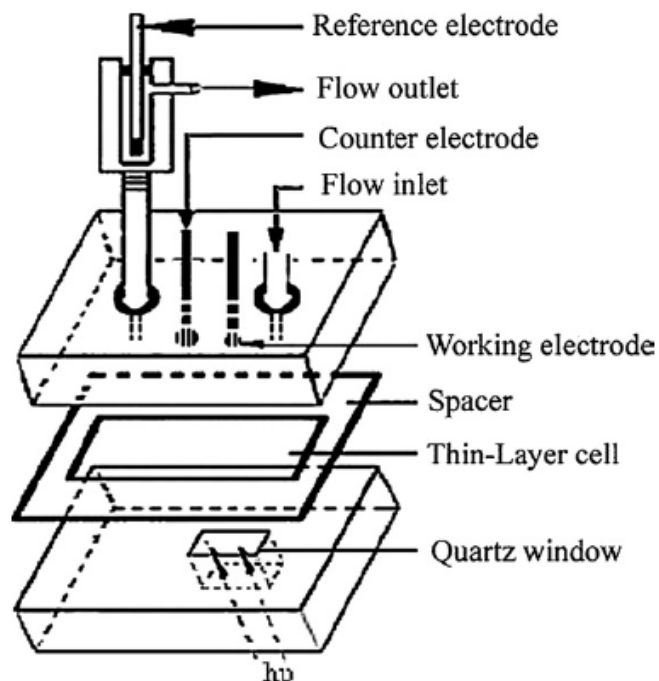
Fig. 2.7 The thin layer three electrode cell [96].

All the results obtained from the literature suggest that the COD values determined by the proposed electrocatalytic and photoelectrocatalytic method are within a small relative standard deviation of those by the conventional COD method. The proposed methods have the advantages of short analysis time, simple instrumentation and low environmental impact. As a result, the electrocatalytic and photoelectrocatalytic methods for the determination of COD are promising alternatives for the conventional method.

Table 2.2 Electrochemical and photoelectrochemical determination of COD

Methods	Electrodes	Cell configuration	Measuring parameter	Detection range (mg/L)	Detection limit (mg/L)	Ref.
Electrocatalytic	Pt-ring + Pt/PbO2-disc	Conventional three-electrode	Current	20 – 5000	15	[83]
	Nano-PbO2	Conventional three-electrode	Current	5 – 3000	2.5	[84]
	F-PbO$_2$	Thin layer three-electrode	Current	100 – 1200	15	[77]
	BDD	Conventional three-electrode	Current	20 – 9000	7.5	[85]
	Cu/CuO	Conventional three-electrode	Current	53.0 – 2801.4	20.3	[78]
Photo-electrocatalytic	TiO$_2$ thin film	Thin layer three-electrode	Charge	0 - 200	0.2	[86]
	TiO$_2$ film	Conventional three-electrode	Photocurrent	0.5 – 235	-	[87]]
	Ti/TiO$_2$	Conventional three-electrode	Photocurrent	50 – 2000	16	[88]
	TiO$_2$ nanotubes	Thin layer three-electrode	Charge	0 – 700	-	[80]
	TiO$_2$ nanoparticles	Portable Thin layer three-electrode	Photocurrent	0 – 120	0.2	[82]

References

[1]   D. R. Medley, E. L. Stover, *J. Water Pollut. Control Fed.* **1983**, *55*, 489.

[2]   E. Brillas, I. Sirés, M. A. Oturan, *Chem. Rev.* **2009**, *109*, 6570.

[3]   X. Y. Li, Y. H. Cui, Y. J. Feng, Z. M. Xie, J. D. Gu, *Water Res.* **2005**, *39*, 1972.

[4]   R. Andreozzi, V. Caprio, A. Insola, R. Marotta, *Catal. Today* **1999**, *53*, 51.

[5]   M. Panizza, G. Cerisola, *Chem. Rev.* **2009**, *109*, 6541.

[6]   C. A. Martinez-Huitle, S. Ferro, *Chem. Soc. Rev.* **2006**, *35*, 1324.

[7]   A. Anglada, A. Urtiaga, I. Ortiz, *J. Chem. Technol. Biotechnol.* **2009**, *84*, 1747.

[8]   A. G. Vlyssides, M. Loizidou, P. K. Karlis, A. A. Zorpas, D. Papaioannou, *J. Hazard. Mater.* **1999**, *70*, 41.

[9]   A. S. Koparal, Y. Yavuz, C. Gürel, Ü. B. Ögütveren, *J. Hazard. Mater.* **2007**, *145*, 100.

[10]   N. Mohan, N. Balasubramanian, C. A. Basha, *J. Hazard. Mater.* **2007**, *147*, 644.

[11]   R. Cossu, A. M. Polcaro, M. C. Lavagnolo, M. Mascia, S. Palmas, F. Renoldi, *Environ. Sci. Technol.* **1998**, *32*, 3570.

[12]   Y. Deng, J. D. Englehardt, *Waste Manage.* **2007**, *27*, 380.

[13]   A. Anglada, A. Urtiaga, I. Ortiz, *Environ. Sci. Technol.* **2009**, *43*, 2035.

[14]   M. Panizza, G. Cerisola, *Environ. Sci. Technol.* **2004**, *38*, 5470.

[15]   H. P. Chang, D. C. Johnson, *J. Electrochem. Soc.* **1990**, *137*, 2452.

[16]   J. R. Feng, D. C. Johnson, *J. Electrochem. Soc.* **1991**, *138*, 3328.

[17]   J. R. Feng, D. C. Johnson, S. N. Lowery, J. J. Carey, *J. Electrochem. Soc.* **1994**, *141*, 2708.

[18]   S. K. Johnson, L. L. Houk, J. R. Feng, R. S. Houk, D. C. Johnson, *Environ. Sci. Technol.* **1999**, *33*, 2638.

[19]   D. C. Johnson, J. Feng, L. L. Houk, *Electrochim. Acta* **2000**, *46*, 323.

[20]   C. Comninellis, *Electrochim. Acta* **1994**, *39*, 1857.

[21]   C. Comninellis, A. DeBattisti, *J. Chim. Phys. Phys.- Chim. Biol.* **1996**, *93*, 673.

[22]   O. Simond, V. Schaller, C. Comninellis, *Electrochim. Acta* **1997**, *42*, 2009.

[23]   G. Foti, D. Gandini, C. Comninellis, A. Perret, W. Haenni, *Electrochem. Solid-State Lett.* **1999**, *2*, 228.

[24]   B. Adams, M. Tian, A. Chen, *Electrochim. Acta* **2009**, *54*, 1491.

[25]   X. M. Chen, F. R. Gao, G. H. Chen, *J. Appl. Electrochem.* **2005**, *35*, 185.

[26]   R. Kotz, S. Stucki, B. Carcer, *J. Appl. Electrochem.* **1991**, *21*, 14.

[27]   C. Comninellis, C. Pulgarin, *J. Appl. Electrochem.* **1993**, *23*, 108.

[28]   J. Grimm, D. Bessarabov, R. Sanderson, *Desalination* **1998**, *115*, 285.

[29]   A. C. Chen, S. Nigro, *J. Phys. Chem. B* **2003**, *107*, 13341.

[30]   B. CorreaLozano, C. Comninellis, A. DeBattisti, *J. Appl. Electrochem.* **1997**, *27*, 970.

[31]   N. Matyasovszky, M. Tian, A. Chen, *J Phys Chem A* **2009**, *113*, 9348.

[32]   A. M. Polcaro, S. Palmas, *Ind. Eng. Chem. Res.* **1997**, *36*, 1791.

[33]   P. A. Soloman, C. Ahmed Basha, M. Velan, N. Balasubramanian, P. Marimuthu, *Sep. Purif. Technol.* **2009**, *69*, 109.

[34]   M. Panizza, M. Zolezzi, C. Nicolella, *J. Chem. Technol. Biotechnol.* **2006**, *81*, 225.

[35]   K. J. Chae, S. K. Yim, K. H. Choi, S. K. Kim, W. K. Park, *Water Sci. Technol.* **2004**, *49*, 427.

[36]   F. Aloui, F. Fki, S. Loukil, S. Sayadi, *Water Sci. Technol.* **2009**, *60*, 605.

[37]   Y. M. Lei, Z. M. Shen, R. H. Huang, W. H. Wang, *Water Res.* **2007**, *41*, 2417.

[38]   C. Comninellis, A. Kapalka, S. Malato, S. A. Parsons, L. Poulios, D. Mantzavinos, *J. Chem. Technol. Biotechnol.* **2008**, *83*, 769.

[39]   A. N. L. Ng, A. S. Kim, *Desalination* **2007**, *212*, 261.

[40]   S. Judd, *Trends Biotechnol.* **2008**, *26*, 109.

[41]   P. Le-Clech, V. Chen, T. A. G. Fane, *J. Membr. Sci.* **2006**, *284*, 17.

[42]   M. Gander, B. Jefferson, S. Judd, *Sep. Purif. Technol.* **2000**, *18*, 119.

[43]   G. Tchobanoglous, F. L. Burton, H. D. Stensel *Wastewater engineering :treatment and reuse /Metcalf & Eddy, Inc*; 4th ed.; McGraw-Hill: Boston, 2003.

[44]   H. Itokawa, C. Thiemig, J. Pinnekamp, *Water Sci. Technol.* **2008**, *58*, 2319.

[45]   M. Kraume, U. Bracklow, M. Vocks, A. Drews, *Water Sci. Technol.* **2005**, *51*, 391.

[46]   P. Artiga, E. Ficara, F. Malpei, J. M. Garrido, R. Mendez, *Desalination* **2005**, *179*, 161.

[47]   B. Marrot, A. Barrios-Martinez, P. Moulin, N. Roche, *Environ. Prog.* **2004**, *23*, 59.

[48]   P. Cornel, S. Krause, *Water Sci. Technol.* **2006**, *53*, 37.

[49]   T. M. Lapara, J. E. Alleman, *Water Res.* **1999**, *33*, 895.

[50]   J. Suvilampi, A. Lehtomaki, J. Rintala, *Water Res.* **2005**, *39*, 741.

[51]   P. R. Berube, E. R. Hall, *Water Res.* **2000**, *34*, 4359.

[52]   C. S. F. Ragona, E. R. Hall, *Water Sci. Technol.* **1998**, *38*, 307.

[53]   T. M. LaPara, A. Konopka, C. Nakatsu, J. E. Alleman, *J. Ind. Microbiol. Biotechnol.* **2001**, *26*, 203.

[54]   J. Lopetegui, L. Sancho, *Membranes in Drinking and Industrial Water Production Iii* **2003**, 245.

[55]   J. C. T. Dias, R. P. Rezende, C. M. Silva, V. R. Linardi, *Process Biochem.* **2005**, *40*, 1125.

[56] C. Visvanathan, M. K. Choudhary, M. T. Montalbo, V. Jegatheesan, *Desalination* **2007**, *204*, 8.

[57] J. Lee, W. Y. Ahn, C. H. Lee, *Water Res.* **2001**, *35*, 2435.

[58] F. Meng, S.-R. Chae, A. Drews, M. Kraume, H.-S. Shin, F. Yang, *Water Res.* **2009**, *43*, 1489.

[59] T. H. Bae, T. M. Tak, *J. Membr. Sci.* **2005**, *264*, 151.

[60] B.-K. Hwang, W.-N. Lee, P.-K. Park, C.-H. Lee, I.-S. Chang, *J. Membr. Sci.* **2007**, *288*, 149.

[61] U. Metzger, P. Le-Clech, R. M. Stuetz, F. H. Frimmel, V. Chen, *J. Membr. Sci.* **2007**, *301*, 180.

[62] D. J. Barker, D. C. Stuckey, *Water Res.* **1999**, *33*, 3063.

[63] J. Cho, K. G. Song, H. Yun, K. H. Ahn, J. Y. Kim, T. H. Chung, *Water Sci. Technol.* **2005**, *51*, 9.

[64] Z. Ahmed, J. Cho, B.-R. Lim, K.-G. Song, K.-H. Ahn, *J. Membr. Sci.* **2007**, *287*, 211.

[65] L. Ji, J. T. Zhou, *J. Membr. Sci.* **2006**, *276*, 168.

[66] S. Rosenberger, H. Evenblij, S. T. Poele, T. Wintgens, C. Laabs, *J. Membr. Sci.* **2005**, *263*, 113.

[67] S. Rosenberger, C. Laabs, B. Lesjean, R. Gnirss, G. Amy, M. Jekel, J. C. Schrotter, *Water Res.* **2006**, *40*, 710.

[68] Z. H. Geng, E. R. Hall, *Water Res.* **2007**, *41*, 4329.

[69] R. Kurian, C. Acharya, G. Nakhla, A. Bassi, *Water Res.* **2005**, *39*, 4299.

[70] J. C. T. Vogelaar, A. De Keizer, S. Spijker, G. Lettinga, *Water Res.* **2005**, *39*, 37.

[71]   A. D. Eaton, M. A. H. Franson, *Standard Methods for the Examination of Water and Wastewater*; 21st ed.; American Public Health Association: Washington, DC, 2005.

[72]   E. Axen, G. M. Morrison, *International Int. J. Environ. Anal. Chem.* **1995**, *59*, 69.

[73]   R. Ramon, F. Valero, M. del Valle, *Anal. Chim. Acta* **2003**, *491*, 99.

[74]   A. Canals, A. Cuesta, L. Gras, M. R. Hernandez, *Ultrason. Sonochem.* **2002**, *9*, 143.

[75]   C. E. Domini, M. Hidalgo, F. Marken, A. Canals, *Anal. Chim. Acta* **2006**, *561*, 210.

[76]   N. D. Popovic, D. C. Johnson, *Anal. Chem.* **1998**, *70*, 468.

[77]   J. Q. Li, L. P. Li, L. Zheng, Y. Z. Xian, S. Y. Ai, L. T. Jin, *Anal. Chim. Acta* **2005**, *548*, 199.

[78]   C. Silva, C. D. C. Conceicao, V. Bonifacio, O. Fatibello, M. Teixeira, *J. Solid State Electrochem.* **2009**, *13*, 665.

[79]   J. Q. Li, L. Zheng, L. P. Li, G. Y. Shi, Y. Z. Xian, L. T. Jin, *Meas. Sci. Technol.* **2007**, *18*, 945.

[80]   Q. Zheng, B. X. Zhou, J. Bai, L. H. Li, Z. J. Jin, J. L. Zhang, J. H. Li, Y. B. Liu, W. M. Cai, X. Y. Zhu, *Adv. Mater.* **2008**, *20*, 1044.

[81]   S. Q. Zhang, H. J. Zhao, *Analyst* **2008**, *133*, 1684.

[82]   S. Q. Zhang, L. H. Li, H. J. Zhao, *Environ. Sci. Technol.* **2009**, *43*, 7810.

[83]   P. Westbroek, E. Temmerman, *Anal. Chim. Acta* **2001**, *437*, 95.

[84]   S. Y. Ai, M. N. Gao, Y. Yang, J. Q. Li, L. T. Jin, *Electroanalysis* **2004**, *16*, 404.

[85]   H. B. Yu, H. Wang, X. Quan, S. Chen, Y. B. Zhang, *Electrochem. Commun.* **2007**, *9*, 2280.

[86]   H. J. Zhao, D. L. Jiang, S. Q. Zhang, K. Catterall, R. John, *Anal. Chem.* **2004**, *76*, 155.

[87] J. S. Chen, J. D. Zhang, Y. Z. Xian, X. Y. Ying, M. C. Liu, L. T. Jin, *Water Res.* **2005**, *39*, 1340.

[88] J. Q. Li, L. Zheng, L. Li, G. Y. Shi, Y. Z. Xian, L. T. Jin, *Electroanalysis* **2006**, *18*, 1014.

Chapter 3. Materials and Methods

3.1 Introduction

In the previous chapters, some new and effective technologies for wastewater remediation and rapid COD determination were discussed. Also, the objectives for this thesis research were outlined. In this chapter, the main experimental methodology and techniques used in this M. Sc. Eng. project will be briefly introduced. For clarification, the details on the experimental procedures and equipment pertaining to each specific study will be presented in Chapters 4 – 6.

3.2 Chemicals and Materials

The following chemicals were used as received from Sigma-Aldrich (St. Louis, MO, USA): phenol (99+%), p-NPh (99+%), p-cresol (99%), hydrofluoric acid (50%), $H_2PtCl_6 \cdot 6H_2O$, D-glucose ($\geq$ 99.5%), potassium hydrogen phthalate (99.95%), lactic acid, maleic acid (99%), , sodium sulphate (97%), sodium chloride ($\geq$ 99%) , sodium phosphate (98+%), sodium dihhydrogen phosphate (98-102%) sulfuric acid (95-98%), nitrogen chloride ($\geq$ 99.5%), potassium chloride (99-100.5%), potassium dihydrogen phosphate ($\geq$ 99%) and Dowex${}^{\circledR}$ Marathon${}^{\circledR}$ C, sodium form, cation exchange resin.

The following chemicals and materials were used as received from Alfa-Aesar (Ward Hill, MA, USA): titanium wire (99.7%, 2 mm diameter), titanium strip (99.2%, 1.25 cm × 0.5 mm), Pt wire (99.9%, 0.5 mm diameter).

The thermomechanical pulping pressate and the microfiltration membrane used in the membrane bioreactor study were provided by Abitibi-Bowater Inc. (Thunder bay, ON, Canada) and SINAP Membrane Science & Technology Co. Ltd (Shanghai, China), respectively.

Pure water (18 MΩcm) obtained from a NANOpure® Diamond™ UV ultrapure water purification system (Thermo Scientific, Dubuque, IA, USA) was used for cleaning purposes and preparation of all solutions.

3.3 Experiments

3.3.1 Membrane bioreactor set-up

A lab-scale thermophilic submerged aerobic membrane bioreactor (TSAMBR) system was constructed, which consisted of a fridge, a water bath, a feed pump, a pH regulation pump, aeration pumps, a permeate peristaltic pump, a level sensor and a membrane bioreactor with a submerged flat sheet microfiltration membrane module. This system was operated for the treatment of thermomechanical pressate at $51 \pm 1°C$ for over 5 months. The details of the system and the operation conditions will be elucidated in Chapter 5.

3.3.2 Membrane bioreactor sludge characterization

The characterization of bulk and cake sludge in the TSAMBR system included: mixed liquor suspended solid (MLSS) determination [1], bound EPS extraction and measurement [2], particle size distribution, cake layer cryosection [3], and conventional optical microscopic observation. The detailed methods will be provided in Chapter 5.

3.3.3 Fabrication of electrodes

The Ti/SnO_2-Sb_2O_5-IrO_2 electrodes used in electrochemical oxidation studies (Chapter 4 and 5) were prepared by a thermal decomposition method [4]. The $TiO_2/Ti/TiO_2$-Pt bifunctional electrodes used in the study of photoelectrochemical determination of COD (Chapter 6) were

fabricated using a two-step method of anodic oxidation followed by photo-assistant deposition [5].

3.3.4 Surface analysis

The surface morphology of the fabricated electrodes was characterized using a JEOL JSM 590LV (Japan) scanning electron microscope (SEM). Surface composition was examined by an Oxford Links ISIS (U.K.) energy dispersive X-ray spectrophometer (EDS), and the crystallographic properties were analyzed using X-ray diffraction (XRD) (Pananalytical X'pert Pro Diffractometer, Netherlands)

3.3.5 Electrochemical systems and techniques

For the electrochemical oxidation experiments, a two-electrode cell system and an Arbin Instruments power supply (College Station, TX, USA) controlled by a computer were used. The working electrode was the as-prepared $Ti/SnO_2-Sb_2O_5-IrO_2$. The counter electrode used was a Pt wire coil and this was cleaned before each experiment by flame annealing and quenching with pure water. For the electrochemical determination of COD experiments, a three-electrode cell system and a CHI 660B electrochemical workstation were used. The working electrode was the $TiO_2/Ti/TiO_2-Pt$ bifunctional electrode; the counter electrode was a Pt wire coil and the reference electrode was an Ag/AgCl (saturated KCl) electrode. All experiments were performed at room temperature (22±2 °C).

Electrochemical techniques such as cyclic voltammetry (CV), Linear sweep voltammetry (LSV) and chronoamperometry (CA) were used in the electrochemical experiments.

3.3.6 Water Quality Measurements

The COD and total suspended solids (TSS) of the wastewater before and after treatment was analyzed as described in Standard Methods (APHA, 2005) [1]. UV-vis spectroscopy was also used for monitoring the pollutants concentration in the electrochemical oxidation study presented in Chapter 4.

3.4 Summary

This chapter outlines the chemicals and materials used throughout the research project. The experimental methods, techniques and equipments used in the membrane bioreactors study and electrochemical study were briefly described. The following chapter will present a study of enhanced electrochemical oxidation of phenolic compounds in wastewater by an effective pre-concentration process.

References

[1]   A. D. Eaton, M. A. H. Franson, *Standard Methods for the Examination of Water and Wastewater*; 21st ed.; American Public Health Association: Washington, DC, 2005.

[2]   H. J. Lin, K. Xie, B. Mahendran, D. M. Bagley, K. T. Leung, S. N. Liss, B. Q. Liao, *J. Membr. Sci.* **2010**, *361*, 126.

[3]   W. J. Gao, H. J. Lin, K. T. Leung, H. Schraft, B. Q. Liao, *J. Membr. Sci.* **2011**, *374*, 110.

[4]   X. Qu, M. Tian, B. Liao, A. Chen, *Electrochimi. Acta* **2010**, *55*, 5367.

[5]   X. Qu, M. Tian, S. Chen, B. Liao, A. Chen, *Electroanalysis* **2011**, *23*, 1267.

Chapter 4. Enhanced Electrochemical Oxidation of Phenolic Pollutants Based on an Effective Pre-concentration Process*

4.1 Introduction

Water pollution, especially in industrial wastewater containing organic compounds, is one of the most urgent environmental problems. Phenolic compounds are a group of common organic pollutants existing in the effluents of coking, oil refineries, production of pesticides and herbicides, dyes and textiles, pharmaceuticals, pulp and paper, plastics, and detergent [1-3]. Due to the wide prevalence of phenolic compounds in different wastewaters and their high toxicity, high oxygen demand and low biodegradability, it is essential to remove them before the discharging of wastewater into water bodies [4-7]. Various methods such as adsorption [7-8], extraction with solvents [9], membrane separation [10], and advanced oxidation processes including Fenton oxidation, ozonation, wet air oxidation, photocatalytic oxidation and electrochemical oxidation have been widely studied for the treatment of the wastewater containing phenolic compounds [1,11]. Among them, adsorption technology is currently being used extensively for the removal of phenolic compounds from aqueous solutions [4,12] and electrochemical oxidation is becoming one of the most promising techniques for the degradation of phenolic compounds in wastewater [13-15].

Adsorption is a simple and efficient method to remove organics from wastewater. Activated carbon is the most widely used adsorbent due to its large specific surface area and predominant proportion of micropores. However, high regeneration cost and poor mechanical rigidity of activated carbon limit its wider applications. Polymeric adsorbents, especially hyper-cross-linked resin, have been considered as a practical alternative to activated carbon. A hyper-cross-linked

---

*This chapter has been published in *Electrochimica Acta* **2010**, 55 (19), 5367-74.

resin has relatively high surface area, high removal efficiency, superior mechanical rigidity and feasible regeneration [5,16]. Various polymeric adsorbents have been investigated and different adsorption mechanisms have been proposed [4,17-20]. However, adsorption is only a process of transferring the pollutants from an aqueous solution to a solid phase and no degradation is achieved. In order to eliminate the pollutants, further steps need to be taken.

Electrochemical oxidation is a promising approach to the destruction of biorefractory organic pollutants and the remediation of wastewater [13-15,21-22]. The electrochemical oxidation of phenolic compounds has been reported on different anodes such as Pt, dimensionally stable anodes (DSA$^®$) and boron doped diamond (BDD) electrodes [2-3,23-26]. Although electrochemical oxidation possesses many advantages, it is not widely applied in wastewater treatment due to its low current efficiency and high cost caused mainly by low concentrations of contaminants and the poor conductivity of most wastewater streams [21,27-28]. It is a challenge to develop efficient electrochemical oxidation processes for wastewater treatment.

The aim of this study is to demonstrate a novel approach based on an effective adsorption and release process to enhance the electrochemical oxidation of phenolic compounds. This new technique overcomes the problem of non-degradability in adsorption by completing eliminating the pollutants in the following electrochemical oxidation process. More importantly, the adsorption and release process improves the efficiency of electrochemical oxidation: the mass transfer of the pollutants from the bulk solution to the surface of the electrode can be significantly enhanced due to the immensely increased concentration achieved by the adsorbing of the pollutants and releasing them into a solution of a much smaller volume; the conductivity of the initial wastewater can be greatly increased due to the employment of a strong NaOH electrolyte as the releasing reagent. Three phenolic pollutants, phenol, p-NPh (containing the

electro-withdrawing $-NO_2$ group) and *p*-cresol (containing the electro-donating $-CH_3$ group) were selected as the model pollutants in this study. The adsorption serving as a pre-concentration process was carried out by adsorbing the three pollutants onto a nonfunctionalized hyper-cross-linked resin: Purolite Macronet MN-200 [29-30]. The release process was carried out with comparing the release efficiency of three solutions (H_2SO_4, Na_2SO_4 and NaOH). The electrochemical oxidation of the three pollutants was performed on a $Ti/SnO_2–Sb_2O_5–IrO_2$ electrode and the kinetics of the electrochemical degradation of the three pollutants was examined. Our study demonstrates that the three pollutants can be efficiently adsorbed by MN-200 resin, released by a NaOH solution and degraded by $Ti/SnO_2–Sb_2O_5–IrO_2$ electrodes.

4.2 Experimental Section

4.2.1 Materials and chemicals

Phenol (99%, Anachemia), *p*-NPh (99%+, Aldrich) and *p*-cresol (99%, Aldrich) were used without any further purification. The Purolite Macronet MN-200 resin was kindly provided by Purolite Ltd. The resin was washed by pure water and dried in an oven at 60 °C before use. All other chemicals were of reagent grade and used as supplied. The ultrapure water (18.2MΩ cm) used to prepare all solutions was purified by a Nanopure Diamond® water system.

4.2.2 Characterization of the MN-200 resin

The properties of the nonfunctionalized Purolite Macronet MN-200 resin were evaluated by a nitrogen adsorption/desorption measurement with a NOVA 2200e surface area and pore size analyzer (Quantachrome). Nitrogen adsorption/desorption isotherms were obtained at 77.3K after degassing samples at 473K for 16 hours. Various adsorption models such as BET and Langmuir were applied to determine the surface and micropore area, showing that the surface

area of the resin is 790.7 m^2 g^{-1}; the t-Plot micropore area is 493.4 m^2 g^{-1}; the micropores (%) are

62.4% and the average pore diameter is 2.3 nm.

4.2.3 Adsorption of phenolic compounds

Equilibrium adsorption experiments were carried out by allowing a pre-selected amount of MN-

200 resin to reach equilibrium with phenol, p-NPh and p-cresol solutions of different initial

concentrations, C_0 (mmol L^{-1}), ranging from 1 to 6 mmol L^{-1} at a temperature of 293K. Known

weight of MN-200 resin (100mg) was introduced into 125 mL reaction bottles each containing

50 mL of the above solutions. The solutions were stirred constantly until the equilibrium was

reached. The equilibrium concentration, C_e (mmol L^{-1}), was determined and the equilibrium

adsorption capacity, q_e (mmol g^{-1}) was calculated [31]. Kinetic adsorption studies of phenol, p-

NPh and p-cresol were performed at the temperature of 293, 313 and 333 K respectively by

analyzing the adsorption capacity q_t (mmol g^{-1}) versus the initial concentration of 1 mmol L^{-1} at

different time intervals until the adsorption equilibrium was reached.

4.2.4 Pre-concentration and release of phenolic compounds

The pre-concentration experiments of phenol, p-NPh and p-cresol were carried out at 293 K. 160

mg of MN-200 resin was weighed and introduced to 200 mL of phenol, p-NPh and p-cresol

aqueous solutions with the initial concentration of 0.04 mmol L^{-1}. The solutions were stirred until

equilibrium was reached. After the pre-concentration process, the release experiments were

carried out by replacing the removed 200 mL equilibrium aliquots with 40 mL of 0.5 mol L^{-1}

NaOH solution. The solutions were stirred until the release process reached equilibrium. For

comparison, 0.5 mol L^{-1} Na$_2$SO$_4$ and H$_2$SO$_4$ solutions were also used to evaluate the release

efficiency of p-NPh.

4.2.5　Fabrication of the electrodes

The Ti/SnO$_2$–Sb$_2$O$_5$–IrO$_2$ electrodes used in this study were prepared by a thermal decomposition method [32-33]. The Ti substrates were cut into strips (12 cm×1.25 cm) and degreased in an ultrasonic bath of acetone for 10min followed by 10min in distilled water. The Ti substrate was etched in 18% HCl at 85 °C for 30 min. The coating solution made by mixing the SnO$_2$-Sb$_2$O$_5$ precursor dissolved in isopropanol and IrCl$_3$·3H$_2$O dissolved in ethanol. This was painted onto the pre-etched Ti substrates. After the solvents were evaporated in an air stream at 80 °C, the samples were calcinated at 450 °C for 10 min. This process was repeated until a SnO$_2$–Sb$_2$O$_5$–IrO$_2$ coating load of 25 g m^{-2} was reached. A final post-bake was carried out at 450 °C for 1 hour to complete the thermal oxidation process. After the Ti strips were coated completely, they were cut into smaller pieces (4.0 cm × 1.25 cm) and used for the surface analysis and electrochemical oxidation experiments.

4.2.6　Electrochemical oxidation study

An Arbin Instruments power supply controlled by a computer was used to apply and monitor the current and potential. The electrochemical oxidation of the released phenol, *p*-NPh and *p*-cresol was carried out in a 0.5 mol L^{-1} NaOH releasing reagent at the current density of 100 mA cm^{-2} and a temperature of 293K. The electrolytes were stirred constantly during the electrochemical oxidation of the phenol, *p*-NPh and *p*-cresol. The Ti/SnO$_2$–Sb$_2$O$_5$–IrO$_2$ electrode with a geometric surface area 5.0 cm^2 was used as the working electrode. The counter electrode was a Pt coil.

All the concentrations of phenol, *p*-NPh and *p*-cresol in aqueous solution were analyzed by a Cary 50 type UV-*vis* spectrophotometer at different time intervals. Three ten-point calibrations

were carried out in the range of (0.0 – 1.0), (0.0 − 0.1) and (0.0 – 1.0) mmol L^{-1} for phenol, *p*-NPh and *p*-cresol, respectively. Linear results were obtained with regression equations A_1=1.462C (mmol L^{-1}) + 0.022, A_2=10.104C (mmol L^{-1}) − 0.0094, and A_3 =1.638C (mmol L^{-1}) + 0.0063, all with a correlative coefficient R^2 > 0.999, for phenol, *p*-NPh and *p*-cresol, respectively.

4.3 Adsorption Studies

4.3.1 Adsorption equilibrium

Fig. 4.1 shows the adsorption isotherms of phenol, *p*-NPh and *p*-cresol on MN-200 resin in aqueous solution at 293K fitted using the Freundlich model. There are two common adsorption isotherms: Langmuir and Freundlich isotherms; they are widely used to describe adsorption process [6,34]. Langmuir isotherm which can be given as:

$$\frac{1}{q_e} = \frac{1}{q_m} + \frac{1}{q_m K_L C_e} \tag{1}$$

While Freundlich isotherm can be described as:

$$ln q_e = \frac{1}{n} ln C_e + ln K_F \tag{2}$$

Where C_e is the equilibrium concentrations (mmol L^{-1}), q_e is the equilibrium adsorption capacity (mmol g^{-1}), q_m is the maximum adsorption capacity (mmol g^{-1}), K_L is a Langmuir isotherm constant (L mmol^{-1}), K_F is the adsorption capacity ((mmol g^{-1}) (L mmol^{-1}) $^{(1/n)}$) in the Freundlich isotherm, and *n* refers to as the adsorption intensity in the Freundlich model.

As shown in Table 4.1, the experimental results can be characterized better by the Freundlich model due to the higher correlation coefficient. It has been reported that the adsorption capacity

of an adsorbent can be affected by several factors including its specific surface area, the pore size and pore structure, the solubility of the adsorbate and the hydrogen bonding, electrostatic interaction and π-π bond interaction between the adsorbate and adsorbent [30,35-37]. As can been seen from Fig. 4.1 and Table 4.1, the adsorption capacity of *p*-cresol and *p*-NPh is much larger than that of phenol. This difference in adsorbability can be explained in terms of the solubility of the three adsorbates. The solubility of *p*-cresol (1.9 g/100mL) and *p*-NPh (1.6 g/100mL) is much less than that of phenol (8.2g/100mL), thus *p*-cresol and *p*-NPh show less affinity towards water (higher hydrophobicity) and adsorb onto the resin more easily than phenol. This is also supported by the work of Valderrama et al [30] and Lin et al [36], who have reported that the hydrophobic interaction can be ruled out as a major influencing factor regulating the adsorption of organic compounds onto resin. Fig. 4.1 also indicates that the adsorption capacity of *p*-cresol is higher than that of *p*-NPh at high equilibrium concentrations although the solubility of *p*-cresol is slightly higher than that of *p*-NPh. This may result from the π-π interaction and electrostatic interaction between the adsorbate and the adsorbent [35-36]. The -CH$_3$ group and the -OH group of *p*-cresol are both electron-donating groups, whereas the -NO$_2$ group of *p*-NPh is an electron-withdrawing group. Hence the electron density of the aromatic ring of *p*-cresol is much higher than that of *p*-NPh, which can increase the π-donating strength of the host aromatic ring and thus enhance the π-π interactions between *p*-cresol and the MN-200 resin. In addition, the pK$_a$ of *p*-NPh (7.15) is much smaller than that of *p*-cresol (10.17), indicating that *p*-NPh dissociates more extensively than *p*-cresol. Therefore, more *p*-NPh anions are present in the solution than the corresponding anions of *p*-cresol, especially at the high concentrations. Higher anion concentration results in a greater degree of electrostatic repulsive forces. Consequently, the adsorption capacity of the resin for the *p*-NPh in solutions is expected
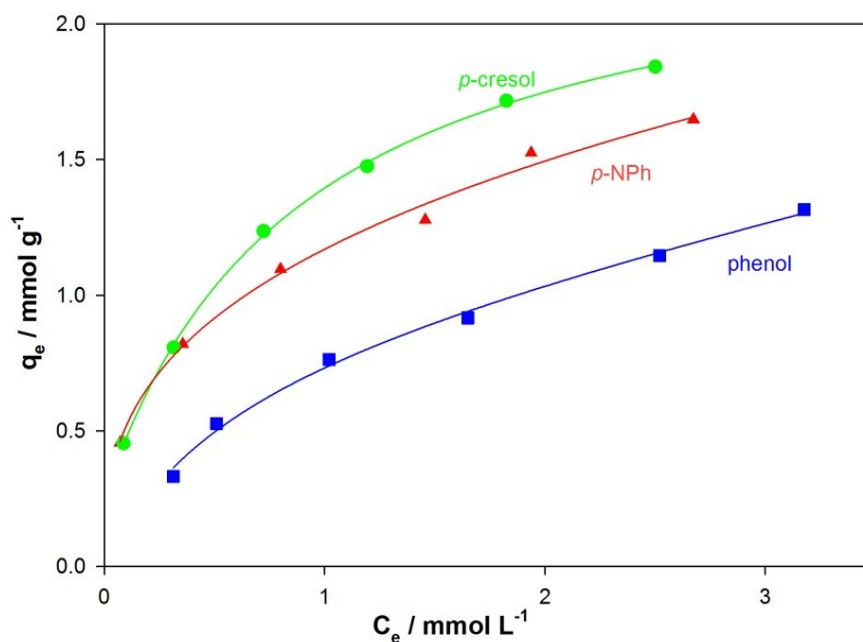
Fig. 4.1 The adsorption isotherms of phenol, *p*-NPh and *p*-cresol adsorbed onto MN-200 resin in aqueous solution at the temperature of 293K.

Table 4.1 The correlated parameters for the adsorption of phenol, *p*-NPh and *p*-cresol onto MN-200 resin at the temperature of 293K according to Langmuir and Freundlich isotherm.

| Adsorbate	Langmuir isotherm			Freundlich isotherm		
	q_m(mmol g^{-1})	K_L(L mmol^{-1})	R^2	K_F(mmol g^{-1})(L mmol^{-1})$^{(1/n)}$	1/n	R^2
Phenol	1.728	0.779	0.990	0.684	0.583	0.992
p-NPh	1.422	6.352	0.954	1.168	0.355	0.997
p-cresol	1.942	3.442	0.994	1.327	0.429	0.992

to be lower than that for *p*-cresol.

4.3.2 Adsorption kinetics

Adsorption kinetic studies were carried out to determine the uptake rate of phenol, *p*-NPh and *p*-cresol onto the MN-200 resin. As shown in Fig. 4.2A-C, the UV-Visible spectral absorbances of phenol, *p*-cresol and *p*-NPh centered at 269.9, 277.1 and 316.9 nm, respectively, decreased with time, indicating a decrease in concentrations of the three adsorbates in solutions. After a 5-hour period of adsorption, the removal efficiency of phenol, *p*-cresol and *p*-NPh was found to be 70%, 91% and 93%, respectively. The corresponding plot C_t/C_0 vs. time (Fig. 4.2D) shows that the concentration of the three adsorbates exhibited a sharp decrease within the first 1 hour, and then decreased slowly over time. This can be explained by the homogeneous particle-diffusion model and shell progress model developed by Valderrama *et al.* [4,30] as well as the intraparticle diffusion model developed by Weber and Morris [37]. The adsorption of the three adsorbates is first controlled by the macropore diffusion process in which the external resistance is significant and then is dominated by the micropore diffusion process, which has a much larger internal resistance.

Fig. 4.2E shows the plot of the three adsorbates uptake vs. time with the initial concentration of 1.0 mmol L^{-1} at 293K. It has been reported that the uptake kinetics might be described by either the pseudo-first-order or pseudo-second-order model [7,31]:

$$ln(q_e - q_t) = lnq_e - k_1t \qquad\qquad (3)$$

$$\frac{t}{q_t} = \frac{1}{k_2 q_e^2} + \frac{1}{q_e} \qquad\qquad (4)$$
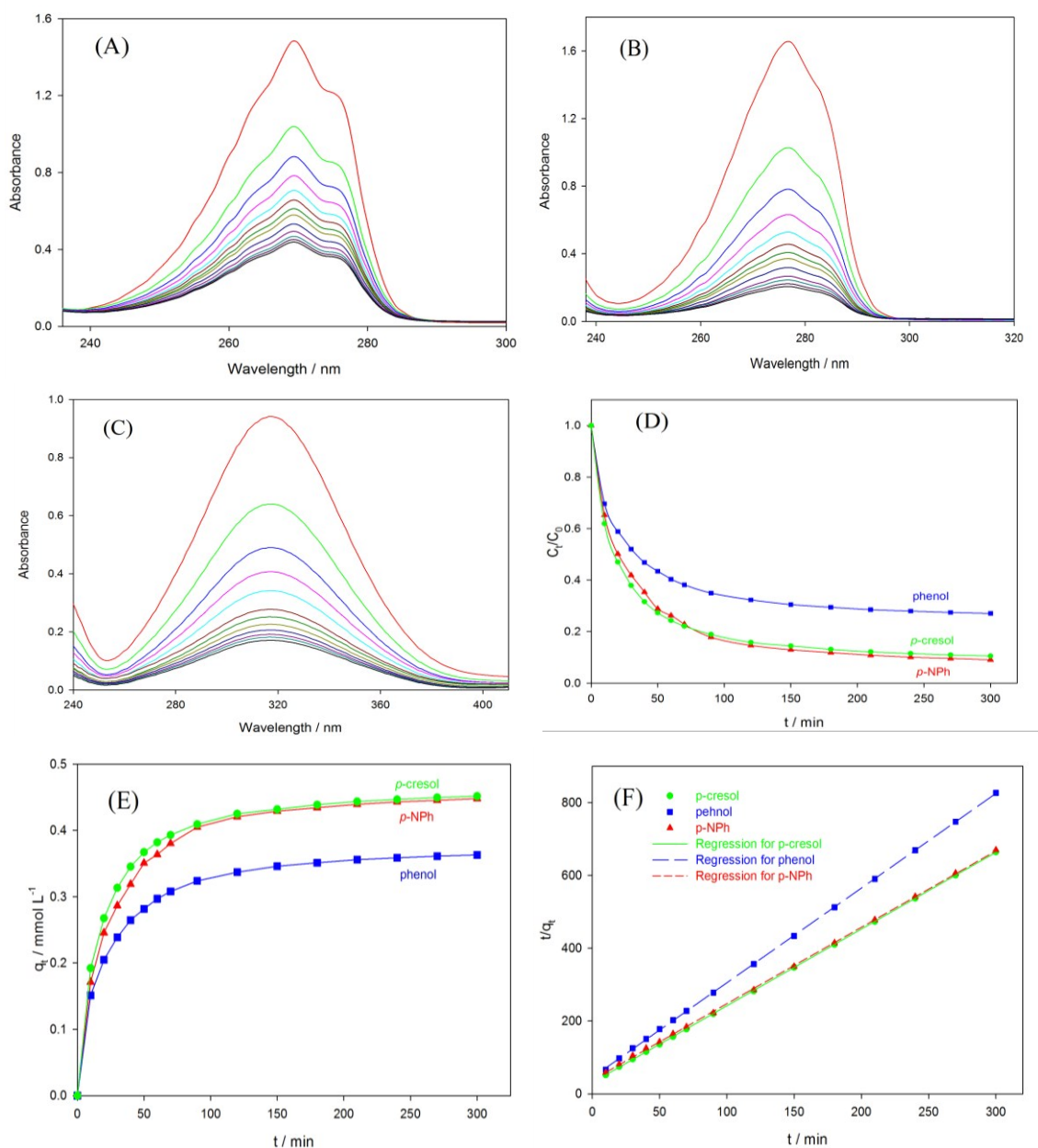
Fig. 4.2 UV spectra during the adsorption of: (A) phenol, (B) *p*-cresol and (C) *p*-NPh with an initial concentration of 1mmol L^{-1} onto MN-200 resin at the temperature of 293K; (D) Plot of C_t/C_0 vs. time; (E) The corresponding adsorption kinetic curve of phenol, *p*-NPh and *p*-cresol; and (F) Plot of t/q_t vs. time (pseudo-second-order kinetics) of phenol, *p*-NPh and *p*-cresol.

Where the q_t is the adsorption capacity at contact time t (mmol g^{-1}); k_1 (min^{-1}) and k_2 (g mmol^{-1} min^{-1}) are the pseudo-first-order and pseudo-second-order rate constants, respectively. The corresponding fitting curves of the three adsorbates for the pseudo-second-order kinetic model are shown in Fig. 4.2F and the kinetic parameters of the three adsorbates are listed in Table 4.2. The higher correlation coefficients ($R^2 > 0.99$) with the pseudo-second-order model and the calculated q_e values closer to the experimental ones suggest that the adsorption of the three adsorbates can be approximated more favourably by the pseudo-second-order model. The k_2 values of phenol, p-cresol, p-NPh at the temperature of 293 K were estimated based on the pseudo-second-order model to be 0.154, 0.142 and 0.118 g mmol^{-1} min^{-1}, respectively, indicating that the removal of phenol is more rapid than that of p-cresol and p-NPh. This may be attributed to the molecular size. The molecular size of phenol, p-cresol and p-NPh is 0.57nm × 0.43nm, 0.66nm × 0.43nm, and 0.66nm × 0.43nm, respectively, and the smaller molecular size of phenol facilitates its diffusion into the micropores of the adsorbent.

4.3.3 The effect of temperature on adsorption

In order to evaluate the effect of temperature, a series of contact time experiments were carried out with constant initial concentrations of phenol, p-cresol and p-NPh of 1 mmol L^{-1} and MN-200 resin dosage of 100 mg/50 mL at 293, 313, and 333 K. The effect of temperature on the adsorption of phenol is shown in Fig. 4.3A and the kinetic parameters for the pseudo-first-order and pseudo-second-order model of the three adsorbates at different temperatures are listed in Table 4.2. It can be seen from Fig. 4.3A and Table 4.2 that the uptake of the phenol onto MN-200 resin decreased from 0.363 to 0.263 mmol^{-1} g^{-1} with an increase in temperature from 293 to 333K, indicating the exothermic nature of adsorption [5,12]. The pseudo-second-order rate constants k_2 of phenol can be determined by the slope of the plot of $q_t/(q^2_e - q_e q_t)$ vs. time shown in

Fig. 4.3B. Both the increase in the adsorption rate constant k_2 value from 0.154 to 0.668 g mmol^{-1} min^{-1} (Table 4.2) and the decrease in adsorption equilibrium time from 180 to 90 min (Fig. 4.3A) indicate that enhanced adsorption velocity of phenol resulted from an increase in temperature. Similar behaviours were obtained with *p*-cresol and *p*-NPh, and the results are listed in Table 4.2. This temperature effect can be explained in terms of the mobility of the adsorbates and extensive existence of hydrogen bonding between the adsorbates' molecules and water. The increased temperature not only expedites the diffusion of the adsorbates to the adsorbent but also helps to break the hydrogen bonding.

Table 4.2 The correlative parameters for the adsorption kinetics of phenol, *p*-NPh and *p*-cresol absorbed onto MN-200 resin at different temperatures.

Absorbate	Temperature	Pseudo-first-order		Pseudo-second-order			
		k_1(min^{-1})	R^2	k_2(g mmol^{-1} min^{-1})	R^2	q_e(mmol g^{-1})	
						Exp.	Cal.
	293k	0.0267	0.965	0.154	0.999	0.363	0.382
Phenol	313k	0.0390	0.964	0.301	0.998	0.318	0.335
	333k	0.0652	0.991	0.668	0.998	0.263	0.278
	293k	0.0265	0.973	0.118	0.999	0.453	0.475
p-NPh	313k	0.0421	0.967	0.265	0.999	0.438	0.456
	333k	0.0510	0.954	0.425	0.999	0.413	0.430
	293k	0.0300	0.969	0.142	1.000	0.451	0.474
p-cresol	313k	0.0387	0.950	0.260	0.999	0.435	0.454
	333k	0.0569	0.985	0.379	0.999	0.407	0.427
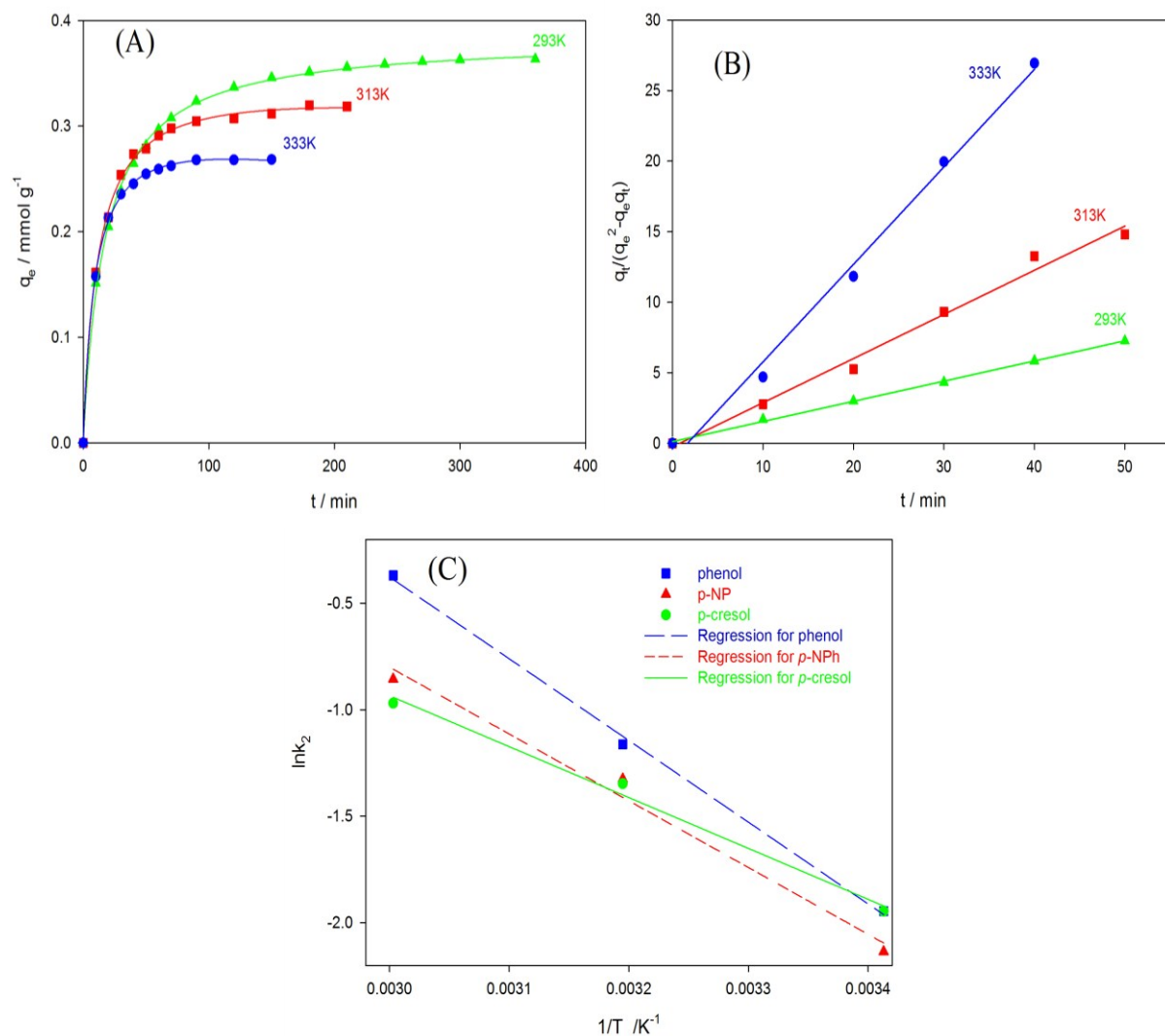
Fig. 4.3 (A) The adsorption kinetic curve of phenol with the initial concentration of 1mmol L^{-1} at 293, 313 and 333K. (B) Plot of $q_t/(q^2_e-q_eq_t)$ vs. time for the adsorption of phenol onto MN-200 resin in aqueous solution at different temperatures with the initial concentration of 1mmol L^{-1} and the slope utilized in the determination of the pseudo-second-order kinetic rate constant k_2. (C) Plot of lnk_2 vs. 1/T (Arrhenius relationship) for the adsorption of *p*-NPh, *p*-cresol and phenol with the initial concentration of 1mmol L^{-1} onto MN-200 resin in aqueous solution with a slope utilized to determine the activation energy.

The activation energy of adsorption was calculated based on the Arrhenius equation [38-39]:

$$k_2 = Ae^{-\frac{E_a}{RT}} \qquad\qquad (5)$$

And the linear form of Eq. 5 can be given as:

$$lnk_2 = -\frac{E_a}{RT} + lnA \qquad\qquad (6)$$

where k_2 is the pseudo-second-order rate constant (g mmol^{-1} min^{-1}), A is the Arrhenius constant related to temperature (g mmol^{-1} min^{-1}), R is the gas constant (8.314 J mol^{-1} K^{-1}), T is the temperature in Kelvin and E_a is the activation energy in kJ mol^{-1}. The value of E_a can be determined from the slope of lnk_2 vs. 1/T plot (Fig. 4.3C). The activation energy for the adsorption of phenol, p-NPh and p-cresol onto MN-200 resin was estimated to be 29.60, 26.07 and 19.87 kJ mol^{-1}, respectively. It was reported by Lv et al [38] and Ho et al [40] that the activation energy of adsorption for diffusion-controlled processes is less than 25-30 kJ mol^{-1}. The E_a values of the three adsorbates indicate that the adsorption process is diffusion-controlled, as already discussed in the above section of Adsorption Kinetics. In addition, the values of activation energy and subsequent impediment of the adsorption process decrease in the order of phenol > p-NPh > p-cresol, which is in agreement with the results of adsorption capacity, as shown in Fig. 4.1

4.4 Adsorption and Release

It has been reported that electrochemical oxidation of the pollutants with low concentration in solution usually leads to a slow mass transfer of the pollutants towards the anodic surface, and thus results in a slow rate of oxidation and a low current efficiency [24,27]. Another challenge of

the electrochemical oxidation process is its high power consumption caused by the poor conductivity of wastewater [28,41]. In order to achieve a high performance of electrochemical oxidation, phenol, p-NPh and p-cresol were first preconcentrated by the adsorption process described above. The adsorption was carried out by adsorbing the three pollutants with an initial concentration of 0.04 mmol L^{-1} from the 200 mL of aqueous solution onto 0.16 g of the MN-200 resin. It was found that the removal efficiency of the three pollutants in the adsorption process was close to 100%.

To re-generate the resin and to further treat the adsorbed phenolic pollutants, we have studied the effect of electrolytes on the release of the phenolic pollutants from the resin. Fig. 4.4 compares the release efficiency of 40 mL of three different solutions (H_2SO_4, Na_2SO_4 and NaOH) with the concentration of 0.5 mol L^{-1} for the release of the adsorbed p-NPh from the resin. Clearly, the electrolytes H_2SO_4 and Na_2SO_4 are unable to release the adsorbed p-NPh. In contrast, a large broad peak appeared when NaOH was used as the release agent. Similar results were obtained for the release of the adsorbed p-cresol and phenol. Further quantitative analysis of the UV visible spectra shows that the release efficiency of the NaOH solution for the adsorbed p-NPh, p-cresol and phenol was over 90%. Our recent studies have shown that a NaOH electrolyte provides a desirable medium for the electrochemical oxidation of organic compounds [42-43]. The effective release of the adsorbed phenolic pollutants using a NaOH solution opens the door to the further treatment the pollutants using the advanced electrochemical oxidation approach.
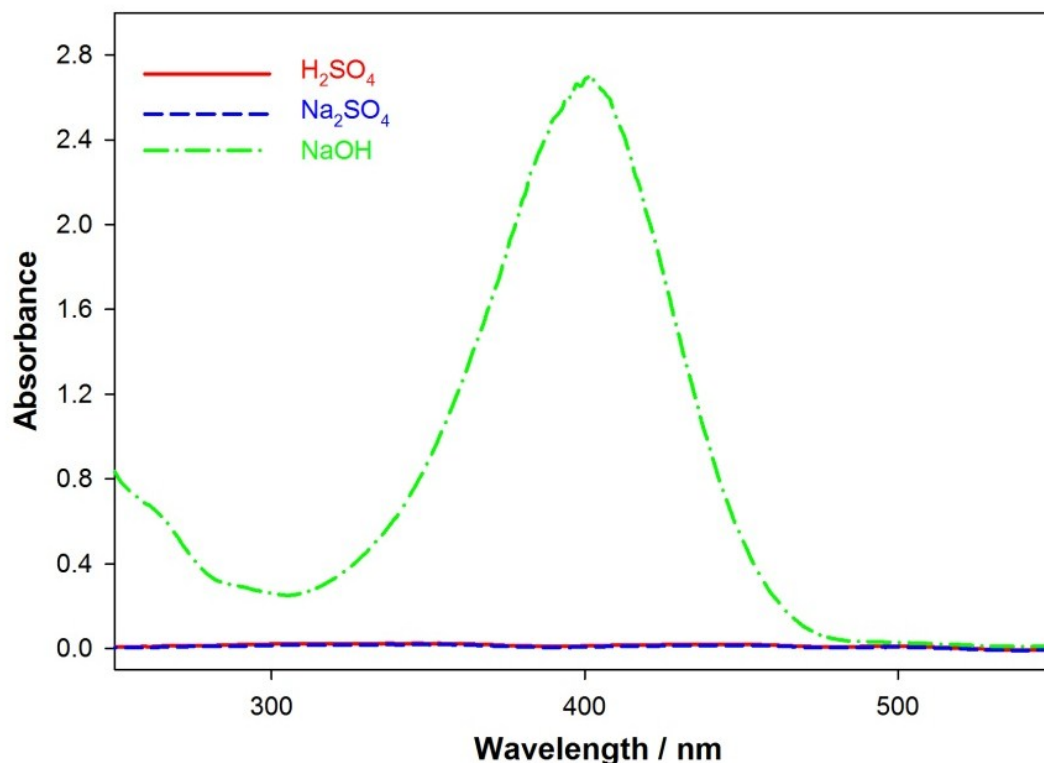
Fig. 4.4 UV-Visible spectra of the release of the adsorbed p-NPh with different solutions: 0.5 mol L^{-1} NaOH, Na$_2$SO$_4$ and H$_2$SO$_4$.

4.5 Electrochemical Oxidation

Among various metal oxide electrodes (e.g., PbO$_2$, RuO$_2$, IrO$_2$ and SnO$_2$), Sb-doped SnO$_2$ electrodes are thought to be superior for the oxidation of organic compounds [44-45]. In addition, SnO$_2$ possesses the additional advantage of being inexpensive compared to many other precious metal oxides, Pt and BBD electrodes. The main issue with the Ti/SnO$_2$–Sb$_2$O$_5$ electrode is its short lifetime; however, this can overcome by the addition of IrO$_2$. A small amount IrO$_2$ is able to avoid the formation of the outer passive layer and thus significantly increase the service life of the anode [14]. Thus, the Ti/SnO$_2$–Sb$_2$O$_5$–IrO$_2$ electrodes were fabricated and used as the working electrode in the electrochemical oxidation of the released phenolic pollutants.

Fig. 4.5 shows the micro-structure and composition of the oxide coating characterized by JEOL 5900LV scanning electron microscopy and X-ray energy dispersive spectrometry (SEM/EDS). The SEM image of the Ti/SnO$_2$–Sb$_2$O$_5$–IrO$_2$ electrode (Fig. 4.5A) displays that the SnO$_2$–Sb$_2$O$_5$–IrO$_2$ coating prepared using the thermal decomposition method exhibits a porous 'cracked mud' structure, which is typical for oxide electrodes [46]. The EDS spectrum of the Ti/SnO$_2$-Sb$_2$O$_5$-IrO$_2$ (Fig. 4.5B) shows peaks for oxygen, iridium, tin, and antimony. Further quantitative analysis revealed that the coating contained about 10% IrO$_2$, which is consistent with the prepared precursor solutions used in the fabrication process.
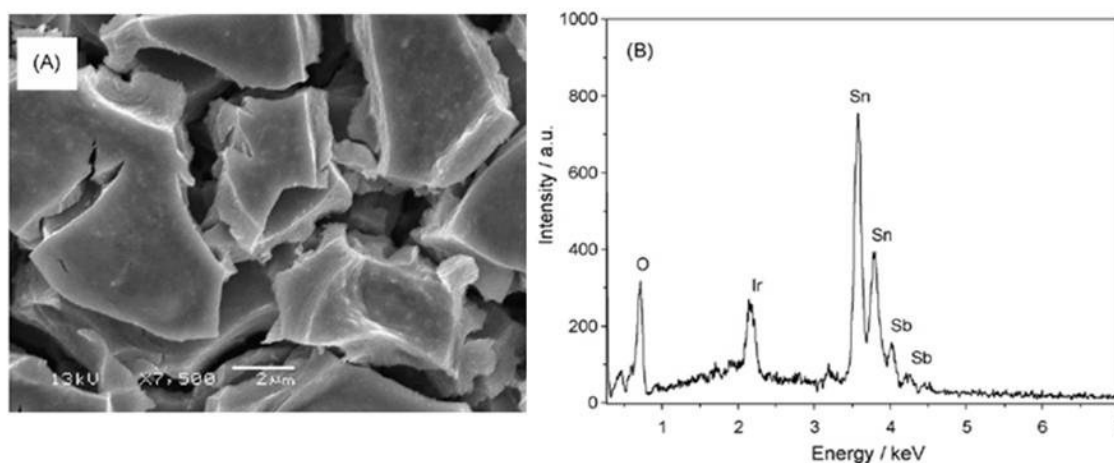

Fig. 4.5 SEM image (A) and EDS (B) of the as-prepared Ti/SnO$_2$-Sb$_2$O$_5$-IrO$_2$ electrode.

Fig. 4.6A-C presents typical scanning kinetics graphs taken at different time intervals during the electrochemical oxidation of p-NPh, phenol and p-cresol, respectively, at the current density of 100 mA cm^{-2} and the temperature of 293 K. As can be seen from Fig. 4.6A, the main absorption band centered at 400 nm significantly decreased with time. In addition, a new band appeared at ca. 320 nm, indicating that intermediates were formed during the electrochemical oxidation of p-NPh. After rising to its maximum intensity, the new band began to decrease and finally disappeared, demonstrating that the intermediates can also be completely electrochemically oxidized. Similarly, for the UV spectra of phenol (Fig. 4.6B), the peak at 240 nm decreased significantly during the electrochemical oxidation while the peak at ca. 260nm and one new peak entered at ca. 320 nm increased during the first 60 min, and then decreased over time. After 420 min electrochemical oxidation, all the peaks disappeared, indicating that the phenol and the intermediates were completed eliminated. Fig. 4.6C presents the spectral absorbance for the oxidation of p-cresol. Both absorbance bands (240nm and 295 nm) decreased with time, indicating a decrease in concentration. The peak centered at ca 270 nm first increased and then decreased over time, showing the short-time formation and complete destruction of the intermediates during the oxidation process.

The C/C_0 vs. time relationship for the three pollutants is calculated based on the calibration equation between the absorbance versus concentration carried out in 0.5 mol L^{-1} NaOH solution. As shown in Fig. 4.6D, 83%, 90% and 96% of the initial p-cresol, phenol and p-NPh were oxidized, after 450, 420 and 110 min periods of treatment, respectively. The stimulated curves based on first-order kinetics fit very well with the experimental data. The plots of $\ln(C/C_0)$ vs. time shown in the inset of Fig. 4.6D further support the first-order kinetics relationship with correlation coefficients of 0.997, 0.999 and 0.999, and give rate constants of $k = 0.0068$, 0.0110
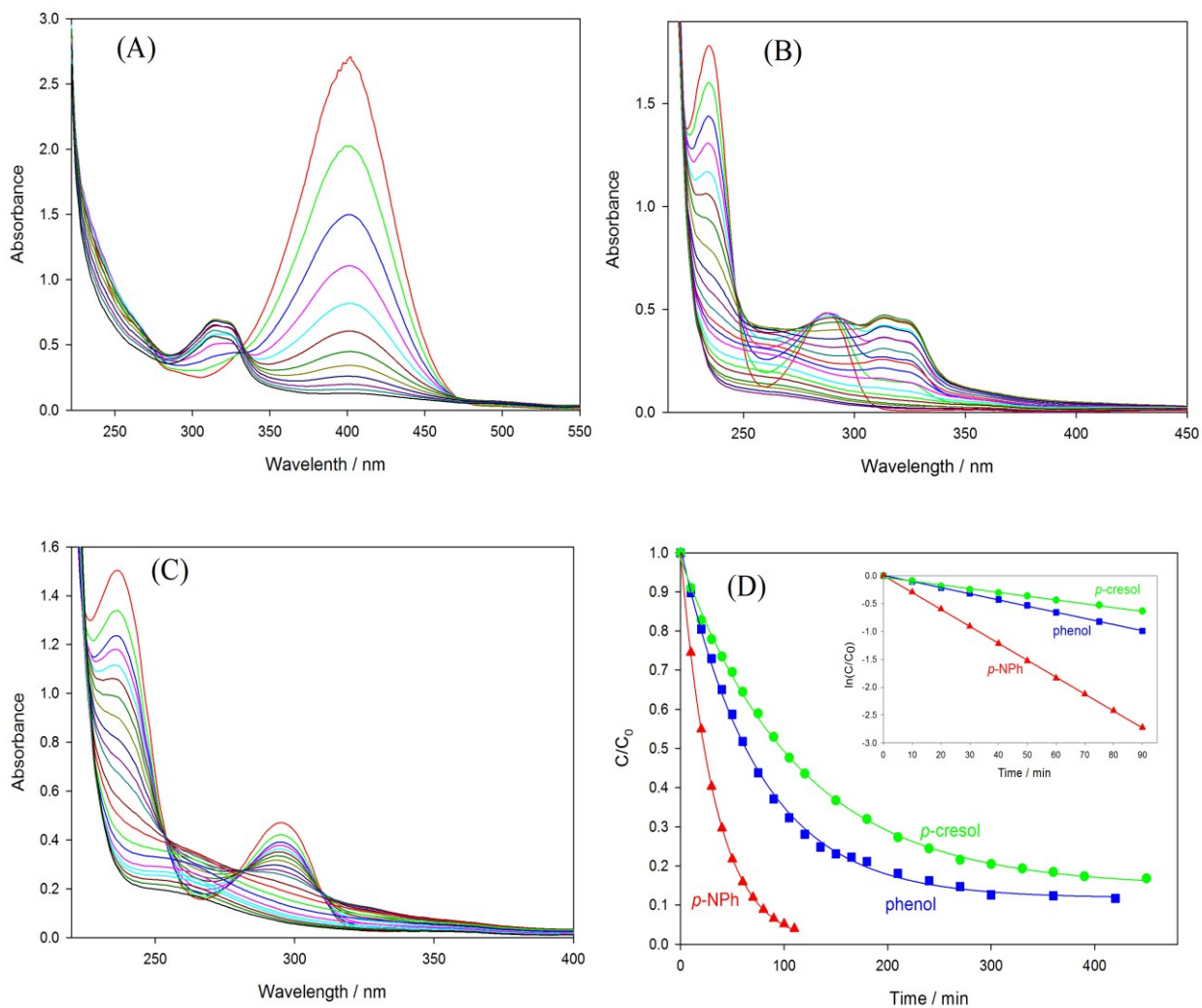
Fig. 4.6 (A-C) UV spectra of the electrochemical oxidation of *p*-NPh, phenol and *p*-cresol at a Ti/ SnO$_2$-Sb$_2$O$_5$-IrO$_2$ electrode in 0.5 mol L-1 NaOH at 293K with 100 mA cm^{-2}. (D) Plot of C/C0 vs. time for the electrochemical oxidation of phenol, *p*-NPh and *p*-cresol at a Ti/SnO$_2$-Sb$_2$O$_5$-IrO$_2$ electrode in 0.5 mol L^{-1} NaOH at 293K with 100 mA cm^{-2}. The inset shows the ln(C/C$_0$) vs. time relationship.

and 0.0304 min^{-1} for *p*-cresol, phenol and *p*-NPh, respectively. The rate constant for the electrochemical oxidation of *p*-NPh is much larger than that for the electrochemical oxidation of *p*-cresol and phenol. It has been reported that the electrochemical degradation of organics is primarily dependent on the hydroxyl radical generated on the anode [13,47]. Under the attack of hydroxyl radicals, the release of *p*-substituted groups [3,47] from the aromatic ring is the rate-limiting step. Since electron-withdrawing groups are easily released, the *p*-substituted phenols with these groups are degraded faster than those with electron-donating groups [1]. In addition, the electron-donating groups increase the electron density of the aromatic ring, thus enhancing its stability and, consequently, strongly retarding the oxidation process [48]. As for the three chemicals in this study, the -NO$_2$ group in *p*-NPh is electron-withdrawing while the -CH$_3$ group in *p*-cresol is electron-donating, thus the rate constant for the electrochemical oxidation is shown as *p*-NPh> phenol> *p*-cresol.

4.6 Summary

To address the non-degradability nature of adsorption and the poor performance of electrochemical treatment of wastewater with low concentrations of pollutants, we have demonstrated a novel approach by integration of effective adsorption, release and electrochemical oxidation in this study. The adsorption process was carried out by adsorbing three model phenolic compounds (phenol, *p*-NPh and *p*-cresol) onto MN-200 resin and shows high removal efficiency of the three model pollutants. The adsorption isotherms can be effectively fitted using the Freundlich isotherm model. The adsorption kinetics of the three pollutants obeys the pseudo-second-order model and an increase in temperature expedites the adsorption process whereas it lowers adsorption capacity. Our experimental results have shown that the adsorbed phenolic pollutants onto the MN-200 resin can be efficiently released by NaOH

media with a significantly reduced volume, thus greatly increasing the concentration of the pollutants as well as the conductivity of the electrolyte. The effective release of the adsorbed phenolic pollutants using a NaOH solution opens the door to completely treat the pollutants using the advanced electrochemical oxidation. We further studied the electrochemical oxidation of the released phenolic pollutants on Ti/SnO_2–Sb_2O_5–IrO_2 electrodes, showing that the three pollutants can be degraded efficiently and the kinetics of the electrochemical oxidation of the three pollutants is pseudo-first-order. In summary, our study has shown that the effective adsorption-release process can enhance the electrochemical oxidation of the pollutants and the combined process is very promising for the treatment of phenolic pollutants in wastewater.

References

[1]   X. Zhu, S. Shi, J. Wei, F. Lv, H. Zhao, J. Kong, Q. He, J. Ni, *Environ. Sci. Technol.* **2007**, *41*, 6541.

[2]   R. A. Torres, W. Torres, P. Peringer, C. Pulgarin, *Chemosphere* **2003**, *50*, 97.

[3]   P. Canizares, J. Lobato, R. Paz, M. A. Rodrigo, C. Saez, *Water Res.* **2005**, *39*, 2687.

[4]   M. Caetano, C. Valderrama, A. Farran, J. L. Cortina, *J. Colloid Interface Sci.* **2009**, *338*, 402.

[5]   J. H. Huang, *J. Hazard. Mater.* **2009**, *168*, 1028.

[6]   V. K. Gupta, I. Ali, V. K. Saini, *Environ. Sci. Technol.* **2004**, *38*, 4012.

[7]   A. S. Bilgili, *J. Hazard. Mater.* **2006**, *137*, 157.

[8]   S. H. Lin, R. S. Juang, *J. Environ. Manage.* **2009**, *90*, 1336.

[9]   R. S. Juang, W. C. Huang, Y. H. Hsu, *J. Hazard. Mater.* **2009**, *164*, 46.

[10]   N. C. Pradhan, C. S. Sarkar, S. Niyogi, B. Adhikari, *J. Appl. Polym. Sci.* **2002**, *83*, 822.

[11]   K. Juttner, U. Galla, H. Schmieder, *Electrochim. Acta* **2000**, *45*, 2575.

[12]   B. Pan, W. Du, W. Zhang, X. Zhang, Q. Zhang, B. Pan, L. Lv, Q. Zhang, J. Chen, *Environ. Sci. Technol.* **2007**, *41*, 5057.

[13]   X. Zhu, M. Tong, S. Shi, H. Zhao, J. Ni, *Environ. Sci. Technol.* **2008**, *42*, 4914.

[14]   B. Adams, M. Tian, A. Chen, *Electrochim. Acta* **2009**, *54*, 1491.

[15]   R. M. Asmussen, M. Tian, A. C. Chen, *Environ. Sci. Technol.* **2009**, *43*, 5100.

[16]   J. Huang, K. Huang, S. Liu, Q. Luo, M. Xu, *J. Colloid Interface Sci.* **2007**, *315*, 407.

[17]   A. M. Li, Q. X. Zhang, J. L. Chen, Z. G. Fei, L. Chao, W. X. Li, *React. Funct. Polym.* **2001**, *49*, 225.

[18]   A. M. Li, Q. X. Zhang, G. C. Zhang, J. L. Chen, Z. H. Fei, F. Q. Liu, *Chemosphere* **2002**, *47*, 981.

[19]   B. J. Pan, B. C. Pan, W. M. Zhang, Q. R. Zhang, Q. X. Zhang, S. R. Zheng, *J. Hazard. Mater.* **2008**, *157*, 293.

[20]   J. Huang, C. Yan, K. Huang, *J. Colloid Interface Sci.* **2009**, *332*, 60.

[21]   J. Yang, J. Wang, J. P. Jia, *Environ. Sci. Technol.* **2009**, *43*, 3796.

[22]   J. W. Wang, D. Bejan, N. J. Bunce, *Ind. Eng. Chem. Res.* **2005**, *44*, 3384.

[23]   J. D. Rodgers, N. J. Bunce, *Environ. Sci. Technol.* **2000**, *35*, 406.

[24]   M. Tian, L. Bakovic, A. C. Chen, *Electrochim. Acta* **2007**, *52*, 6517.

[25]   M. Li, C. Feng, W. Hu, Z. Zhang, N. Sugiura, *J. Hazard. Mater.* **2009**, *162*, 455.

[26]   Y. Q. Wang, B. Gu, W. L. Xu, *J. Hazard. Mater.* **2009**, *162*, 1159.

[27]   A. M. Polcaro, S. Palmas, *Ind. Eng. Chem. Res.* **1997**, *36*, 1791.

[28]   L. Lei, Q. Dai, *Ind. Eng. Chem. Res.* **2007**, *46*, 8951.

[29]   C. Valderrama, J. L. Cortina, A. Farran, X. Gamisans, F. X. de las Heras, *React. Funct. Polym.* **2008**, *68*, 679.

[30] C. Valderrama, X. Gamisans, F. X. de las Heras, J. L. Cortina, A. Farrán, *React. Funct. Polym.* **2007**, *67*, 1515.

[31] C. Long, J. D. Lu, A. M. Li, D. B. Hu, F. Q. Liu, Q. X. Zhang, *J. Hazard. Mater.* **2008**, *150*, 656.

[32] A. C. Chen, B. Miller, *J. Phys. Chem. B* **2004**, *108*, 2245.

[33] B. Miller, A. C. Chen, *Electrochim. Acta* **2005**, *50*, 2203.

[34] H. Genc-Fuhrman, J. C. Tjell, D. McConchie, *Environ. Sci. Technol.* **2004**, *38*, 2428.

[35] S. Nouri, F. Haghseresht, G. Q. M. Lu, *Adsorpt.-J. Int. Adsorpt. Soc.* **2002**, *8*, 215.

[36] D. Lin, B. Xing, *Environ. Sci. Technol.* **2008**, *42*, 7254.

[37] W. J. Weber , J. C. Morris, Proceedings of 1st International Conference on Water Pollution Symposium, vol. 2, Pergamon Press, Oxford 1962

[38] L. Lv, J. He, M. Wei, X. Duan, *Ind. Eng. Chem. Res.* **2006**, *45*, 8623.

[39] K. V. Kumar, *Ind. Eng. Chem. Res.* **2009**, *48*, 5105.

[40] Y. S. Ho, G. McKay, *Chem. Eng. J.* **1998**, *70*, 115.

[41] K. Vijayaraghavan, D. Ahmad, R. Lesa, *Ind. Eng. Chem. Res.* **2006**, *45*, 6854.

[42] N. Matyasovszky, M. Tian, A. C. Chen, *J. Phys. Chem. A* **2009**, *113*, 9348.

[43] R. Tolba, M. Tian, J. Wen, Z.-H. Jiang, A. Chen, *J. Electroanal. Chem.* **2010**, *649*, 9.

[44] R. Kotz, S. Stucki, B. Carcer, *J. Appl. Electrochem.* **1991**, *21*, 14.

[45] B. Correa-Lozano, C. Comninellis, A. D. Battisti, *J. Appl. Electrochem.* **1997**, *27*, 970.

[46] A. C. Chen, S. Nigro, *J. Phys. Chem. B* **2003**, *107*, 13341.

[47] M. Zhou, Q. Dai, L. Lei, C. a. Ma, D. Wang, *Environ. Sci. Technol.* **2004**, *39*, 363.

[48] W. Partenheimer, *Adv. Synth. Catal.* **2009**, *351*, 456.

Chapter 5. Combined TSAMBR and Electrochemical Oxidation (TSAMBR – EO) for the Treatment of Thermomechanical Pulping Pressate and the Membrane Fouling in the TSAMBR at Different Hydraulic Retention Times

5.1 Introduction

The pulp and paper industry is undergoing significant reforms in its processes and environmental practices in order to respond to more competitive markets and meet more stringent environmental regulations. The industry is now seeking promising technologies to conserve and reuse water with the aim for system closure. One appealing option is to reuse the wastewaters after effective in-mill treatment. Considering that most of the waste streams in pulp and paper industry, for instance, thermomechanical pulping pressate, which is produced by crushing or grinding of the wood chips in the thermomechanical pulping process, are high strength and high temperature in nature [1], thermophilic aerobic biological process (TABP) is the most favourable treatment technology for them [2].

The TABP can harness the energy content (i.e. rich in organic matters and/or high temperature) in the wastewaters to facilitate the autothermal operation without the exogenous heat input and thus eliminates the requirements of the pre-cooling for conventional biological treatment and the post-heating for subsequent reuse of the treated effluent [2-3]. In addition, compared to analogous mesophilic treatment, thermophilic treatment has the advantages of low sludge yield, high reaction rate, and excellent process stability [2]. However, it is believed that the elevated operating temperature in the TABP usually leads to the deterioration of the sludge settleability

and thus raises the problem of biomass separation [4-5]. The incorporation of membrane separation technology into the TABP to construct unique thermophilic submerged aerobic membrane bioreactors (TSAMBRs) may overcome this problem [6].

The TSAMBRs have been successfully used for the treatment of wastewaters from pulp and paper industry, food industry and landfill sites [7-10]. All the findings demonstrate that TSAMBR can achieve high effluent quality, low sludge yield and good process stability. However, similar to the mesophilic MBRs systems, the membrane fouling is also the intractable problem associated with the TSAMBRs and a careful review of the literature shows that there is quite limited information available for the membrane fouling in TSAMBRs.

Hydraulic retention time (HRT) is a very important operating parameter for MBRs system, which correlates not only to the treatment efficiency of the MBRs [11], but also to the sludge properties in the MBRs [12-14]. For example, Ren et al. [11] reported on using a mesophilic aerobic MBR for the treatment of domestic sewage and found that with the decrease in HRT, the COD removal efficiency decreased. Moreover, Meng et al. [13] found that MLSS concentration, EPS concentration and sludge viscosity increased significantly as HRT decreased in a mesophilic aerobic MBR. However, to date, no investigation has been reported on the influence of HRT on the TSAMBR system.

In order to practically achieve system closure, further treatment of the effluent after the TSAMBR system is required. Several approaches including reverse osmosis (RO) [15], ozonation [16-17] and electrochemical oxidation [18] have been proposed for post treatment of MBRs effluent. Among them, electrochemical oxidation has the advantages of versatility, easy operation, amenability to automation and most importantly, environmentally benign [19]. Using

electrochemical oxidation as a post treatment process has also been reported on treating different wastewaters [20-22], indicating the high feasibility of the process. Therefore, electrochemical oxidation was selected as a post treatment method after the TSAMBR system to form a unique TSAMBR – EO process in this study.

The objectives of this study are to: (i) test the feasibility of using a TSAMBR followed by electrochemical oxidation (TSAMBR – EO) for the in-mill treatment of thermomechanical pulping pressate and investigate the effect of HRT on the performance, sludge properties and membrane fouling in the TSAMBR.

5.2   Experimental Section

5.2.1   Experimental set-up and operation

A lab-scale TSAMBR system was built for the treatment of thermomechanical pulping pressate from a local pulp and paper mill (Fig. 5.1). The TSAMBR has a working volume of 6.0 L, in which a flat sheet microfiltration membrane module ($0.015 \text{ m}^2 \times 2 = 0.03 \text{ m}^2$) was immersed. The membranes (SINAP Membrane Science & Technology Co. Ltd., Shanghai, China) were made of polyvinylidene fluoride (PVDF) materials with a pore size of 0.3 μm and a molecular weight cut off (MWCO) of 70,000 Da. In order to maintain satisfying dissolved oxygen level, fine bubbles and coarse bubbles were both used in the aeration system in the TSAMBR. Fine bubbles were produced by two air stones at the bottom of the reactor connected to two air pumps (1.6 LPM). Coarse bubbles were provided by pumping air at the rate of 3.2 LPM through two stainless steel tubes diffuser (one for each side of the module) located at the bottom of the membrane module. In addition to aeration, the coarse bubbles also help mix biomass and mitigate membrane fouling by constant scouring of the membrane surface. A pH regulation

pump (Thermo/Barnant, Model HD-pH-5e10, Barrington, IL, USA) and a pH electrode (Thermo Scientific, Beverly, MA, USA) were installed for the automatic control of the pH value at 6.9 ± 0.1 using 0.2 M NaOH solution. The TSAMBR was operated at a thermophilic temperature of 51±1 °C by circulating hot water (63 °C) through the water jacket. The thermophilic sludge in this study was developed by a step increase in temperature using a seed sludge obtained from the wastewater treatment unit of a local pulp and paper mill. The sludge liquor was continuously mixed by a magnetic stirrer located at the bottom of bioreactor.
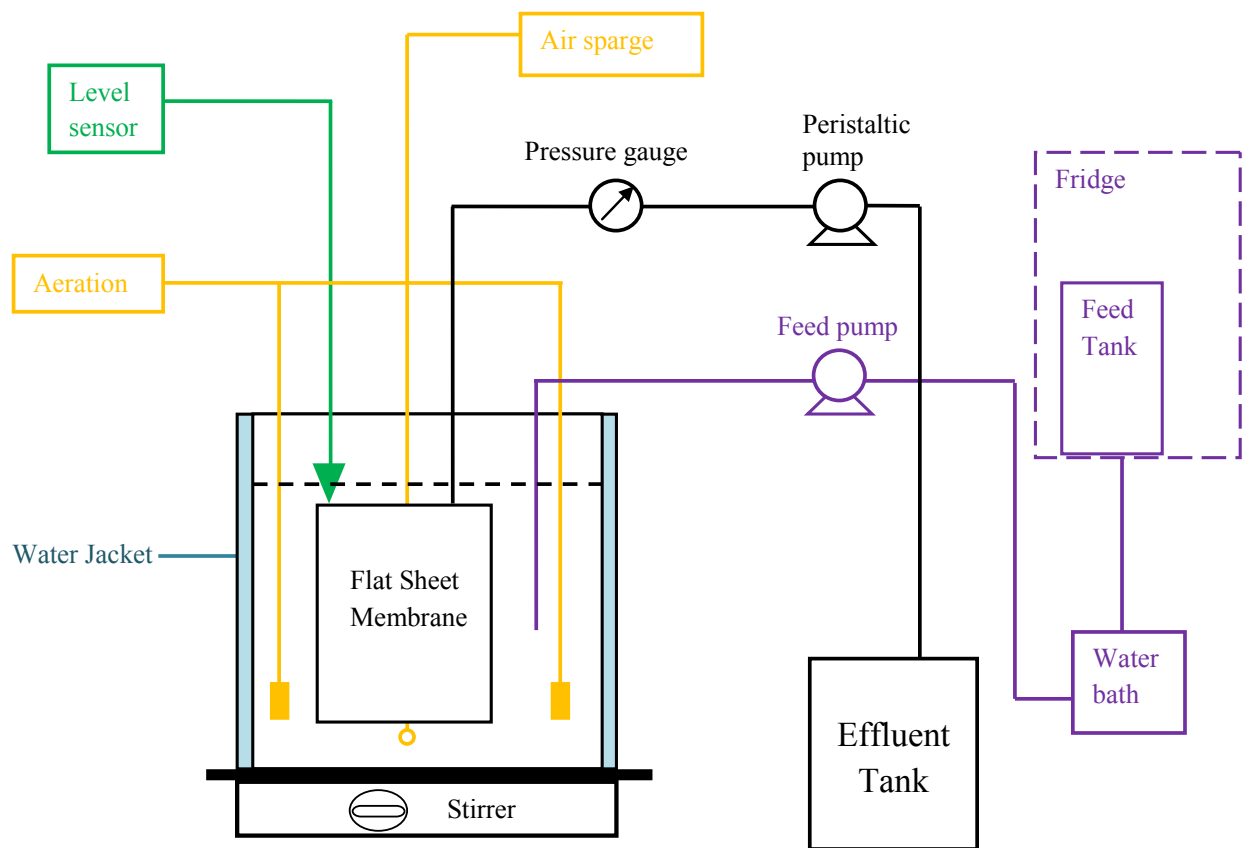

Fig. 5.1 Schematic of the thermophilic submerged aerobic membrane bioreactor set-up.

TMP pressate was pumped into the bottom of the bioreactor automatically by a peristaltic pump (Masterflex Model 7520-50, Barnant Co., USA) controlled by a level sensor (Madison Co., USA) and controller (Flowline, USA). The characteristics of the influent are summarized in Table 5.1. Macro-nutrients: nitrogen (NH_4Cl) and phosphorus (KH_2PO_4) were fed in a proportion of COD: N: P = 100:5:1 for biomass growth in an aerobic environment. The permeate was obtained intermittently by using a peristaltic pump (Masterflex, C/L, Model 77120-70, Barnant Co., USA) with a operation mode of 4 min on and 1 min off. Membrane flux was controlled by adjusting the pump rotation speed and transmembrane pressure (TMP) was measured by a vacuum gauge connected between the bioreactor and the permeate pump. During the operation of the bioreactor, a total volume of 300 ml of sludge was taken out for bulk sludge characterization or was wasted daily to main the SRT = 20 d. The main operating conditions are summarized in Table 5.2. When the TMP reached 30 Kpa, the reactor was shut down and the membrane module was taken out of the bioreactor and replaced by a new one. The fouled membranes were then used for cake sludge characterization.

The electrochemical oxidation of the TSAMBR effluent was performed on the lab-made $Ti/SnO_2-Sb_2O_5-IrO_2$ electrode with an applied current of 80 mA for 5.5 hours. The fabrication and characterization of the $Ti/SnO_2-Sb_2O_5-IrO_2$ electrode were elucidated in Chapter 4. 20ml of the TSAMBR effluent was put into a two-electrode cell where the $Ti/SnO_2-Sb_2O_5-IrO_2$ electrode with a geometric area of 5 cm^2 acted as the working electrode and a platinum coil served as the counter electrode. The electrochemical cell was connected to an Arbin Instruments power supply coupled with a computer system for the application and monitoring of current and potential. A Fisher stirrer was used to stir the solution during the electrochemical oxidation of the TSAMBR treated effluent.

Table 5.1 Main characteristics of thermomechanical pulping pressate.

pH	4.0 - 4.2
TSS (mg/L)	~330
COD (mg/L)	3343 - 4250
Total nitrogen (mg/L)	0.01 - 0.02
Total phosphorus (mg/L)	1.306 - 1.474
Total Sulfur (mg/L)	55.25 - 59.61
Aluminum (mg/L)	0.452 - 0.561
Barium (mg/L)	0.579 - 0.726
Calcium (mg/L)	35.810 - 43.350
Copper (mg/L)	0.023 - 0.024
Iron (mg/L)	0.238 - 0.288
Potassium (mg/L)	35.30 - 38.20
Magnesium (mg/L)	7.35 - 8.84
Manganese (mg/L)	2.032 - 2.149
Sodium (mg/L)	61.78 - 66.83
Nickel (mg/L)	0.04 - 0.08
Strontium (mg/L)	0.132 - 0.154
Zinc (mg/L)	0.343 - 0.534

Table 5.2 Main operational conditions of the TSMBR.

	Day 17-41	Day 67-105	Day 106-158
HRT(d)	1.7 ± 0.2	1.1 ± 0.1	0.9 ± 0.1
SRT (d)	20	20	20
Organic Loading Rate (kgCOD/(m^3·d))	2.76 ± 0.13	3.34 ± 0.17	3.98 ± 0.23
Flux (L/(m^{2}h))	6.8 ± 0.7	9.2 ± 0.5	11.8 ± 0.4
pH	6.9 ± 0.1	6.9 ± 0.1	6.9 ± 0.1 (7.8 at day 120)
Temperature (°C)	51 ± 1	51 ± 1	51 ± 1

5.2.2 Analytical methods

5.2.2.1 Water quality measurements

Samples of influent, permeate and mixed liquor were taken periodically from the system. COD and mixed liquor suspended solids (MLSS) were analyzed as described in Standard Methods (APHA, 2005) [23]. Supernatant COD was determined after centrifuging the mixed liquor for 15 min at 18700 x *g*. MLSS, influent COD, supernatant COD and permeate COD were routinely measured each week.

5.2.2.2 Membrane fouling rate determination

Membrane resistance was determined by using Darcy's law as follows:

$$R_t = R_m + R_c + R_p = \frac{\Delta P_t}{\eta \times J}$$

Where R_t is the total resistance (m^{-1}); R_m, R_p and R_c is the membrane, pore blocking and cake layer resistance (m^{-1}), respectively; ΔP_t is the transmembrane pressure (Kpa); η is the dynamic viscosity (Kpa·s) and J is the membrane flux ($m^3 \cdot m^{-2} \cdot s^{-1}$).

Membrane fouling rate (ΔR) of the TSAMBR system was calculated as ΔR_{24} ($m^{-1}h^{-1}$), the change rate of resistance within 24 h of filtration, according to:

$$\Delta R_{24} = \frac{R_{24} - R_0}{\Delta t}$$

Where Δt is the filtration time (h), R_0 and R_{24} is the R value (m^{-1}) at starting time and after 24 hours filtration, respectively.

5.2.2.3 EPS extraction and measurement

The extraction of bound EPS was performed according to a cation exchange resin (CER) (Dowex® Marathon® C, Na$^+$ form, Sigma–Aldrich, Bellefonte, PA, USA) method [24]: 100mL mixed liquor was taken and centrifuged (IEC MultiRF, Thermo IEC, Needham Heights, MA, USA) at 18700 x g for 15 min at 4 °C. The supernatant was removed carefully using pipette and the sludge pellets were re-suspended to their original volume using a buffer consisting of 2 mM Na$_3$PO$_4$, 4 mM NaH$_2$PO$_4$, 9 mM NaCl and 1 mM KCl at pH=7. Then, the sludge was transferred to an extraction flask with buffer solution and the CER (80 g/gMLSS) added. The suspension was stirred (Corning 171 Scholar Stirrer, Corning, USA) for extraction of EPS for 2 h at 4 °C. The extracted EPS solution was recovered by centrifuging the CER/sludge suspension for 30 min at 18700 x g at 4 °C to remove the CER and MLSS.

The EPS was then normalized as the sum of carbohydrate (CH) and proteins (PN), which were quantified by colorimetric methods proposed by Dubois et al. [25] and Lowry et al. [26], respectively. D-glucose was used as a carbohydrate standard and bovine serum albumin (BSA) was used as a protein standard.

5.2.2.4 Particle size distribution measurement and analysis

The particle size distribution (PSD) of the mixed liquor was determined by using a Malvern Mastersizer 2000 instrument (Malvern Instruments Ltd., Worcestershire, UK) with a detection range of 0.02 – 2000 μm. Scattered light is detected by a detector converting the signal to a size distribution based on volume. The PSD of cake layer sludge was conducted by carefully scraping the cake sludge from the membrane surface using a plastic sheet and then gently re-suspending the cake sludge with distilled water.

5.2.2.5   Cake layer cryosection and optical microscopic observation

After the termination of each operation cycle, the membrane module was removed from the bioreactor and the fouled membranes were used for cake layer characterization. Several small pieces (four to seven) of membrane with cake layer were cut from the membrane sheet. The small piece was cryofixed vertically or horizontally onto a sample holder using optimal cutting temperature compound (Sakura Finetechnical Co. Ltd. Tokyo, 103, Japan) at the temperature of -21°C. The samples were then mounted in a cryostate microtome (Histostate Microtome, Model 855, Reichert Scientific Instruments Division of Warner Lambert Technologies Inc., NY, USA) for cryosectioning. The vertically fixed cake layer covered membrane were sliced into thin film for their cross-section view, and the horizontally fixed ones were sectioned into a surface layer and a bottom layer for the observation of spatial change of the cake layers. The cryosectioned slices were then observed by a conventional optical microscope (COM) station with a phase contrast illumination (Olympus IX51, Japan).

The areal porosity of the cake layers can be determined by the combination of COM and image processing software [27]. Briefly, the COM images were acquired and transferred to gray-scale formation (256 gray-scale levels) with Adobe Photoshop CS5. Before analyzing an image, a threshold has to be determined in order to distinguish pores from the background, obtaining a binary image. The pore area values can be determined by analyzing the binary images.

5.3   Performance of the TSAMBR – EO System

5.3.1   Performance of the TSAMBR

The TSAMBR system was operated for over 5 month for the treatment of thermomechanical pulping pressate at a thermophilic temperature of 51 ± 1 °C. As shown in Fig. 5.2, the whole

operating period can be divided into 5 stages: acclimation stage (day 1 -17), HRT = 1.7 ± 0.2d

stage (day 18 - 41), 1.1 ± 0.1d stage (day 67 - 105), and 0.9 ± 0.1d stage (day 106 - 156) with a

system upset stage from day 42 to 66. The decreased HRT from 1.7 ± 0.2d to 0.9 ± 0.1d was

achieved by increasing permeate flux from around 6.8 ± 0.7 to 11.8 ±0.4 L/(m^2 h), which also led

to an slight increase in MLSS concentration from 10.0 to 12.0 g/L (Fig. 5.2a). Previous studies

demonstrated that the concentration of MLSS ranging from 8 to 12g/L [28] and from 9 to 14g/L

[29] does not appear to have significant effect on the membrane fouling. The COD in the

influent, supernatant and permeate are presented in Fig. 5.2b. The influent COD value varies

from 3343 to 4250 mg/L, while the steady-state permeate COD value at HRT of 1.7 ± 0.2, 1.1 ±

0.1, 0.9 ± 0.1d and was 385, 292, and 393 mg/L corresponding to a removal efficiency of 92%,

92% and 89%, respectively. The supernatant COD in the bioreactor was consistently higher than

the permeate COD, indicating the retention of organic compounds by the membrane and the

formed cake layer, which is consistent with the findings of previous studies [30-32]. The

significantly higher supernatant COD at an HRT of 0.9 ± 0.1d may contribute to the much faster

fouling (Fig. 5.3). A pH disruption occurred on day 120, which gave rise to deterioration in COD

degradation: both permeate and supernatant COD jumped to high values and the COD removal

efficiency dropped sharply from around 90% to 73%. Then the TSAMBR was recovered in 5

days. All of the findings indicate that the HRTs chosen in our experiments exert no significant

influence in terms of COD removal efficiency and the TSAMBR has the potential to be used as

an in-mill wastewater treatment process to achieve system closure in the pulp and paper industry

under an optimal HRT.
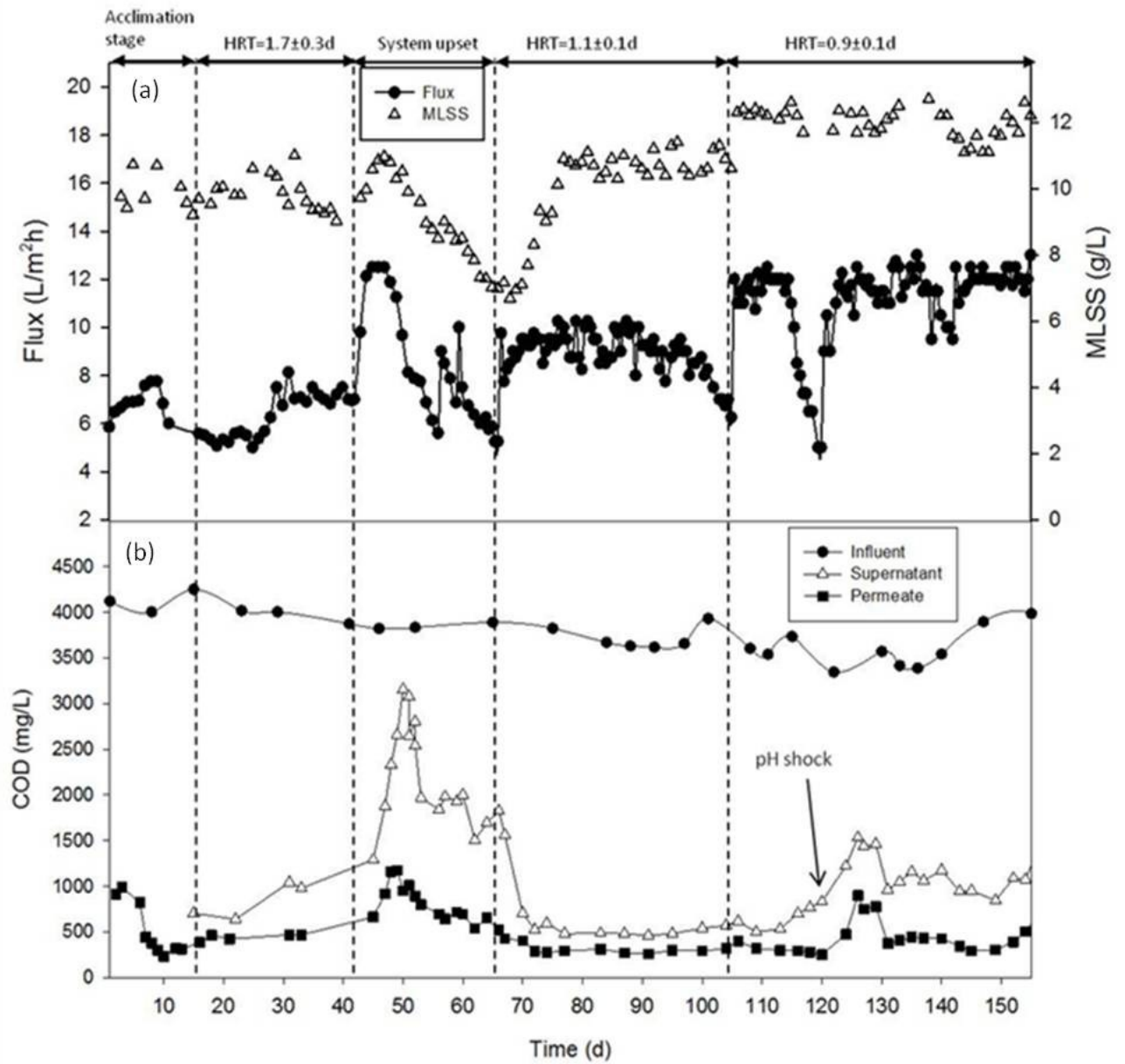
Fig. 5.2 Temporal variation of (a) membrane flux and MLSS concentration, and (b) influent, supernatant and permeate COD during the entire period of study.

Fig. 5.3 shows the TMP variations with respect to the normalized operating time at HRT of 1.7 ± 0.2, 1.1 ± 0.1 and 0.9 ± 0.1d, respectively. As expected, a shorter HRT corresponding to a higher flux resulted in a faster membrane fouling and a steeper jump of TMP. The TMP profiles of HRT

= 1.1 ± 0.1 and 0.9 ± 0.1d exhibit similar two-stage behaviours: a very low and steady TMP with subtle fluctuations at the first stage followed by an abrupt and rapid jump in TMP at the second stage. This finding is somewhat different from other investigations in which a slow and graduate increase in TMP at the first stage was observed [33-34]. This difference may be attributed to the high-temperature effects on membrane and sludge properties under the thermophilic condition. A jumping point around which distinct changes in TMP occurred was also observed for the cases of HRT= 1.1 ± 0.1 and 0.9 ± 0.1d. The similar observations have also been reported by Brooks et al. [35] and Hwang et al. [36]. However, no TMP jump was observed during the 42-day (including the acclimation stage) operation at HRT =1.7 ± 0.2d. The absence of TMP jump was presumably due to the low average flux (6.8 ± 0.7 LMH) so that 42-day operation was not long enough to reach the second stage. After taking into account of the system removal efficiency, the initial capital cost and the membrane cleaning and maintenance cost, the optimal HRT for the TSAMBR system can be for determined to be 1.1 ± 0.1d.
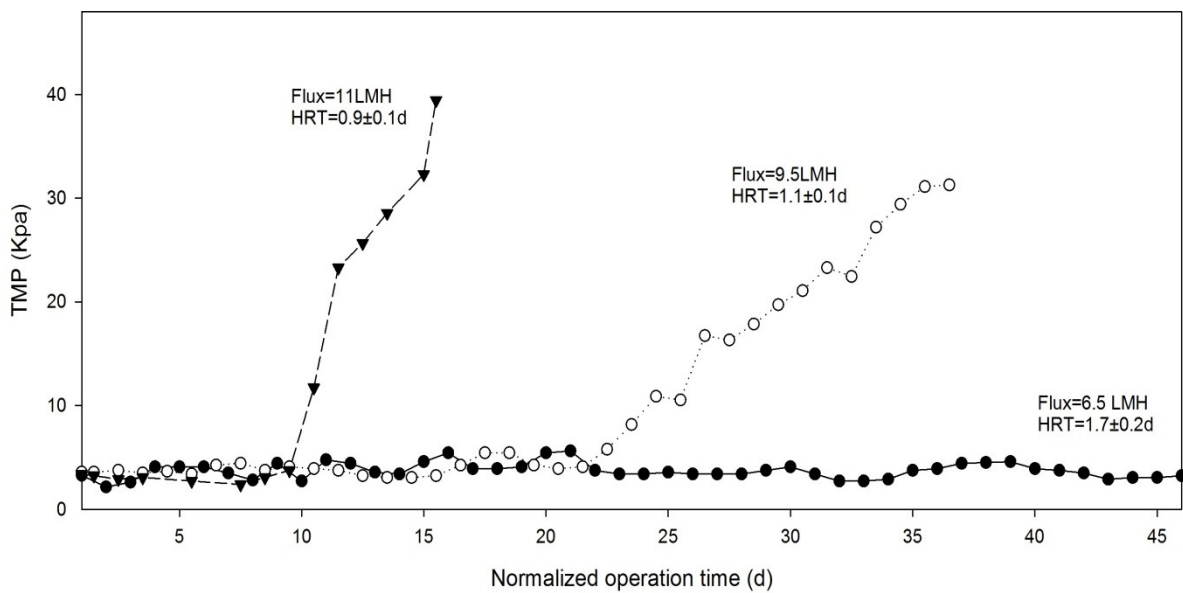

Fig. 5.3 TMP profile at different HRTs.

5.3.2 Performance of electrochemical oxidation

Fig. 5.4 shows the evident change in color of the TSAMBR effluent before and after electrochemical oxidation. The color of the TSAMBR effluent varied with HRT (Fig. 5.4a) before the electrochemical oxidation and the darker color corresponded to a higher concentration of COD (Table 5.3). As shown in Fig. 5.4b, the effluent became colorless after 5.5-hour electrochemical oxidation regardless of the HRT, indicating a complete decolourization.
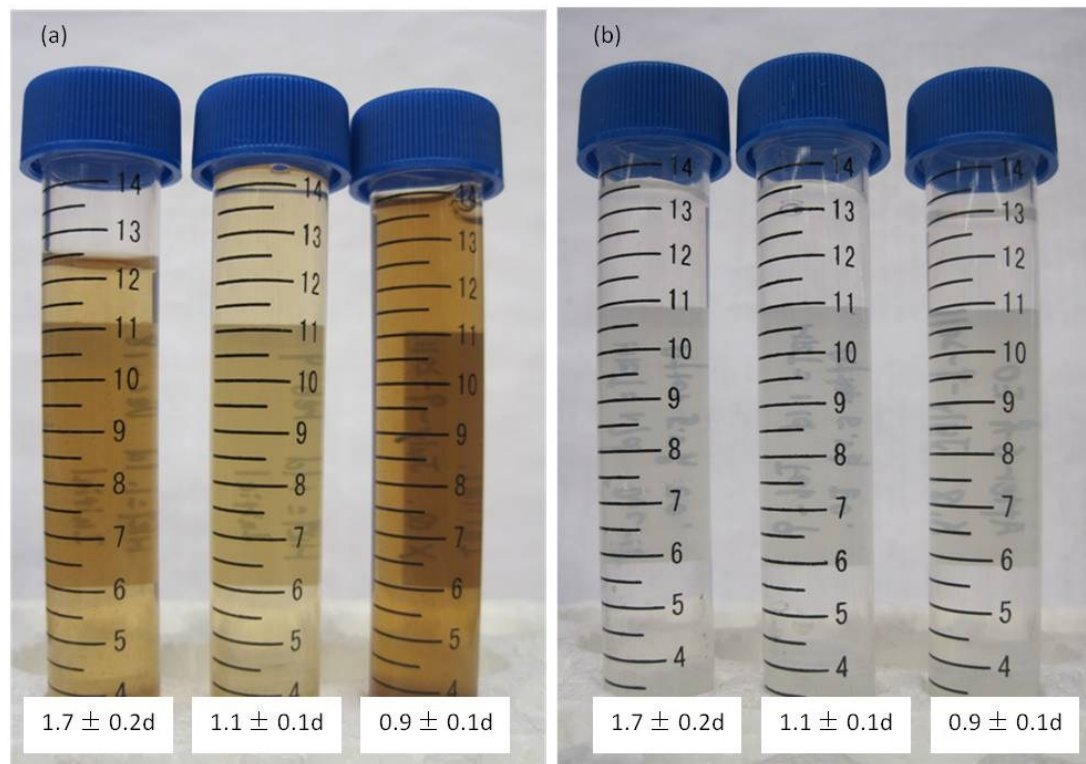
Fig. 5.4 Visual presentation of the color removal of the TSAMBR effluent by electrochemical oxidation: (a) before and (b) after electrochemical oxidation.

However, the rapid color removal could not necessarily correlate to the mineralization of the pollutants in the TSAMBR effluent. Further examination in COD revealed that the electrochemical oxidation achieved a removal efficiency of 51%, 54% and 54% for the effluent

obtained from the TSAMBR at HRT = 0.9 ± 0.1, 1.1 ± 0.1 and 1.7 ± 0.2d, respectively. The

slight variation in the COD removal efficiency of the electrochemical oxidation process could be,

mostly, attributed to the different compositions of the effluent due to the different HRT in

TSAMBR. For instance, the effluent obtained from the TSAMBR at shortest HRT may contain

more recalcitrant compounds with large molecule and complex structure from the initial

thermomechanical pulping pressate due to the insufficient biological reaction, which may

negatively affect the electrochemical oxidation process. The COD values and the overall removal

efficiency are listed in Table 5.3. It can also be found that the overall removal efficiency of COD

is above 94%, with the highest value of 97%. The high COD removal efficiency along with the

colorless and solids free effluent, demonstrate the great possibility of using the TSAMBR – EO

system as an in-mill treatment process to achieve system closure.

Table 5.3 COD values and removal efficiency of TASMBR – EO system.

HRT in TSAMBR (d)	COD (mg/L)			Overall removal efficiency (%)
	Initial	After TSAMBR treatment	After 5.5-h electrochemical oxidation post treatment	
1.7 ± 0.2	4002	436	205	95
1.1 ± 0.1	3630	236	109	97
0.9 ± 0.1	3985	509	249	94

5.4   Comparison of Bulk Sludge Properties at Different HRTs

5.4.1   Particle size distributions of bulk sludge

The particle size distributions of mixed liquor in the TSAMBR at different HRTs are shown in

Fig. 5.5. With the decrease in HRT, the mean particle size (the mean diameter over the volume

distribution) shifted from 78 to 66 μm. It is also interesting to note that there were more small particles (2μm < diameter < 20μm) in the bulk sludge at the longest HRT. This is probably due to the fact that the increased HRT leads to a reduced food/microorganism ratio and bound extracellular polymeric substance (EPS) production (results are presented in later sections). The decreased EPS production will reduce the polymer bridging mechanism of sludge flocs and the embedment of small flocs in EPS matrix, and thus promote deflocculation and small flocs [37-39]. Previous studies showed that small particles had a strong tendency to deposit on the membrane surface and form a cake layer [40-41]; however, our results indicate that the larger portion of small particles at longest HRT exert an insignificant impact on the fouling tendency due to the fact that there is no increase in TMP or decrease in flux for the stable operation of 42 days (Fig. 5.3). This may attribute to the fact that the size of small particles is actually much larger than the pore size of the membrane (0.3 μm), which means that the small particles cannot block the pore entrances. In addition, the low operating flux generating small drag forces for the particles attraction, which can just form a loose gel layer rather than a compact cake layer, bring marginal impact on membrane fouling. As a result, the particle size distribution of the bulk sludge alone is not a key parameter to be directly correlated to membrane fouling in the TSAMBR, which is also consistent with findings of Le-Clech et al. [42].
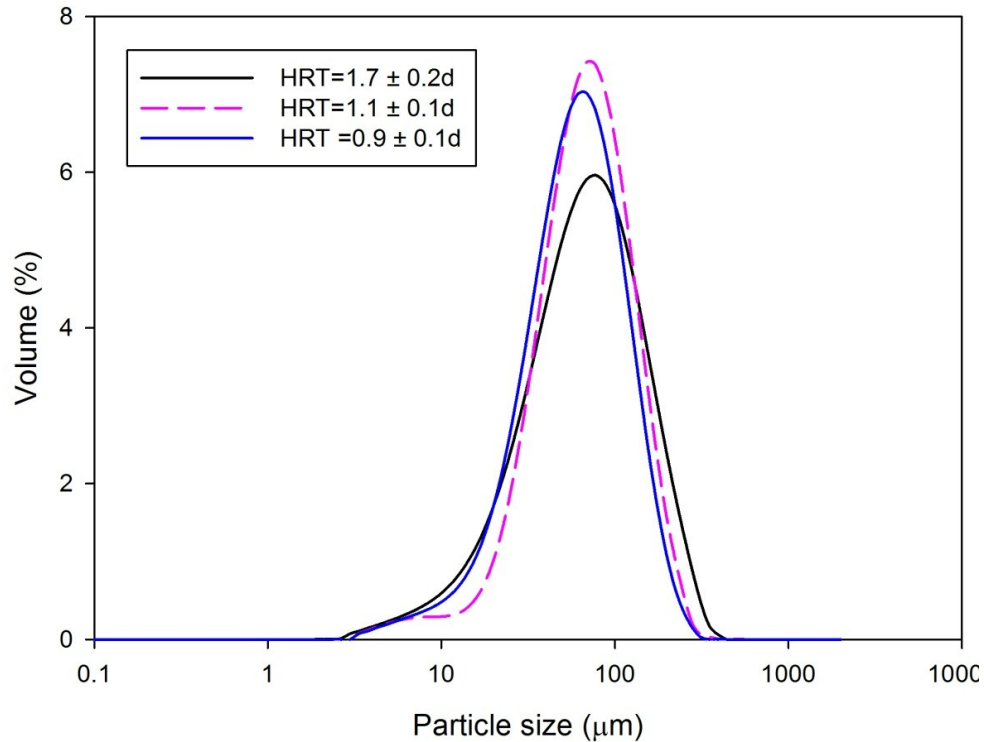
Fig. 5.5 Particle size distribution of bulk sludge at different HRTs.

5.4.2 Bound EPS of bulk sludge

Bound EPS has been identified as a key membrane fouling parameter in MBR systems [42-43]. Fig. 5.6 presents the comparison of bound EPS of the bulk sludge in TSAMBR at different HRTs. Proteins were found to be the dominant component in the EPS for all HRTs. With the decrease in HRT, the protein, carbohydrate and EPS concentration increased while the protein to carbohydrate (PN/CH) ratio decreased. HRT can govern both organic loading rate and MLSS concentration and thus, control food to microorganisms (F/M) ratio. The bound EPS is growth-related and is produced in direct proportion to substrate utilization [44], thus the decreased HRT (increased F/M) induces the generation of more bound EPS. Similarly, Meng et al. [13] reported that there were high bound EPS concentration and high sludge viscosity as F/M ratio increased. The increased EPS concentration in the bulk sludge facilitated the deposition of biomass and the

formation of cake layer and thus partially contributed to the sooner commencement of the TMP jump at shorter HRT (Fig. 5.3) [34]. Extracellular carbohydrates are synthesized for a specific function, while proteins can exist in the extracellular polymer network due to the excretion of intracellular polymers or cell lysis [45]. At longer HRT or lower F/M ratio, carbohydrates in the microbial flocs decline as an available carbon source and proteins also decrease due to the less excretion of intracellular polymers; on the contrary, at shorter HRT or higher F/M ratio, excess carbon substrates were likely to be converted to polymers accumulated in EPS and more protein were produced due to more excretion of intracellular polymers [46], which can explain the trends of carbohydrates and proteins shown in Fig. 5.6. The decrease in PN/CH ratio could correlate to the increase of non-flocculating flocs with the decrease of HRT. It was reported that a decrease in the PN/CH ratio in EPS led to poorer bioflocculation, which caused sludge particles shifting towards smaller sizes (Fig. 5.5) and thus resulted in higher propensity of membrane fouling [39]. The data obtained from the current investigation suggests that, similar to conventional MBRs, the PN/CH ratio is an important factor governing sludge particle size in the TSAMBR system, which in turn affects membrane permeability.
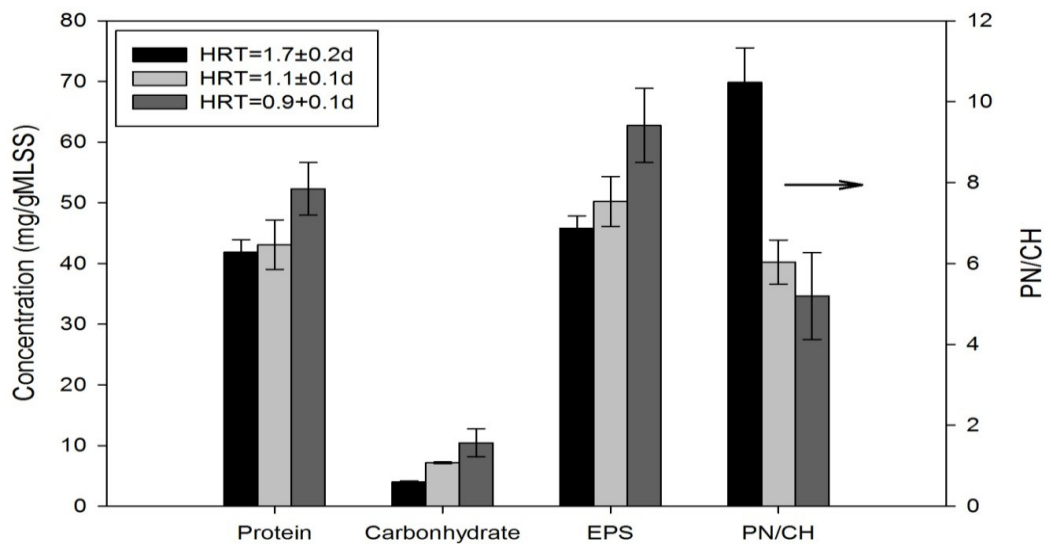

Fig. 5.6 Comparison of bound EPS of bulk sludge at different HRTs.

5.5   Comparison of Cake Sludge Properties at Different HRTs

5.5.1   Particle size distribution of cake sludge

A significant difference in the particle size distributions of cake sludge at the three HRTs was observed (Fig. 5.7). The mean particle size followed the order of HRT = 1.7 ± 0.2d < HRT= 0.9 ± 0.1d < HRT= 1.1 ± 0.1d. In addition, it is quite clear that a significantly larger portion of small particles existed in the cake sludge liquor at HRT =1.7 ± 0.2d than those at HRT of 0.9 ± 0.1d and 1.1 ± 0.1d. When compared to the bulk sludge particle size distributions shown in Fig. 5.5, the cake sludge particles at HRT = 1.7 ± 0.2d shifted to a much smaller range while those at HRT = 1.1 ± 0.1 and 0.9 ± 0.1d moved to a larger range. The small particles have stronger tendency to deposit on the membrane surface. Under a low flux (long HRT), the small particles were slowly and gradually attracted onto the membrane surface to form a thin and loose gel layer while the large flocs cannot be deposited onto the membrane due to the low drag force provided by the low flux. Our cake sludge particle size distribution for the HRT of 1.7 ± 0.2d is in line with the studies of Meng et al [47] and Wang et al [48], who reported that mean size of the washed liquid of cake layer was much lower than that of bulk sludge and gel layer formed on the membrane surface has a smaller particle size distribution compared to bulk sludge, respectively. However, at shorter HRTs, the increased flux not only drew more large particles to attach onto the membrane but also continuously compressed the cake layer to form a more compact structure due to the consolidation effect [49], which resulted in the larger particles of the cake sludge at HRT = 1.1 ± 0.1 and 0.9 ± 0.1d. Considering the insignificant difference in flux at HRT = 1.1 ± 0.1 and 0.9 ± 0.1d, the larger cake sludge particles at HRT = 1.1 ± 0.1d may be contributed by the longer operating time of 38 days (more compression) compared to that of HRT = 0.9 ± 0.1d (15 days).
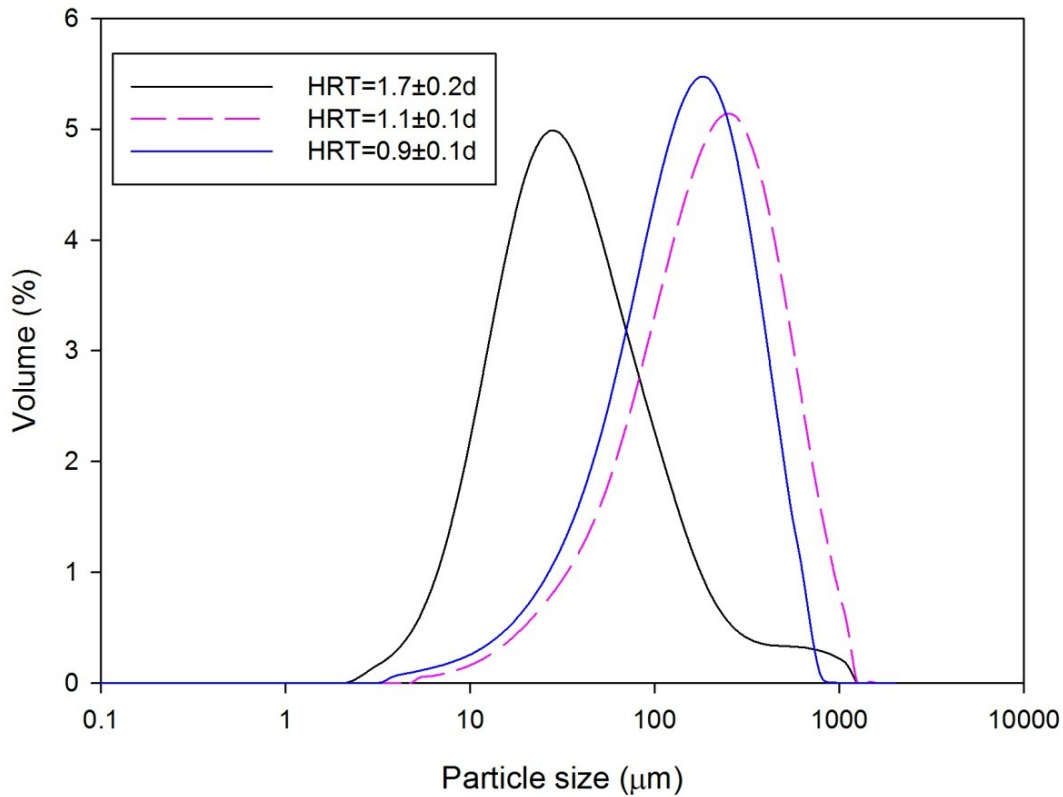
Fig. 5.7 Particle size distribution of cake sludge at different HRTs.

5.5.2 Bound EPS of cake sludge

The bound EPS profile of cake sludge at HRT = 0.9 ± 0.1 and 1.1 ± 0.1d are shown in Fig. 5.8 (no cake layer formed at HRT of 1.7 ± 0.2d). It can be found that the proteins were also the major contents of the EPS, which is consistent with the results of bulk sludge; however, no significant difference was found in the concentrations of protein, carbohydrate, EPS or the ratio of PN/CH of the cake sludge for the two HRTs. This indicates that the cake sludge EPS alone, cannot explain the distinctions in the TMP profile (Fig. 5.3) for the HRT of 0.9 ± 0.1 and 1.1 ± 0.1d. Moreover, the EPS contents of the cake sludge and the bulk sludge (Fig. 5.6) were somewhat similar. The cake sludge at HRT = 1.1 ± 0.1d had slightly more protein, carbohydrate and EPS compare to bulk sludge, while the cake sludge at HRT = 0.9 ± 0.1 produced a little less EPS. Generally speaking, there was little difference between the cake sludge and the bulk sludge

in terms of the extracellular properties of the biomass. This is consistent with the fact that the bulk sludge in the MBR suspension was the source of the cake sludge on the membrane inside the reactor [50].
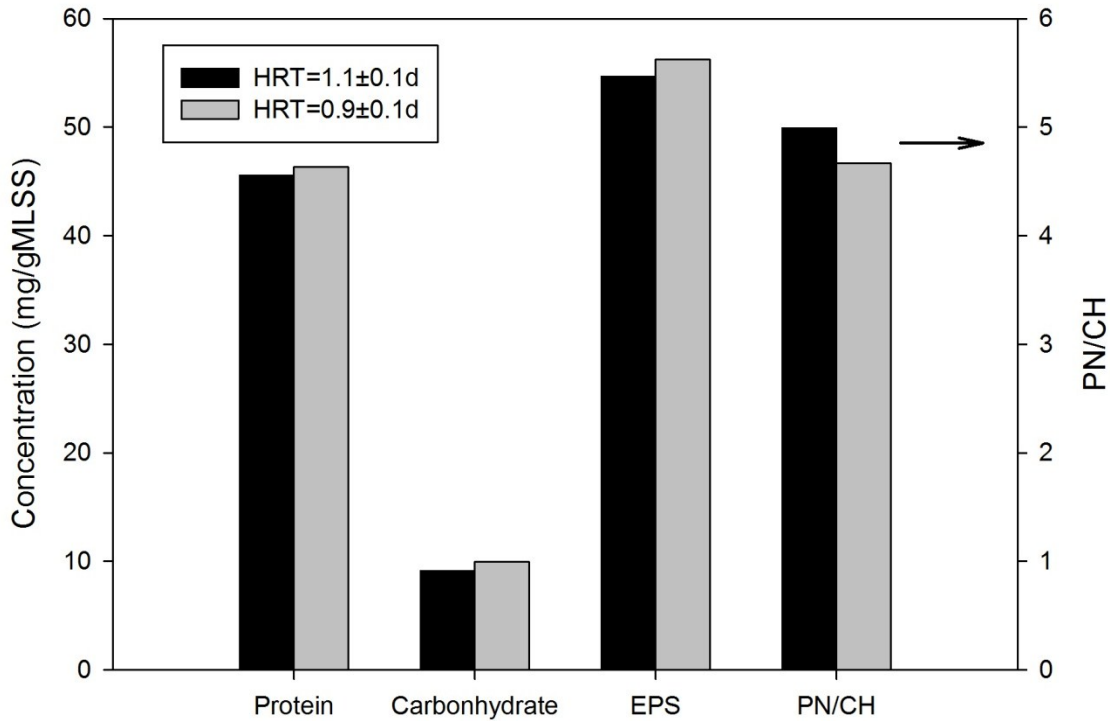

Fig. 5.8 Comparison of bound EPS of cake sludge at different HRTs.

5.5.3 Cake sludge morphology and structure

Fig. 5.9 shows the COM images and photos of the fouled membrane with cake layer coverage at the end of a filtration cycle at HRT = 1.1 ± 0.1 and 0.9 ± 0.1d. As displayed in Fig. 5.9a and b, no significant variation in terms of cake layer thickness for the two HRTs was found, even though a considerable difference existed in the length of filtration time: 36 days at HRT = 1.1 ± 0.1 vs. 15 days at HRT = 0.9 ± 0.1d. This observation is consistent with the previous findings of Hwang et al. [36] who reported that the average cake layer thickness cannot explain the TMP profile. It is also worth noting that there was no formation of cake layer after 42 days of

operation. Interestingly, the cake layer formed at HRT of 1.1 ± 0.1d demonstrated a homogenous structure (Fig. 5.9a); whereas two distinct layers along the depth of the cake layer were observed at HRT of 0.9 ± 0.1d as shown in Fig. 5.9b. This heterogeneous structure formed at shorter HRT consists of a loose surface layer and a compressed bottom layer, which is similar to the results of our previous investigation in a mesophilic anaerobic membrane bioreactor [51].

The optical microscopic images of cryosectioned slices show that the cake layer of HRT=1.1 ± 0.1d has a slight difference in the architecture of the surface and the bottom layers (Fig. 5.9c and e): larger but fewer pores on the surface vs. smaller but more pores at the bottom, whereas there was significant difference between the surface and the bottom of the cake layer formed at HRT = 0.9 ± 0.1d (Fig. 5.9d and f). These observations show a good consistency with the cross-section images of the cake layers in Fig. 5.9a and b. In addition, the photos of cake layers covered membrane (Fig. 5.9g and h) show the morphology of the cake layer at a macroscopic scale: similar structure along the depth of the cake layer at longer HRT and an inhomogeneous structure with a compact layer at the bottom and a loose gel-like layer on the top at shorter HRT, which are also in agreement with the microscopic observation. The formation of the homogeneous structure of the cake layer at HRT =1.1 ± 0.1d may be due to the long period of moderate but continuous compression, which also corresponds to the gradual increase in TMP profile (Fig. 5.3) after 22-day steady-state operation. The formation of the two-layer structure and the sooner and steeper jump in TMP at HRT = 0.9 ± 0.1d can be attributed to the high operating flux, which will be discussed in details in Section 5.6.
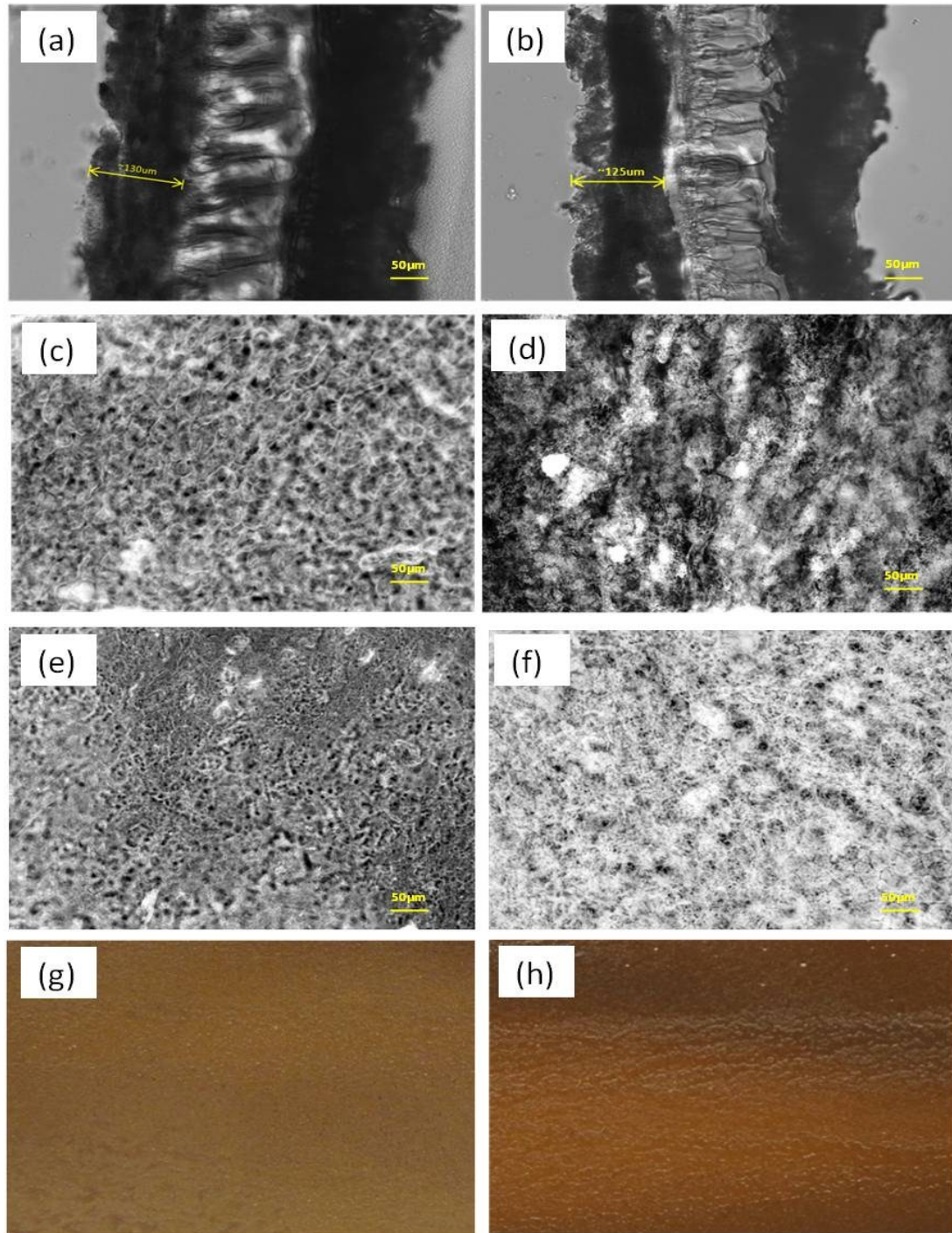
Fig. 5.9 Comparison of cake layer morphology at HRT=1.1±0.1d (a, c, e, g) and 0.9 ±0.1d (b, d, f, h): (a) – (f) COM images of cross section of cake layer (a and b), and cryosectioned slices of surface layer (c and d) and bottom layer (e and f); (g) - (h) Images of membrane with sludge cake layer.

The porosity profile of the cake layer along the depth at HRT = 1.1 ± 0.1 and 0.9 ± 0.1d is presented in Fig. 5.10 It can be found that areal porosity of the cake layer of HRT = 1.1 ± 0.1d shows minor variations from surface to bottom, although there are indeed some differences in the structure (Fig. 5.9c and e). In contrast, a sharp decrease in the porosity along the depth of the cake layer for HRT = 0.9 ± 0.1d is found, which is in good agreement with our aforementioned optical observations (Fig. 5.9) and the study of Lee et al. [52] who investigated the porosity of thin bio-cake layers (thickness < 60 μm) by using CLSM, and found a clear decrease along the depth. The porosity profile can also help to explain the distinctions of the TMP profile (Fig. 5.3). Given that there is no significant difference in the porosity of the bottom layer for the two HRTs, the sooner and steeper TMP jump of HRT =0.9 ± 0.1d is possibly caused by the higher imposed permeate flux exceeding the critical flux of the cake layer to a greater extent [34]. In addition, it can also be concluded from Fig. 5.10 that the overall cake layer porosity of HRT = 1.1 ± 0.1d is smaller than that of HRT = 0.9 ± 0.1d, indicating that the cake layer formed at HRT = 1.1 ± 0.1d is more compressed, which are likely to form larger particles in the cake sludge as illustrated in the PSD profile (Fig. 5.7).
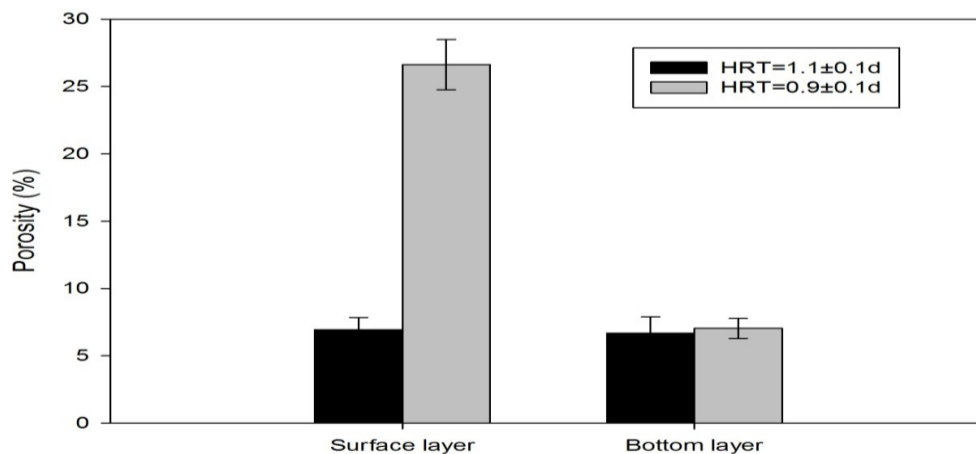

Fig. 5.10 Area porosity of the surface and bottom of cake layer at different HRTs.

5.6 Temporal Evolution of Cake Layer Formation

In addition to the spatial variation of the cake layer architecture, the evolution of cake layer formation over time is also very important for the full understanding of the mechanism of membrane fouling. However, to date, a very limited number of studies can be found in this area [36,52]; therefore, it is of great interests to investigate the temporal evolution of the formation of cake layer in the TSAMBR. In this study, we explored the variation of cake layer with operating time at HRT of 0.9 ± 0.1d. Fig. 5.11a, b and c present the photos of the virgin membrane, the membrane with thin cake layer at the commencement of the TMP jump (10 days of operation) and at the end of the TMP jump (15 days of operation) at HRT = 0.9 ± 0.1d, respectively. It can be seen that more and more biomass were deposited onto the surface of the membrane over time. The side view images of the membrane with cake layer at the beginning and the end of the TMP jump were shown in Fig. 5.11d and e, respectively. It is evident that the thickness of the cake layer increased from 0 μm to 45um over the first 10 days of operation, corresponding to the constant TMP with subtle fluctuation in stage one and the very beginning of stage two (Fig. 5.3). Then a significant and quick increase in the thickness of the cake layer from around 45 to 135 μm over 5 days was observed, which corresponds to the jump stage in the TMP profile (Fig. 5.3). The growth of cake layer would indeed increase filtration resistance; however, the thickness alone does not always coincide with membrane fouling development. For example, during the period of stage one, although the thickness of cake layer increased to about 45 μm, the membrane fouling rate was too small to be detected. However, when the cake layer further grew, the fouling rate was determined to be as high as 1.31×10^{11} $m^{-1}h^{-1}$ for the period where the TMP jump occurred. This observation is in an agreement with the findings of our previous studies in SAnMBR [51].
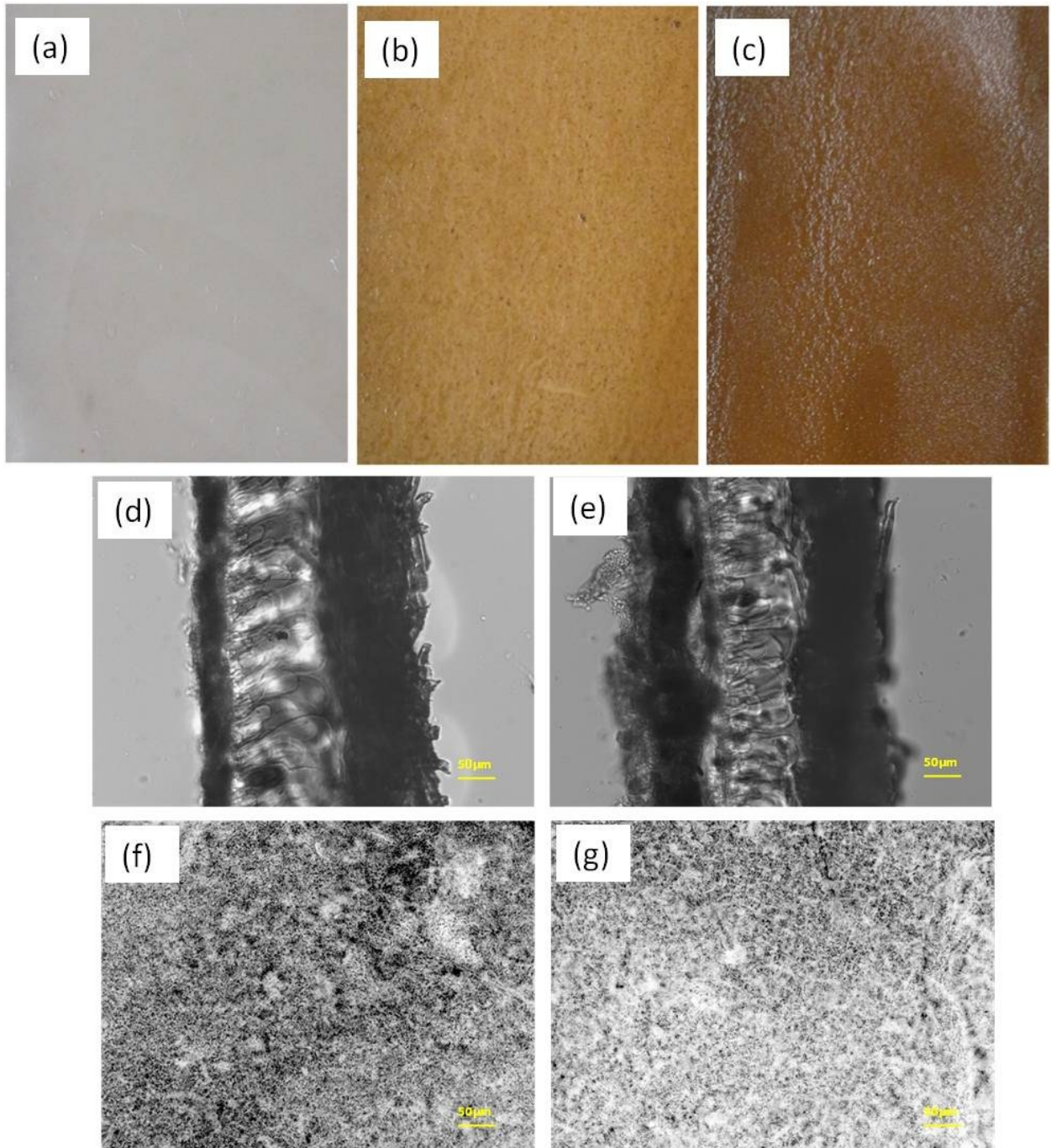
Fig. 5.11 Morphological evolution of membrane fouling at HRT=0.9 ± 0.1d. (a) – (c) Images of (a) virgin membrane, (b) onset of TMP jump and (c) end of TMP jump; (d) - (g) COM images of cross section of cake layer: (d) onset of TMP jump and (e) end of TMP jump, and cryosectioned slices of cake layer: (f) onset of TMP jump and (g) end of TMP jump.

As shown in the photos as well as the microscopic images (Fig. 5.11a-e), the thin cake layer formed at the onset of the TMP jump exhibits a homogeneous and moderate compact structure while the thicker layer developed at the end of TMP jump shows a two-layer inhomogeneous architecture with a loose top layer and a more compact bottom layer as discussed before. The COM images of the cake layers (Fig. 5.11f and g) demonstrates that the bottom layer at the end of TMP is more compact and less porous compare to the cake layer formed at the commencement of the TMP jump, further quantification reveals that the porosity of the cake layer at the beginning of the TMP jump is 11 ± 2 % vs. 7 ± 1% of the bottom layer at the end of the TMP jump. This indicates that not only the thickness but also the inner structures (e.g. porosity, compressibility etc.) of the cake layer evolves with operating time, and the critical change in the cake layer structure may be more responsible for the sudden and sharp increase in TMP [53].

The particle size distributions profile of the bulk sludge and cake layer with spatial and temporal variations at HRT of 0.9 ± 0.1d is presented in Fig. 5.12. The sludge particles of cake layer at the onset of the TMP jump was found to be much bigger than the bulk sludge and slightly shifted to larger sizes at the end of the TMP jump, possibly due to the consolidation effect caused by the long-term continuous compression. This finding also indicates the cake layer at the end of TMP jump is more compact than that at the beginning of the TMP jump, which is consistent with the change in porosity and structure (Fig. 5.11) over the operating time. In addition, the sludge particles of the surface layer of the cake layer formed at the end of TMP jump were smaller than those of the bulk sludge, indicating that the surface layer consists of a large portion of small particles with a fairly loose structure, which coincides with the observation shown in the microscopic image (Fig. 5.11e).
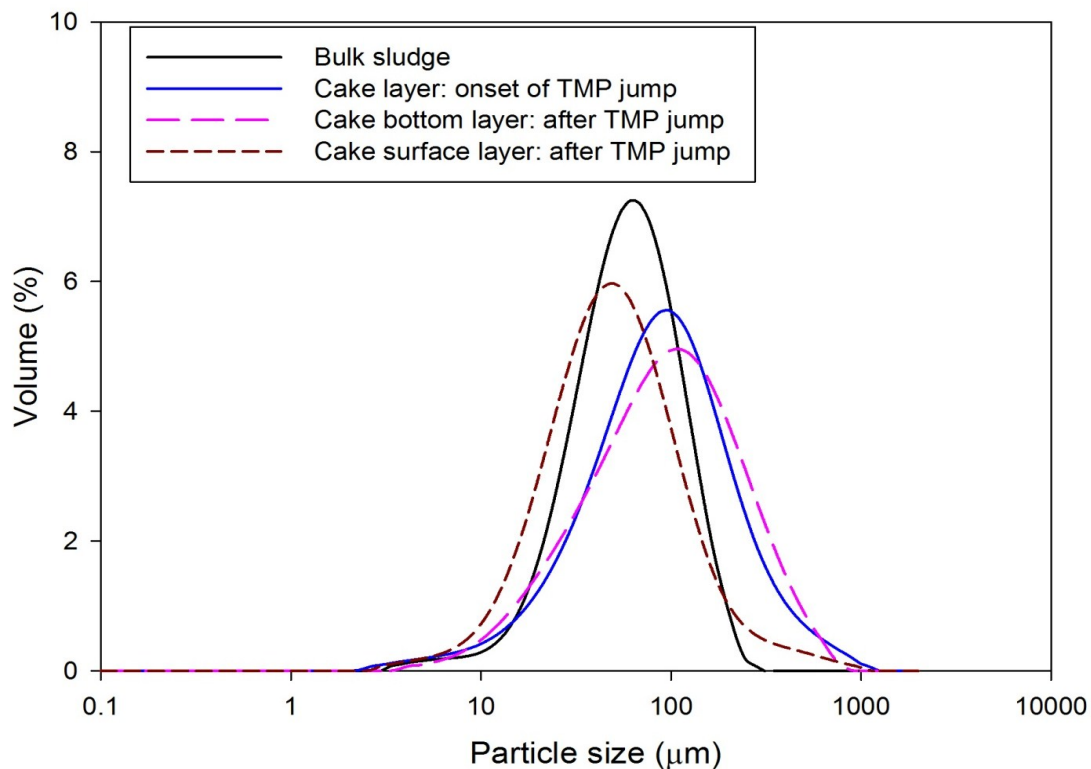
Fig. 5.12 Particle size distribution of the bulk sludge and cake layers at HRT of 0.9 ± 0.1d.

Membrane resistance is another parameter for the evaluation of membrane fouling. The total hydraulic resistance for the TSAMBR system at HRT of 0.9 ± 0.1d was measured to be 2.07×10^{13} m^{-1}, with 8.38×10^{11} m^{-1} for the virgin membrane, 8.22×10^{11} m^{-1} for pore blocking and 1.90×10^{13} m^{-1} for cake layer, corresponding to 4%, 4% and 92% of the total resistance. The results indicate that the cake layer formation is the dominant mechanism of the membrane fouling in TSAMBR, which is consistent with the findings in the mesophilic MBRs [36,47,54].

5.7 Summary

This study investigated the feasibility of using TSAMBR – EO system for treatment of thermomechanical pulping pressate and the effect of hydraulic retention time on the

performance, sludge properties and membrane fouling of a TSAMBR. Based on the results presented in this study, the following conclusions can be drawn:

1. The TSAMBR is feasible for the treatment of high-temperature and high-strength thermomechanical pulping pressate in terms of COD removal efficiency. With the influent COD concentration varying from 3343 to 4250 mg L^{-1}, an overall COD removal efficiency of 89% - 92% was achieved and an optimal HRT of 1.1 ± 0.1 was determined.

2. The TSAMBR – EO treatment process could achieve a COD removal efficiency of 94% – 97% and produce high-quality effluent free of color and solid. This shows the promise of employing this novel process for the energy utilization from thermomechanical pulping pressate and for the reuse of treated effluent for system closure.

3. Similar to the conventional MBRs, membrane fouling is also an intractable problem associated with the TSAMBR system. A two-stage TMP evolution was observed for the shorter HRTs of 1.1 ± 0.1 and 0.9 ± 0.1d. However, instead of a slow and gradual increase in TMP at the first stage as observed in most of the conventional MBRs, the first- stage TMP in TSAMBR was steady with subtle fluctuations.

4. The properties of bulk sludge vary with the HRT. The low HRT resulted in high EPS concentration, high MLSS and small sludge particles. These factors have negative effects on membrane fouling, and therefore, too low HRT should avoid for the operation of TSAMBR.

5. HRT has significant influences on the cake sludge properties. The mean particle size of cake sludge was found larger than those of bulk sludge at shorter HRT of 1.1 ± 0.1 and 0.9 ± 0.1d due to the consolidation effect, while smaller than those of bulk sludge at longest HRT because of the low permeate flux. The cake layer formed at HRT of 1.1 ± 0.1d exhibited a homogeneous and compact structure with a similar porosity along the depth and the one

developed at the shortest HRT displayed a two-layer heterogeneous architecture, resulting in a considerable difference between the porosity of the surface layer and bottom layer.

6. The thickness and the structure of the cake layer vary with operating time. The growth of the cake layer was slow at the first stage of TMP and turned to be very fast after TMP jump and the thickness of the cake layer alone does not always coincide with membrane fouling development. The cake layer changed from one homogeneous layer at the beginning of the TMP jump to two heterogeneous layers at the end of TMP jump, indicating the cake layer structure evolve over the operating time. The change in the inner structure of the cake layer i.e. reduced porosity and increased compactibility, resulted in the local flux exceeding the critical flux of the cake layer covered membrane, and subsequently led to the TMP jump. As a result, the cake layer structure is considered as a more important factor for membrane fouling in TSAMBR.

References

[1]   *Mechanical pulping* J. Sundholm, Ed.; Published in cooperation with the Finnish Paper Engineers' Association and TAPPI: Helsinki, 1999; Vol. book 5.

[2]   T. M. Lapara, J. E. Alleman, *Water Res.* **1999**, *33*, 895.

[3]   B. Q. Liao, K. Xie, H. J. Lin, D. Bertoldo, *Water Sci. Technol.* **2010**, *61*, 2177.

[4]   C. Krishna, M. C. M. Van Loosdrecht, *Water Res.* **1999**, *33*, 2374.

[5]   C. S. Tripathi, D. Grant Allen, *Water Res.* **1999**, *33*, 836.

[6]   C. S. F. Ragona, E. R. Hall, *Water Sci. Technol.* **1998**, *38*, 307.

[7]   P. R. Bérubé, E. R. Hall, *Water Sci. Technol.* **1999**, *40*, 327.

[8]   J. C. T. Dias, R. P. Rezende, C. M. Silva, V. R. Linardi, *Process Biochem.* **2005**, *40*, 1125.

[9]   R. Kurian, C. Acharya, G. Nakhla, A. Bassi, *Water Res.* **2005**, *39*, 4299.

[10]   C. Visvanathan, M. K. Choudhary, M. T. Montalbo, V. Jegatheesan, *Desalination* **2007**, *204*, 8.

[11]   N. Q. Ren, Z. B. Chen, A. J. Wang, D. X. Hu, *Int. Biodeterior. Biodegrad.* **2005**, *55*, 279.

[12]   J. W. Cho, K. G. Song, S. H. Lee, K. H. Ahn, *Desalination* **2005**, *178*, 219.

[13]   F. Meng, B. Shi, F. Yang, H. Zhang, *Bioprocess. Biosyst. Eng.* **2007**, *30*, 359.

[14]   N. Fallah, B. Bonakdarpour, B. Nasernejad, M. R. A. Moghadam, *J. Hazard. Mater.* **2010**, *178*, 718.

[15]   T. K. Chen, J. N. Chen, *Water Sci. Technol.* **2004**, *50*, 99.

[16]   K. Gommers, H. De Wever, E. Brauns, K. Peys, *Water Sci. Technol.* **2007**, *55*, 245.

[17]   G. Mascolo, G. Laera, A. Pollice, D. Cassano, A. Pinto, C. Salerno, A. Lopez, *Chemosphere* **2010**, *78*, 1100.

[18]   F. Aloui, F. Fki, S. Loukil, S. Sayadi, *Water Sci. Technol.* **2009**, *60*, 605.

[19]   K. Rajeshwar, J. G. Ibanez, G. M. Swain, *J. Appl. Electrochem.* **1994**, *24*, 1077.

[20]   K. J. Chae, S. K. Yim, K. H. Choi, S. K. Kim, W. K. Park, *Water Sci. Technol.* **2004**, *49*, 427.

[21]   H. D. Doan, J. N. Wu, R. Mitzakov, *J. Chem. Technol. Biotechnol.* **2006**, *81*, 1398.

[22]   Y. M. Lei, Z. M. Shen, R. H. Huang, W. H. Wang, *Water Res.* **2007**, *41*, 2417.

[23]   A. D. Eaton, M. A. H. Franson, *Standard Methods for the Examination of Water and Wastewater*; 21st ed.; American Public Health Association: Washington, DC, 2005.

[24]   B. Frolund, R. Palmgren, K. Keiding, P. H. Nielsen, *Water Res.* **1996**, *30*, 1749.

[25]   M. DuBois, K. A. Gilles, J. K. Hamilton, P. A. Rebers, F. Smith, *Anal. Chem.* **1956**, *28*, 350.

[26] O. H. Lowry, N. J. Rosebrough, A. L. Farr, R. J. Randall, *J. Biol. Chem.* **1951**, *193*, 265.

[27] F. G. Meng, H. M. Zhang, Y. S. Li, X. W. Zhang, F. L. Yang, J. N. Xiao, *Sep. Purif. Technol.* **2005**, *44*, 250.

[28] S. Rosenberger, H. Evenblij, S. T. Poele, T. Wintgens, C. Laabs, *J. Membr. Sci.* **2005**, *263*, 113.

[29] S. Rosenberger, C. Laabs, B. Lesjean, R. Gnirss, G. Amy, M. Jekel, J. C. Schrotter, *Water Res.* **2006**, *40*, 710.

[30] M. E. Hernandez Rojas, R. Van Kaam, S. Schetrite, C. Albasi, *Desalination* **2005**, *179*, 95.

[31] X. Huang, R. Liu, Y. Qian, *Process Biochem.* **2000**, *36*, 401.

[32] R. Kurian, G. Nakha, A. Bassi, *Chemosphere* **2006**, *65*, 1204.

[33] P. Le Clech, B. Jefferson, I. S. Chang, S. J. Judd, *J. Membr. Sci.* **2003**, *227*, 81.

[34] B. D. Cho, A. G. Fane, *J. Membr. Sci.* **2002**, *209*, 391.

[35] A. Brookes, B. Jefferson, G. Guglielmi, S. J. Judd, *Sep. Sci. Technol.* **2006**, *41*, 1279.

[36] B. K. Hwang, W. N. Lee, K. M. Yeon, P. K. Park, C. H. Lee, I. S. Chang, A. Drews, M. Kraume, *Environ. Sci. Technol.* **2008**, *42*, 3963.

[37] B. Jin, B. M. Wilen, P. Lant, *Chem. Eng. J.* **2003**, *95*, 221.

[38] B.-M. Wilén, B. Jin, P. Lant, *Water Res.* **2003**, *37*, 2127.

[39] B. Q. Liao, D. G. Allen, I. G. Droppo, G. G. Leppard, S. N. Liss, *Water Res.* **2001**, *35*, 339.

[40] W. J. J. Gao, H. J. Lin, K. T. Leung, B. Q. Liao, *Process Biochem.* **2010**, *45*, 1279.

[41] T. H. Bae, T. M. Tak, *J. Membr. Sci.* **2005**, *264*, 151.

[42] P. Le-Clech, V. Chen, T. A. G. Fane, *J. Membr. Sci.* **2006**, *284*, 17.

[43]   F. Meng, S.-R. Chae, A. Drews, M. Kraume, H.-S. Shin, F. Yang, *Water Res.* **2009**, *43*, 1489.

[44]   C. S. Laspidou, B. E. Rittmann, *Water Res.* **2002**, *36*, 2711.

[45]   R. Bura, M. Cheung, B. Liao, J. Finlayson, B. C. Lee, I. G. Droppo, G. G. Leppard, S. N. Liss, *Water Sci. Technol.* **1998**, *37*, 325.

[46]   W. Lee, S. Kang, H. Shin, *J. Membr. Sci.* **2003**, *216*, 217.

[47]   F. Meng, H. Zhang, F. Yang, L. Liu, *Environ. Sci. Technol.* **2007**, *41*, 4065.

[48]   Z. W. Wang, Z. C. Wu, X. Yin, L. M. Tian, *J. Membr. Sci.* **2008**, *325*, 238.

[49]   S.-H. Hong, W.-N. Lee, H.-S. Oh, K.-M. Yeon, B.-K. Hwang, C.-H. Lee, I.-S. Chang, S. Lee, *Environ. Sci. Technol.* **2007**, *41*, 6270.

[50]   X.-M. Wang, X.-Y. Li, X. Huang, *Sep. Purif. Technol.* **2007**, *52*, 439.

[51]   W. J. Gao, H. J. Lin, K. T. Leung, H. Schraft, B. Q. Liao, *J. Membr. Sci.* **2011**, *374*, 110.

[52]   C. H. Lee, P. K. Park, W. N. Lee, B. K. Hwang, S. H. Hong, K. M. Yeon, H. S. Oh, I. S. Chang, *Desalination* **2008**, *231*, 115.

[53]   J. Zhang, H. C. Chua, J. Zhou, A. G. Fane, *J. Membr. Sci.* **2006**, *284*, 54.

[54]   I.-S. Chang, S.-N. Kim, *Process Biochem.* **2005**, *40*, 1307.

Chapter 6. Determination of Chemical Oxygen Demand Based on Novel Photoelectro-bifunctional Electrodes*

6.1 Introduction

Considering the increasing quantities of pollutants being discharged into water bodies, environmental monitoring and control have become issues of global concern [1]. Chemical oxygen demand (COD) is one of the most widely used parameters in the assessment of water quality and pollution control as it can comprehensively represent the organic pollution level [2-3]. COD is defined as the number of oxygen equivalents consumed in the oxidation of organic compounds by strong oxidizing agents, such as dichromate or permanganate [4]. Though COD is commonly used, the standard methods for its determination have several drawbacks. They requires reflux over a long period of time (2-4 h) to achieve complete oxidation and consume expensive (e.g. Ag_2SO_4), corrosive (e.g. concentrated H_2SO_4), and toxic (e.g. Hg^{2+}, $Cr_2O_7^{2-}$) reagents. The inherent problems of long analysis time and high demanding experimental conditions make the methods unsuitable for the rapid and on-site monitoring of COD [5-6].

A great deal of effort has been devoted to improve standard methods for COD measurement. In an attempt to shorten the time of COD determination, modified standard methods have been developed using microwave-assisted and/or ultrasound-assisted digestion [7-10] and employing spectrophotometry, flame atomic absorption spectrometry and chemiluminescence as detection techniques [11-13]. In recent years, developing rapid and environmentally friendly methods for the determination of COD has attracted more attention. Most of these new methods were based on electrocatalysis (EC) using PbO_2 [14-15], Cu/CuO [16] and BDD [17] electrodes, photocatalysis (PC) and photoelectrocatalysis (PEC) with TiO_2-based materials [18-26].

Although these methods have demonstrated many advantages over the traditional COD methods such as the rapid analysis, directness of acquisition of analytical signals and possibility of incorporation into online monitoring, they are still far from perfect. The EC method is not reliable enough due to its incapacity of effectively oxidizing a wide spectrum of organic compounds. Moreover, electrodes with PbO_2 materials pose the risk of releasing toxic Pb during their preparation, determination and disposal. The PC method suffers from the easy recombination of the photogenerated electro-hole pairs, which implies a narrow dynamic working range and relatively poor reproducibility of COD measurements. The PEC method is the most promising alternative in which a potential bias is applied in the photocatalytic degradation using a TiO_2 electrode. The oxidation efficiency was enhanced due to the fact that the applied potential is able to reduce the photogenerated electron-hole recombination [27]. However, PEC can only be regarded as electro-assisted photocatalysis as the electrocatalysis doesn't function during this process.

To tackle these problems, for the first time, we report on a novel bifunctional electrode, $TiO_2/Ti/TiO_2$-Pt, involving an integration of photocatalytic degradation and electrocatalytic oxidation for COD determination. The photocatalyst, highly-ordered TiO_2NTs, was fabricated on both sides of a Ti plate by anodic oxidation [28-29], whereas the electrocatalyst, PtNPs, was loaded on one side of the fabricated TiO_2NTs by the photoreduction method [30-31]. We thus call the prepared samples bifunctional electrodes. Our study shows that with the unique double-side configuration of the electrode and the applied potentials not only greatly improves the performance of the TiO_2NTs photocatalyst, but also effectively drives the electrochemical oxidation of the organics at the PtNPs electrocatalyst. The photoelectro-bifunctional catalysis (PEBC) exhibited enhanced catalytic activity due to the synergistic effect of EC and PEC [32],

which resulted in a wider linear range, higher sensitivity and stability than either the EC or PEC method for COD determination.

6.2 Experimental Section

6.2.1 Reagents and materials

Titanium plates (1.25 cm × 0.8 cm × 0.5 mm, 99.2%) were purchased from Alfa Aesar. Dimethyl sulfoxide (DMSO) and methanol were obtained from Caledon Laboratories Ltd, Canada. Acetic acid came from Anachemia. Hydrofluoric acid (HF, 50 %), $H_2PtCl_6 \cdot 6H_2O$, D-glucose, potassium hydrogen phthalate (KHP), lactic acid, maleic acid, phenol, sodium sulfate, sodium chloride, sulfuric acid were used as received from Sigma-Aldrich. Ultrapure water (18.2 MΩ cm) used to prepare all solutions was purified by a Nanopure® Diamond ™ water system.

6.2.2 Preparation and characterization of TiO_2/Ti/TiO_2-Pt bifunctional electrode

The TiO_2NTs photocatalyst was synthesized onto both sides of titanium plates by anodic oxidation [28-29]. Briefly, pure titanium plates were ultrasonically cleaned in acetone and pure water, and then etched in an 18% HCl solution at 85 °C for 10 min. The etched titanium plates were rinsed thoroughly with pure water and then anodized in an electrochemical cell in a solution containing dimethyl sulfoxide (DMSO) and hydrofluoric acid (2% HF) at 40 V for 8 h. The anodization was carried out at room temperature, with two platinum foils used as the counter electrodes (one foil for each side of the titanium plate). After the anodization, samples were rinsed thoroughly with pure water. As an anatase structure is known to be the most efficient TiO_2 structure for photocatalysis, the synthesized TiO_2NTs were annealed at 450 °C for 3 h to form the anatase phase [33].

The surface morphology of the $TiO_2/Ti/TiO_2$-Pt electrode was characterized using scanning electron microscopy (SEM) (JEOL JSM 5900LV). The surface composition was examined by an energy dispersive X-ray spectrometer (EDS) (Oxford Links ISIS). The X-ray diffraction (XRD) patterns of the electrode were recorded using Pananalytical X'pert Pro Diffractometer.

In order to fabricate the photoelectro-bifunctional electrode, the electrocatalyst, PtNPs, was deposited on one side of the double-face TiO_2NTs electrode by a photoreduction method [30-31]. The PtNPs were loaded onto the surface of TiO_2NTs by reducing the Pt^{4+} ions photocatalytically using $H_2PtCl_6 \cdot 6H_2O$ as Pt precursor in methanol/water (1/1, v/v) solution. First, the prepared TiO_2NTs electrode with one side being covered was immersed in a quartz tube containing 5 mL methanol/water solution and 0.04 mL of 0.2 M $H_2PtCl_6 \cdot 6H_2O$ for 30 min with an argon stream purging the solution. Then the tube was sealed with an air-tight rubber cap and exposed to UV irradiation using a 150 W Xenon Arc lamp (LOT-oriel GmbH&Co. KG, Germany) for 30 min. This process was repeated for three times to secure certain amount of PtNPs to be deposited onto TiO_2NTs. Finally, the obtained electrode was baked in an argon flow at a temperature of 250 °C for 2 h to stabilize the deposited PtNPs.

The surface morphology of the $TiO_2/Ti/TiO_2$-Pt electrode was characterized using scanning electron microscopy (SEM) (JEOL JSM 5900LV). The surface composition was examined by an energy dispersive X-ray spectrometer (EDS) (Oxford Links ISIS). The X-ray diffraction (XRD) patterns of the electrode were recorded using a Pananalytical X'pert Pro Diffractometer.

6.2.3 Electrochemical and photochemical measurements

All the electrochemical and photoelectrochemical experiments were conducted using an electrochemical workstation (CHI660B, CH instrument Inc.) connected with a lab-made, three-

electrode cell at room temperature. The TiO_2/Ti/TiO_2-Pt electrode was used as the working electrode, a Pt coil as the counter electrode and an Ag/AgCl (saturated KCl) electrode as the reference electrode. The UV irradiation source was CureSpot 50 (ADAC systems) equipped with an Hg lamp with measured light irradiance of 2.0 mW/cm^2. The light from the source was guided through a fiber and projected on the surface of the fabricated TiO_2NTs photocatalyst.

6.2.4 Determination of COD

The electrochemical and photoelectrochemical measurements of COD were carried out in 10 mL of 0.5 M Na_2SO_4 stirred by a magnetic stirrer bar. The linear sweep voltammetry was employed to record the corresponding increase in current due to the electrocatalytic and photoelectrocatalytic oxidation of the injecting aliquots of organic compounds solutions and wastewater samples. The measured net increase in current was converted to the equivalent COD according to the calibration curve determined by known synthetic samples including D-glucose, KHP, acetic acid, lactic acid, maleic acid and phenol.

6.3 Characterization of the TiO_2/Ti/TiO_2-Pt Bifunctional Electrode

6.3.1 Surface characterization of the TiO_2/Ti/TiO_2-Pt electrode

The morphology and composition of the TiO_2NTs (photocatalyst) and the TiO_2NT supported PtNPs (electrocatalyst) were examined by scanning electronic microscopy (SEM) and energy dispersive X-ray spectroscopy (EDS). The crystallographic properties of the prepared electrode were identified by X-ray diffraction (XRD). Fig. 6.1A shows the typical SEM image of the photocatalyst surface. All the self-organized TiO_2NTs have a unique open-mouth structure with estimated dimensions of ~250 nm in outer diameter, ~90 nm in inner diameter and ~80 nm of wall thickness. Strong O and Ti peaks appear in the EDS spectrum of the TiO_2NTs (Fig. 6.1C).

As shown in Fig. 6.1B, the PtNPs electrocatalyst has been loaded on TiO$_2$NTs on the other side of the double-face electrode by photoreduction. The success of the preparation of TiO$_2$NT supported PtNPs (TiO$_2$NTs-Pt) is further demonstrated by the EDS spectrum (Fig. 6.1C). The EDS spectrum of the TiO$_2$NTs-Pt surface displays Pt, O and Ti peaks, showing the presence of platinum on the TiO$_2$NTs. Fig. 6.1D presents the corresponding XRD patterns of the synthesized TiO$_2$NTs and TiO$_2$NTs-Pt surfaces. For the TiO$_2$NTs surface, the peaks marked with a star are derived from the Ti substrate; all other diffraction peaks are attributed to those of the tetragonal anatase TiO$_2$ phase, indicating the formation of the anatase structure [34-35]. It has been reported that the anatase form has a better photocatalytic performance than rutile and amorphous structures [36], which not only is favourable for photocatalytic degradation of organics but also opens the door for the photoreduction of Pt onto the TiO$_2$NTs. For the TiO$_2$-NTs-Pt surface, the XRD patterns demonstrate a well-crystallized structure of the Pt nanoparticles. The PtNPs exhibits strong diffraction peaks at 39.97°, 46.43°, 67.31°, which correspond to the characteristic (1 1 1), (2 0 0), (2 2 0) reflections of a Pt faced-centered cubic (fcc) structure. In addition, the average crystallite size of the formed Pt particles is calculated to be around 9 nm by employing the Scherrer equation [37].
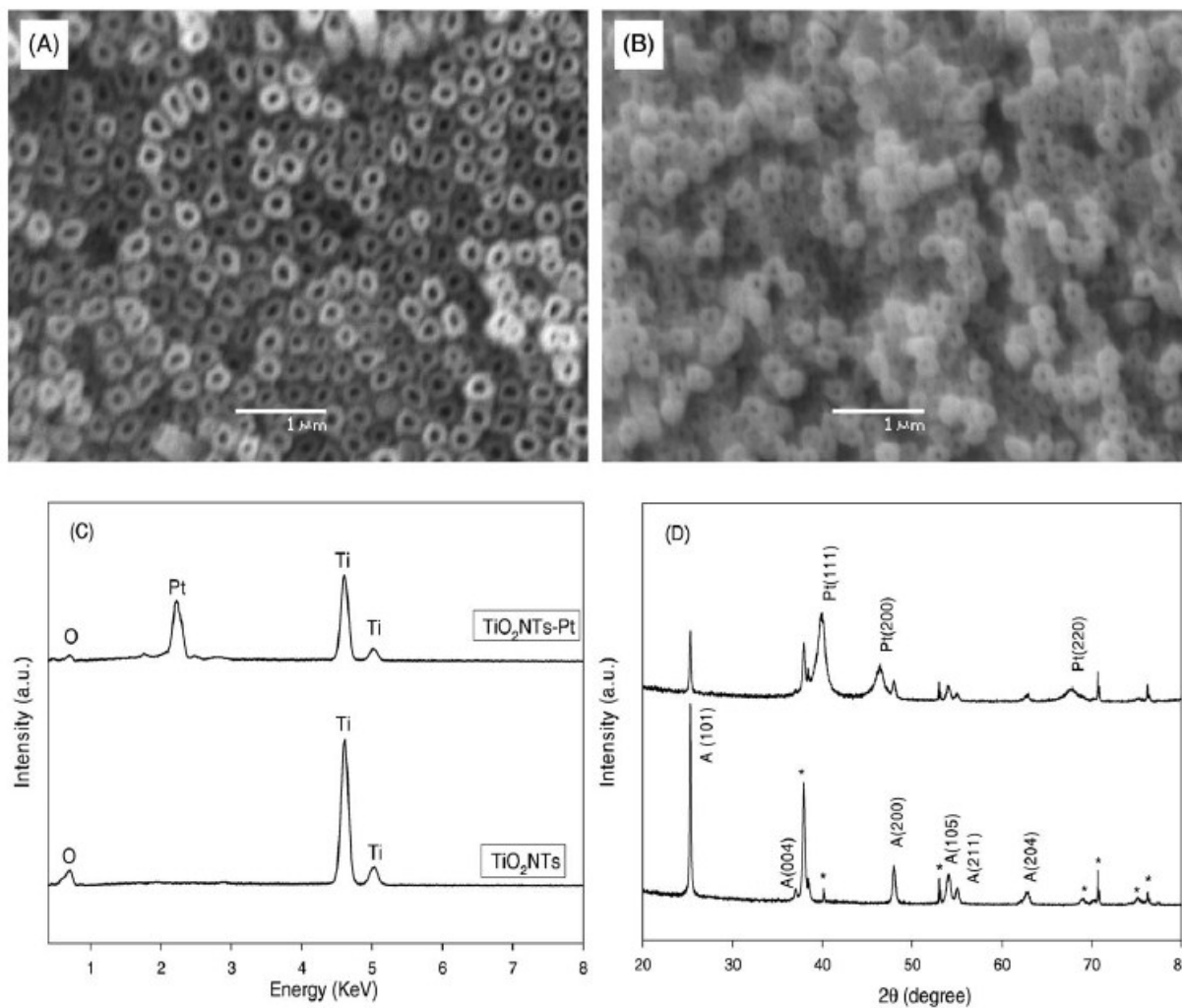
**Fig. 6.1** SEM images of the TiO$_2$/Ti/TiO$_2$-Pt bifunctional electrode: (A) the TiO$_2$NT surface and (B) the TiO$_2$NT supported PtNPs surface; (C) EDS spectra and (D) XRD patterns of the TiO$_2$NT surface and TiO$_2$NTsupported PtNPs surface.

6.3.2 Cyclic voltammograms (CVs) of the $TiO_2/Ti/TiO_2$-Pt electrode

Short-range CVs of a Pt wire (dashed line, 30-time enlarged) and the $TiO_2/Ti/TiO_2$-Pt electrode (solid line) in 0.5 M H_2SO_4 are shown in Fig. 6.2A. The two electrodes have similar hydrogen adsorption/desorption properties. The peaks observed at approximately -0.065 and -0.205 V vs. Ag/AgCl in the cathodic scan correspond to hydrogen adsorption and the peaks at about -0.18 and -0.045 V in the anodic scan are related to hydrogen desorption. Furthermore, the peak intensity of the $TiO_2/Ti/TiO_2$-Pt electrode is significantly higher than that of Pt wire electrode. It is well known that the active surface areas of Pt-containing electrodes can be determined by integrating the charge associated with the hydrogen adsorption or desorption peaks [38-40]. It is assumed that the double layer capacitance is constant across the entire investigated potential range. The charge for the hydrogen adsorption/desorption (Q_H) of the Pt wire and TiO_2NTs supported PtNPs is calculated to be 0.22 mC/cm^2 and 69.89 mC/cm^2, respectively. Q_H represents the number of the Pt sites available for hydrogen adsorption/desorption [41]; thus, the active surface area of the PtNPs is over 300 times larger than that of the Pt wire. This large electrochemical active surface area for the $TiO_2/Ti/TiO_2$-Pt electrode is in good agreement with the well-dispersed Pt nanoparticles on the TiO_2NTs as shown in Fig. 6.1B.

Fig. 6.2B compares long-region CVs of the Ti/TiO_2NTs and $TiO_2/Ti/TiO_2$-Pt electrodes recorded in 0.5 M H_2SO_4 at a scan rate of 20 mV/s. TiO_2NTs are known as a semiconductor and have poor catalytic activity in the absence of UV irradiation. As expected, neither an oxidation nor reduction peak is found in the CV of the Ti/TiO_2NTs electrode. In contrast, for the $TiO_2/Ti/TiO_2$-Pt electrode, clear and characteristic Pt surface electrochemical behaviour is observed. Apart from the aforementioned hydrogen adsorption/desorption properties, the wave associated with surface oxidation, $E_{1/2}$=0.62 V vs. Ag/AgCl, is well formed, and a large sharp reduction peak

centered at 0.40 V is also observed during the cathodic scan. The features of the CV are consistent with those of the Ti/Pt and Pt wire electrodes reported in our previous work [39]. The above results demonstrate that the PtNPs deposits significantly increase the electrocatalytic activity of the electrode and have the potential to oxidize a wide range of organic compounds.
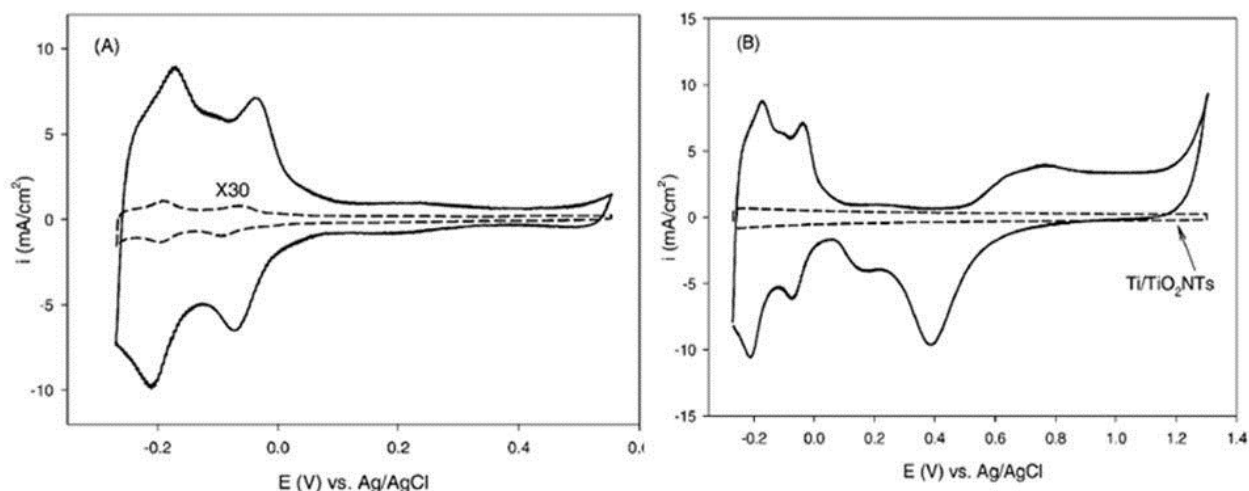

Fig. 6.2 Cyclic voltammograms of TiO_2/Ti/TiO_2-Pt (solid line), Pt wire (30-time enlarged) and Ti/TiO2NTs electrodes in 0.5 M H_2SO_4 at a potential scan rate of 20 mV/s. (A): -0.27-0.55 V. (B) -0.27-1.30 V.

6.3.3 Current responses of the TiO_2/Ti/TiO_2-Pt electrode under the condition of EC and PEBC

Fig. 6.3A presents the PEBC current (a) and EC current (b) responses of the prepared electrode in 0.5 M Na_2SO_4 solution at a scan rate of 20 mV/s. An evident increase in current from EC to PEBC is observed over potential range of 0.20 to 1.00 V due to the UV irradiation. Moreover, the photoelectrocurrent (difference between curve a and b) increases with the increase of the applied potentials, likely due to the decrease of the recombination of the photogenerated electrons and holes [42-43]. Further scanning the potential from 1.00 to 1.35 V, both of the EC

and PEBC currents undergo a sharp increase and the photoeletrocurrent is reduced due to fierce oxygen evolution.

Fig. 6.3B shows the photocurrent response of the $TiO_2/Ti/TiO_2$-Pt electrode at an applied electrode potential of 1.2 V in 0.5 M Na_2SO_4 solution. In the dark, the EC current density is measured to be 0.2 mA/cm^2 as PtNPs is an effective electrocatalyst [44]. A large instant generation of photocurrent (1.05 mA/cm^2) arose when the electrode was illuminated by a UV light with a low intensity of 2.0 mW/cm^2. The photocurrent kept constant when the UV light was turned on and quickly fell to zero once the light was switched off, demonstrating a quick response of the fabricated TiO_2NTs to the UV light.
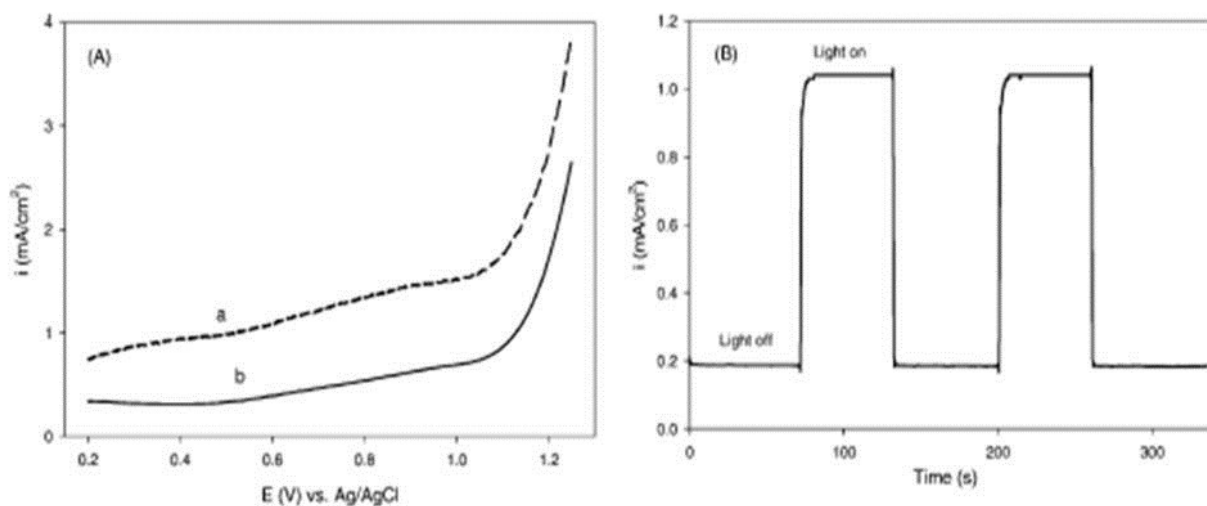

Fig. 6.3 (A) Linear sweep voltammograms of $TiO_2/Ti/TiO_2$-Pt bifunctional electrode at a potential scan rate of 20 mV/s in 0.5 M Na_2SO_4: current with (a) and without (b) UV irradiation. (B) Photocurrent response of the as-prepared bifunctional electrode under UV illumination at an applied potential of 1.2 V vs. Ag/AgCl in 0.5 M Na_2SO_4.

6.4 Photoelectro-bifunctional Catalytic Effect of the TiO$_2$/Ti/TiO$_2$-Pt Electrode

To investigate the dependence of oxidation current response on the applied potentials for the electrode, experiments with KHP solution were conducted in the presence and in the absence of UV irradiation. The linear sweep voltammograms of the TiO$_2$/Ti/TiO$_2$-Pt electrode at EC and PEBC conditions are shown in Fig. 6.4A. Curve a displays the dark current without KHP solution and UV irradiation. The oxidation current response of the addition of KHP solution without UV illumination is depicted in curve b. It is noticed that at the potential below 1.00 V, the increase in potential results in the increase in current response due to the electrocatalytic function of the TiO$_2$ supported PtNPs. Under the UV irradiation, similar behaviour but a much larger oxidation current is observed owing to the TiO$_2$NTs and TiO$_2$NTs-Pt photoelectro-bifunctional catalysis (curve c). This finding confirms the characteristic of photoelectrocatalysis synergetic effect of the TiO$_2$/Ti/TiO$_2$-Pt electrode. When the applied potential exceeds 1.00V, oxygen evolution is fierce and causes a decrease in photocurrent.

The linear sweep voltammograms of successive injections of 50 μL of 10 g/L KHP solution without and with UV irradiation are shown Fig. 6.4 B and C, respectively. It can be seen that the maximum oxidation current response of the added KHP solution appears at 1.00V vs. Ag/AgCl in both cases of EC (Fig. 6.4B) and PEBC (Fig. 6.4C), and thus, the current response at 1.00V in the linear sweep voltammograms is chosen to correlate the COD value in the following experiments. The net current response is measured to be only 1.0μA per 1.0 mg/L KHP in EC and as high as 4.4μA per 1.0 mg/L KHP in PEBC at the potential of 1.00V, further showing the photoelectro-synergistic effect of the bifunctional electrode. For the oxidation of KHP on the TiO$_2$/Ti/TiO$_2$-Pt electrode without UV irradiation (Fig. 6.4B), the electrode exhibits electrochemical activity due to the PtNPs on the TiO$_2$NTs.
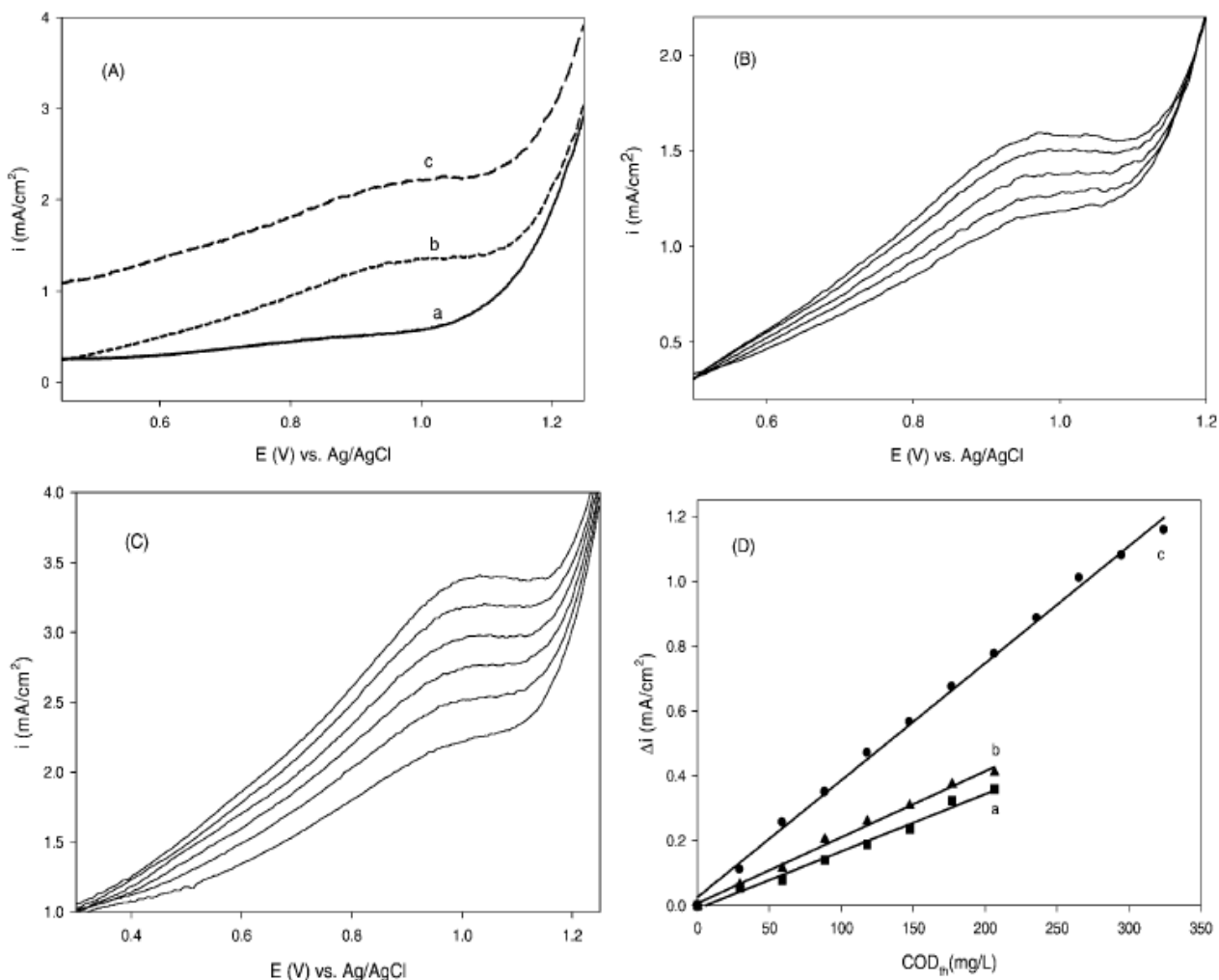
Fig. 6.4 (A)-(C) Linear sweep voltammograms of $TiO_2/Ti/TiO_2$-Pt bifunctional electrode at a potential scan rate of 20 mV/s in 0.5 M Na_2SO_4. (A) The current responses: (a) without KHP, (b)-(c) with addition of 20 μL of 50 g/L KHP by electrocatalysis (b) and photoelectro-bifunctial catalysis (c). (B)-(C) The current responses: successive addition of 50 μL of 10 g/L KHP by electrocatalysis (B) and photoelectro-bifunctional catalysis (C). (D) Plot of net increase in current vs. COD_{th} with successive addition of 25 μL of 10 g/L KHP: (a) electrocatalysis, (b) electro-assisted photocatalysis and (c) photoelectro-bifunctional catalysis.

It is known that before the oxidation of organic compounds on the Pt electrode, surface oxidation of Pt first occurred with the increase in applied potentials [45-46]:

$$Pt + H_2O \rightarrow PtO + 2H^+ + 2e^- \tag{1}$$

Then, the hydroxyl radicals (·OH) generated from the anodic discharge of water adsorbed on PtO can oxidize the organic compounds (R) to produce the current response [14]. The whole process can be represented by the following two equations:

$$PtO + H_2O \rightarrow PtO(\cdot OH) + H^+ + e^- \tag{2}$$

$$PtO(\cdot OH) + R \rightarrow PtO + R^{\cdot} + H^+ + e^- \tag{3}$$
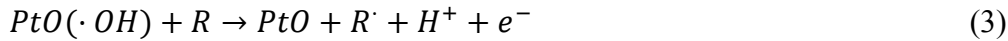
When the UV illumination was applied, the oxidation current responses of successive injections of the KHP solution on the $TiO_2/Ti/TiO_2$-Pt electrode were recorded in Fig. 6.4C. In addition to the current responses provided by the PtNPs electrocatalyst, electro-assisted photocatalytic oxidation of organic species at the TiO_2NTs photocatalyst also contributed to the oxidation current. It is known that the strong oxidant, photogenerated holes could oxidize water adsorbed on the TiO_2NTs surface to create the strong oxidizing agent hydroxyl radical. Both the photogenerated holes and hydroxyl radical could oxidize organic compounds to produce the current as represented by the following reactions [47-48]:

$$TiO_2 + hv \rightarrow h^+ + e^- \tag{4}$$

$$TiO_2 + h + H_2O \rightarrow TiO_2(\cdot OH) + H \tag{5}$$

$$h^+ + R \rightarrow R^{\cdot} \tag{6}$$

$$TiO_2(\cdot OH) + R \rightarrow TiO_2 + R^{\cdot} + H^+ + e^- \tag{7}$$
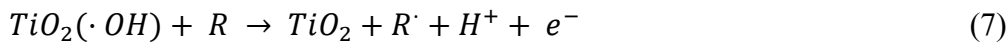
Compared with the net oxidation current responses at the applied potential of 1.0 V in EC (Fig. 6.4B), the 4-times larger current observed in PEBC (Fig. 6.4C) can be attributed to the combination of PtNPs electrochemical oxidation and the TiO_2NTs photoelectrocatalytic oxidation of organics. On the photocatalyst surface of the electrode, UV irradiation with high applied potential bias (1.0 V) prevented the recombination of photogenerated holes and electrons of the TiO_2NTs, thus, significantly improving the efficiency of the photocatalytic oxidation. Meanwhile, the PtNPs deposited on the reverse side of electrode promoted the electrochemical oxidation of organic compounds, resulting in the electrocatalytic current response. As expected, the $TiO_2/Ti/TiO_2$-Pt electrode exhibited a much higher catalytic activity for the oxidation of organic species under the high electrode potential and in the presence of UV irradiation.

The photoelectro-synergistic effect of the fabricated electrode for the oxidation of KHP is shown in Fig. 6.4D. Curves a, b and c represent the linear relationship of net current responses due to the oxidation of KHP (Δi) vs. theoretical COD (COD_{th}) under the conditions of EC (a), PEC (b) and PEBC (c). It is apparent that the slope of curve c is significantly larger than those of curves a and b, demonstrating that the sensitivity ($\Delta i / COD_{th}$) of PEBC is much higher than that of EC and PEC. Further quantification reveals that the sensitivity of PEBC, PEC and EC is 3.61×10^{-3}, 2.05×10^{-3} and 1.77×10^{-3} mA/(mg L COD_{th}), respectively. Additionally, the PEBC possesses a wider linear range (25.0-380.0 mg/L) and a lower detection limit (DL=9.5 mg/L) than those of PEC (25.0-206.0 mg/L, DL=11.8mg/L) and EC (25.0-206.0 mg/L, DL=13.7 mg/L). These results clearly show the significant advantages of the $TiO_2/Ti/TiO_2$-Pt bifunctional electrode.

6.5 Performance of the $TiO_2/Ti/TiO_2$-Pt Bifunctional Electrode for the Determination of Chemical Oxygen Demand

6.5.1 Validation of analytical principle

To validate the proposed method, a wide range of organic compounds with a known COD value were chosen. The calibration curve of net current increases (Δi) due to the oxidation of the injecting aliquot of organic compounds versus COD_{cr} of the standard samples is shown in Fig. 6.5. The net currents for all the organic compounds investigated are well fitted into the linear line $y = 0.00355x + 0.056$, where y represents the net current increase (Δi) obtained from organic oxidation and x represents the COD_{cr} value of the organics, with R=0.993. The linear relationship between the net current increase and COD value shows that the COD measured by the $TiO_2/Ti/TiO_2$-Pt electrode are almost independent of the type of organic species tested in our experiments. Furthermore, a high sensitivity of 3.55×10^{-3} mA/(mg/L COD) , a linear range of 25.0 to 380.0 mg/L COD and a low detection limit of 9.5 mg/L COD (S/N=3) are achieved.

6.5.2 Interference of chloride ion

The interference of Cl^- is a major issue in the determination of COD [49]. The effect of Cl^- concentration on COD measurement at the $TiO_2/Ti/TiO_2$-Pt electrode was investigated and the results are listed in Table 6.1. It was found that, within the concentration range of Cl^- from 0 to 1400 mg/L, the COD value obtained from the proposed method is almost independent of the Cl^- and is very close to the COD_{th} value.
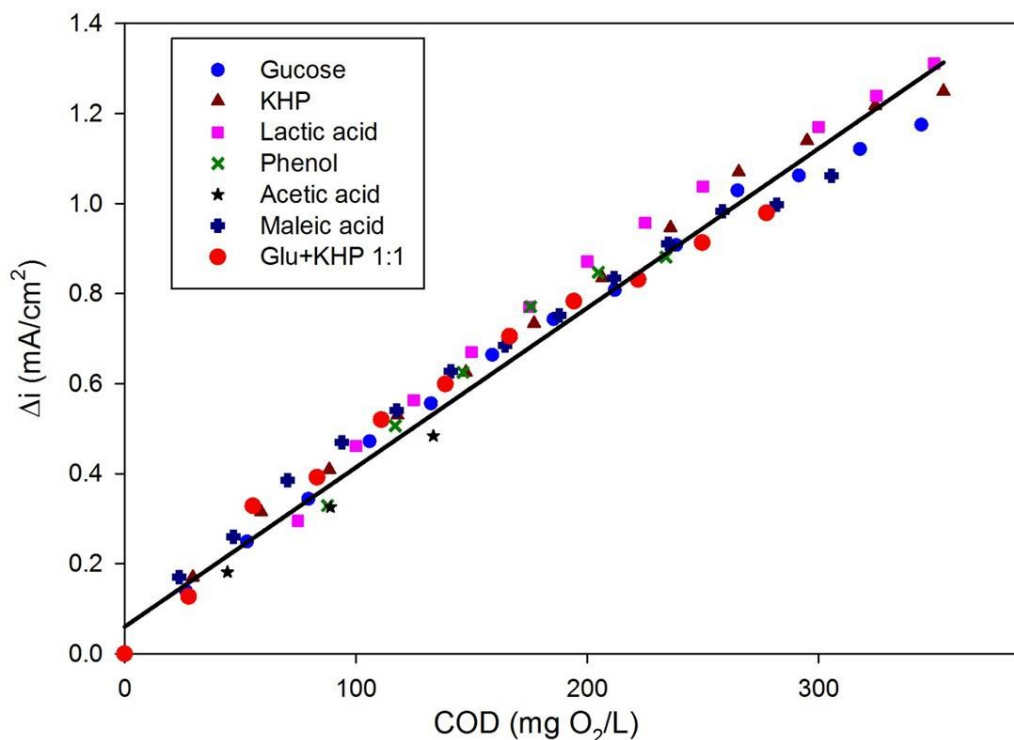
Fig. 6.5 Calibration curve of the net increase in current (Δi) vs. COD_{cr} of a number of standard samples containing D-glucose, potassium hydrogen phthalate (KHP), lactic acid, phenol, acetic acid , maleic acid and a mixture of glucose and KHP (1:1) in 0.5 M Na_2SO_4.

Table 6.1 Effect of concentration of Cl^- on the proposed COD determination method.

C_{Cl^-} (mg/L)	COD_{cr} without Cl^- (mg/L)	Proposed Method	
		COD (mg/L)	RD (%)
500	145	144.2	-0.51
800	145	145.7	0.51
1000	145	146.4	1.03
1200	145	148.9	2.74
1400	145	149.4	3.08
1500	145	132.5	-8.56

6.6 Analysis of Real Wastewater Samples

Real wastewater samples obtained from a pulp and paper mill and the effluent of a biological treatment process were collected to test the applicability of the proposed method for the COD determination. Table 6.2 shows that all the relative errors calculated from the COD values measured by the $TiO_2/Ti/TiO_2$-Pt electrode and by the standard dichromate method are within ±5.5%, demonstrating that the proposed method shows excellent correspondence with the standard method and can be successfully applied in practice.

Table 6.2 Comparison of COD values obtained by the proposed method with those from the standard method.

Sample	Proposed method		COD_{cr} method		Relative error (%)
	Mean±SD (mg/L)	RSD (%) n=7	Mean±SD (mg/L)	RSD (%) n=7	
Pulp and paper mill					
Sample 1	1897.4±54.3	2.8	1951.0±44.9	2.3	-2.76
Sample 2	1732.7±53.3	3.1	1724.5±23.1	1.3	0.46
Biological treatment effluent					
Sample 1	542.6±24.9	4.6	573.7±22.0	3.8	-5.42
Sample 2	448.6±16.9	3.7	469.4±19.9	4.2	-4.43

6.7 Summary

In summary, a novel bifunctional electrode (TiO_2/Ti/TiO_2-Pt) with the presence of an electrocatalyst (TiO_2NTs-Pt) on one side and photocatalyst (TiO_2NTs) on the reverse side was prepared for the COD determination. The electrochemical and photoelectrochemical properties of the prepared electrode were studied. The catalytic activity of TiO_2/Ti/TiO_2-Pt was greatly enhanced due to the photoelectro-synergistic effect of the electrocatalysis and photoelectrocatalysis. For the COD determination, the bifunctional electrode exhibits a very low detection limit of 9.5 mg/L, a high sensitivity of 3.55×10^{-3} mA/(mg/L COD) and a high Cl^- tolerance of 1400 mg/L. When used for the test of real wastewater samples, the electrode exhibited merits of rapidity, good accuracy, high stability and reproducibility. The results obtained from the proposed method were in excellent agreement with those determined by the standard method. All these advantages suggest that the TiO_2/Ti/TiO_2-Pt electrode can be successfully used for practical applications.

References

[1]   M. A. Shannon, P. W. Bohn, M. Elimelech, J. G. Georgiadis, B. J. Marinas, A. M. Mayes, *Nature* **2008**, *452*, 301.

[2]   A. Cuesta, J. L. Todoli, J. Mora, A. Canals, *Anal. Chim. Acta* **1998**, *372*, 399.

[3]   B. M. Jones, R. H. Sakaji, C. G. Daughton, *Anal. Chem.* **1985**, *57*, 2334.

[4]   A. D. Eaton, M. A. H. A. P. H. A. Franson, A. W. W. Association, W. E. Federation *Standard Methods for the Examination of Water and Wastewater*; 21st ed.; American Public Health Association: Washington, DC, 2005.

[5]   T. Korenaga, H. Ikatsu, *Anal. Chim. Acta* **1982**, *141*, 301.

[6]   S. Q. Zhang, L. H. Li, H. J. Zhao, G. Y. Li, *Sens. Actuators, B* **2009**, *141*, 634.

[7]   M. L. Balconi, M. Borgarello, R. Ferraroli, F. Realini, *Anal. Chim. Acta* **1992**, *261*, 295.

[8]   D. M. Dharmadhikari, A. P. Vanerkar, N. M. Barhate, *Environ. Sci. Technol.* **2005**, *39*, 6198.

[9]   A. Canals, M. D. Hernandez, *Anal. Bioanal.Chem.* **2002**, *374*, 1132.

[10]   C. E. Domini, L. Vidal, A. Canals, *Ultrason. Sonochem.* **2009**, *16*, 686.

[11]   J. Li, T. Tao, X. B. Li, J. L. Zuo, T. Li, J. Lu, S. H. Li, L. Z. Chen, C. Y. Xia, Y. Liu, Y. L. Wang, *Desalination* **2009**, *239*, 139.

[12]   A. Cuesta, J. L. Todoli, A. Canals, *Spectrochim. Acta, Part B* **1996**, *51*, 1791.

[13]   Y. G. Hu, Z. Y. Yang, *Talanta* **2004**, *63*, 521.

[14]   S. Y. Ai, M. N. Gao, Y. Yang, J. Q. Li, L. T. Jin, *Electroanalysis* **2004**, *16*, 404.

[15]   J. Q. Li, L. P. Li, L. Zheng, Y. Z. Xian, S. Y. Ai, L. T. Jin, *Anal. Chim. Acta* **2005**, *548*, 199.

[16]   C. Silva, C. D. C. Conceicao, V. Bonifacio, O. Fatibello, M. Teixeira, *J. Solid State Electrochem.* **2009**, *13*, 665.

[17]   H. B. Yu, H. Wang, X. Quan, S. Chen, Y. B. Zhang, *Electrochem. Commun.* **2007**, *9*, 2280.

[18]   S. Y. Ai, J. Q. Li, Y. Ya, M. N. Gao, Z. S. Pan, L. T. Jin, *Anal. Chim. Acta* **2004**, *509*, 237.

[19]   L. H. Zhu, Y. Chen, Y. H. Wu, X. R. Li, H. Q. Tang, *Anal. Chim. Acta* **2006**, *571*, 242.

[20]   Y. C. Kim, K. H. Lee, S. Sasaki, K. Hashimoto, K. Ikebukuro, I. Karube, *Anal. Chem.* **2000**, *72*, 3379.

[21]   J. Q. Li, L. Zheng, L. Li, G. Y. Shi, Y. Z. Xian, L. T. Jin, *Electroanalysis* **2006**, *18*, 1014.

[22] J. S. Chen, J. D. Zhang, Y. Z. Xian, X. Y. Ying, M. C. Liu, L. T. Jin, *Water Res.* **2005**, *39*, 1340.

[23] S. Q. Zhang, L. H. Li, H. J. Zhao, *Environ. Sci. Technol.* **2009**, *43*, 7810.

[24] H. J. Zhao, D. L. Jiang, S. Q. Zhang, K. Catterall, R. John, *Anal. Chem.* **2004**, *76*, 155.

[25] Q. Zheng, B. X. Zhou, J. Bai, L. H. Li, Z. J. Jin, J. L. Zhang, J. H. Li, Y. B. Liu, W. M. Cai, X. Y. Zhu, *Adv. Mater.* **2008**, *20*, 1044.

[26] J. Zhang, B. Zhou, Q. Zheng, J. Li, J. Bai, Y. Liu, W. Cai, *Water Res.* **2009**, *43*, 1986.

[27] W. H. Leng, Z. Zhang, J. Q. Zhang, C. N. Cao, *J. Phys. Chem. B* **2005**, *109*, 15008.

[28] S. Yoriya, M. Paulose, O. K. Varghese, G. K. Mor, C. A. Grimes, *J. Phys. Chem. C* **2007**, *111*, 13770.

[29] M. Tian, G. S. Wu, B. Adams, J. L. Wen, A. C. Chen, *J. Phys. Chem. C* **2008**, *112*, 825.

[30] S. Shironita, K. Mori, T. Shimizu, T. Ohmichi, N. Mimura, H. Yamashita, *Appl. Surf. Sci.* **2008**, *254*, 7604.

[31] Y. Hou, X. Li, X. Zou, X. Quan, G. Chen, *Environ. Sci. Technol.* **2008**, *43*, 858.

[32] R. M. Asmussen, M. Tian, A. C. Chen, *Environ. Sci. Technol.* **2009**, *43*, 5100.

[33] J. M. Macak, S. Aldabergerova, A. Ghicov, P. Schmuki, *Phys. Status Solidi A* **2006**, *203*, R67.

[34] R. Beranek, H. Tsuchiya, T. Sugishima, J. M. Macak, L. Taveira, S. Fujimoto, H. Kisch, P. Schmuki, *Appl. Phys. Lett.* **2005**, *87*.

[35] M. Tian, J. L. Wen, D. MacDonald, R. M. Asmussen, A. C. Chen, *Electrochem. Commun.* **2010**, *12*, 527.

[36] J. M. Macak, M. Zlamal, J. Krysa, P. Schmuki, *Small* **2007**, *3*, 300.

[37] B. E. Warren *X-ray Diffraction*; 1st ed.; Dover Publications: NY, 1990.

[38]   U. A. Paulus, A. Wokaun, G. G. Scherer, T. J. Schmidt, V. Stamenkovic, N. M. Markovic, P. N. Ross, *Electrochim. Acta* **2002**, *47*, 3787.

[39]   A. C. Chen, D. J. La Russa, B. Miller, *Langmuir* **2004**, *20*, 9695.

[40]   J. Wang, D. F. Thomas, A. Chen, *Anal. Chem.* **2008**, *80*, 997.

[41]   T. J. Schmidt, H. A. Gasteiger, G. D. Stab, P. M. Urban, D. M. Kolb, R. J. Behm, *J. Electrochem. Soc.* **1998**, *145*, 2354.

[42]   J. H. Park, S. Kim, A. J. Bard, *Nano Lett.* **2005**, *6*, 24.

[43]   G. S. Wu, J. P. Wang, D. F. Thomas, A. C. Chen, *Langmuir* **2008**, *24*, 3503.

[44]   A. Chen, P. Holt-Hindle, *Che. Rev.* **2010**, *110*, 3767.

[45]   V. I. Birss, M. Chang, J. Segal, *J. Electroanal. Chem.* **1993**, *355*, 181.

[46]   B. E. Conway, *Prog. Surf. Sci.* **1995**, *49*, 331.

[47]   I. K. Konstantinou, T. A. Albanis, *Appl. Catal., B* **2004**, *49*, 1.

[48]   J. Q. Li, L. Zheng, L. P. Li, G. Y. Shi, Y. Z. Xian, L. T. Jin, *Electroanalysis* **2006**, *18*, 2251.

[49]   W. A. Moore, R. C. Kroner, C. C. Ruchhoft, *Anal. Chem.* **1949**, *21*, 953.

Chapter 7. Summary and Future Work

In recent years, the appearance of pollutants that are recalcitrant to conventional treatments, together with stricter environmental regulations and increasing demands for water re-use, have promoted a great deal of research work toward the development of more potent, robust and environmentally benign treatment methods, as well as improved analytical techniques. In alignment with this scenario, the current M. Sc. Eng. project has set its focus mainly on the use of improved electrochemical oxidation and modified membrane bioreactor technologies for wastewater treatment, as well as the utilization of electrochemical techniques for the rapid determination of COD. The key results obtained during the course of this M. Sc. Eng. project are summarized below.

7.1 Improved Electrochemical Oxidation Process

Electrochemical oxidation is an effective approach for the decontamination of biorefractory pollutants in wastewater. However, the low concentration of pollutants and insufficient conductivity of some wastewater streams may significantly decrease the efficiency of the process. In Chapter 4, we demonstrated a novel approach through the integration of pre-concentration and electrochemical oxidation for the decontamination of phenolic compounds. The pre-concentration step was carried out by adsorbing phenol, *p*-NPh and *p*-cresol onto MN-200 resin, which exhibited high efficiency for the removal of three model pollutants. The adsorption of the three pollutants followed the Freundlich model in equilibrium and pseudo-second-order model in kinetics. Although increased temperature had a positive impact on kinetics, it reduced adsorption capacity. The adsorbed phenolic pollutants could be efficiently released using a NaOH solution, which resulted in a significantly reduced volume. This served to

greatly increase the concentration of the pollutants, as well as to enhance the conductivity of the wastewater and has opened the door for the further treatment of the pollutants utilizing advanced electrochemical oxidation on a Ti/SnO$_2$–Sb$_2$O$_5$–IrO$_2$ electrode. The electrochemical oxidation results showed that the three pollutants can be degraded efficiently and that the kinetics of the electrochemical oxidation of the three pollutants was pseudo-first-order. Our study shows that the combined process strategy is very promising for the treatment of phenolic pollutants in wastewater.

7.2 TSAMBR – EO Treatment Process and HRT Effect on Sludge Properties and Membrane Fouling of the TSAMBR

In order to produce a high-quality effluent for water re-use, a single treatment process may not be sufficient. In Chapter 5, we studied the use of TSAMBR followed by electrochemical oxidation (TSAMBR – EO) for the treatment of high-temperature and high-strength thermomechanical pulping pressate. The results demonstrated that the TSAMBR – EO process achieved a high COD removal efficiency (94% –97%) and complete solid and color removal, which showed great promise for the utilization of energy from thermomechanical pulping pressate and for the reuse of treated effluent to enable a closed-loop system. In addition, the HRT effect on sludge properties and membrane fouling of the TSAMBR was investigated. A two-stage TMP evolution was observed for the shorter HRTs of 1.1 ± 0.1 and 0.9 ± 0.1d. The low HRT resulted in high EPS concentration, high MLSS and small particles in the bulk sludge. HRT had a significant influence on the cake sludge properties. At an HRT of 1.1 ± 0.1 and 0.9 ± 0.1d, the mean particle size of the cake sludge was larger than that of the bulk sludge, whereas, at the longest HRT, cake sludge flocs tended to be smaller than the bulk sludge flocs. There was no

cake layer formed at HRT=1.7 $\pm$ 0.2d during the entire period of our experiment. The cake layer formed at HRT of 1.1 $\pm$ 0.1d exhibited a homogeneous and compact structure with similar porosity at every level of depth. Dissimilarly, the cake layer developed at an HRT of 0.9 $\pm$ 0.1d showed a two-layer heterogeneous architecture, which led to a considerable contrast in the porosity between the surface layer and base layer. It was also found that the thickness of the cake layer alone did not always coincide with the development of membrane fouling. The cake layer structure evolved over the operating timeline and the alteration of the inner structure of the cake layer was more responsible for the TMP jump. As a result, the cake layer structure was considered as a critical factor for membrane fouling in TSAMBR.

7.3 Photoelectrochemical Determination of COD

Electroanalytical techniques for the monitoring and assessment of water quality are required for process automation. In Chapter 6, a novel bi-functional electrode (TiO_2/Ti/TiO_2-Pt) that featured the combination of an electrocatalyst (TiO_2NTs-Pt) and a photocatalyst (TiO_2NTs) was fabricated for the rapid determination of COD. The TiO_2/Ti/TiO_2-Pt electrode demonstrated enhanced catalytic activity due to the photoelectro-synergistic effect. For the determination of COD, the bi-functional electrode exhibited a working range of 25.0 – 380 mg/L, a low detection limit of 9.5 mg/L, a high sensitivity of 3.55×10^{-3} mA/(mg/L COD) and a high Cl^- tolerance of 1400 mg/L. When the electrode was used for the COD test in real wastewater samples, the results were in excellent agreement with those determined by the standard $K_2Cr_2O_7$ method.

7.4 Concluding Remarks and Future Work

The electrochemical oxidation process has been proven to be an efficient, versatile and environmentally friendly technology that is capable of handling a wide variety of wastewaters.

However, previous studies have typically tested this technology using synthetic wastewater that contained target compounds, which diminished its industrial significance. To expedite the establishment of validation and real-world utility, it is suggested that future studies might direct more attention to the use of electrochemical oxidation for the treatment of actual wastewaters. In addition, high energy consumption is the bottleneck/limiting factor that impedes the full-scale commercial application of electrochemical oxidation. Further investigation is required to improve the electrocatalytic activity and electrochemical stability of electrode materials for the development of enhanced and more cost-effective electrodes, which will translate to lower operational and capital costs.

Electrochemical and photoelectrochemical techniques have been successfully utilized for the rapid determination of COD. However, the working range and stability of these electrodes require further improvement. It is recommended that further work be initiated toward the development of more portable and inexpensive electrochemical devices for the accurate and rapid determination of COD.

Aerobic membrane bioreactors (AMBRs) operated at thermophilic temperatures (> 45 °C) have great potential for incorporation into industrial processes for the direct treatment of high temperature and/or high strength wastewaters. Currently, however, investigation into thermophilic AMBRs (TAMBRs) is very limited. We propose that the effects of operating conditions (e.g., SRT, HRT, and aeration, etc.) on the performance of the TAMBRs should be systematically studied to arrive at the establishment of optimal operating conditions. Moreover, membrane fouling in the TAMBRs is another major area that warrants a more intense focus for future research.

The combination of TSAMBR and electrochemical oxidation has been introduced in this study toward the potential achievement of closed-loop waste stream handling systems within the pulp and paper industry. The results indicate a high possibility of success. However, the operating conditions (e.g., applied current/potentials and reaction time) in the electrochemical oxidation step should be optimized to achieve virtually complete COD removal in the overall process.